Modélisation et analyse de processus pour l'écriture directe à l'encre basée sur des simulations numériques

Yongqiang Tu

HESAM UNIVERSITÉ

Arts et Métiers Sciences et Technologies

ÉCOLE DOCTORALE SCIENCES DES MÉTIERS DE L'INGÉNIEUR
[Laboratoire de Conception, Fabrication, Commande – Campus de Metz]

THÈSE

présentée par: **Yongqiang TU**

soutenue le : **20 avril 2023**

pour obtenir le grade de: **Docteur d'HESAM Université**

préparée à **École Nationale Supérieure d'Arts et Métiers**

Spécialité: **Génie industriel**

Process modeling and analysis for direct ink writing based on numerical simulations

THÈSE dirigée par :
M. SIADAT Ali
M. HASSAN Alaa
M. YANG Gongliu

Jury

Mme. Cécile NOUVEL, Professeur, Université de Lorraine	Présidente
M. Nabil ANWER, Professeur, Université de Paris Saclay	Rapporteur
M. Julien GARDAN, Maitre de Conférences HDR, EPF École d'Ingénieurs	Rapporteur
M. Uzair Khaleeq Uz ZAMAN, Assistant Professor, National University of Sciences and Technology - Pakistan	Examinateur
M. Gianluca PERCOCO, Professor, Polytechnic University of Bari - Italy	Examinateur
M. Ali SIADAT, Professeur, Arts et Métiers ParisTach	Directeur de Thèse
M. Alaa HASSAN, Maître de Conférences, Université de Lorraine	Co- Directeur de Thèse
M. Gongliu YANG, Professor, Beihang University - PR China	Co- Directeur de Thèse

THÈSE

Acknowledgement

The thesis was conducted in Laboratory LCFC (Laboratoire de Conception Fabrication Commande) in Metz Campus of ENSAM (École Nationale Supérieure des Arts et Métiers), ERPI (Équipe de Recherche sur les Processus Innovatifs) in Université de Lorraine and Lorraine Fab Living Lab® (LF2L®) in ERPI. In addition, the thesis was financially supported by CSC (China Scholarship Council) under grant 201906020135.

I feel grateful and fortunate having the opportunity to study in France for three years on the subject related to direct ink writing (DIW). Joining the research team of Prof. Ali Siadat and Dr. Alaa Hassan and doing research work on DIW was a life-changing scientific research experience for me, where I found my career direction, gained comprehensive research training, shaped my research attitude and build up my confidence to face difficulties. I would not have been able to complete the journey without the help I received from different individuals, and I feel truly beholden to them.

Firstly, I would like to express my sincere gratitude to my respectable supervisors, Prof. Ali Siadat and Dr. Alaa Hassan, who gave me the opportunity to pursue a PhD degree in France. Prof. Ali Siadat always emphasized the need to distil scientific questions from the applications and challenges, giving me a deeper understanding of scientific research. Dr. Alaa Hassan helped me to understand the whole research work by giving me patient guidance and constructive advice. And Dr. Alaa Hassan always supported my ideas and gave me enough freedom to carry out research work. At the same time, both Prof. Ali Siadat and Dr. Alaa Hassan cared about my work progress and life, and helped me as much as possible. I am grateful for their continuous support, kind patience and scientific advice.

Secondly, I would like to express my deep gratitude to Prof. Gongliu Yang and Prof. Lihong Qiao in Beihang University. They encouraged me to study aboard and gave me a lot of advices on thesis writing. With their encouragement and insightful comments, I was able to consist on my doctoral studies. Also, I deeply appreciated Dr. Julien Gardan and Dr. Uzair Khaleeq Uz Zaman, for being my referees and giving me valuable advice for thesis every year. Specially, Dr. Uzair Khaleeq Uz Zaman gave me a lot of advice on process parameters optimization using Taguchi method and helped me revise my draft for journal article submission.

Thirdly, I would like to thank all the members of my jury. It is an honour for me to invite such famous and knowledgeable scholars as my jury. Their insightful and valuable suggestions are sincerely appreciated. I would like to thank Prof. Cécile NOUVEL, Prof. Nabil ANWER

and Prof. Gianluca PERCOCO for accepting my invitation and taking the precise time to participate in my PhD defence.

Moreover, I would like to thank my colleagues in LCFC, ERPI and LF2L®: Javier Arrieta-Escobar, Fangkai Xue, Benjamin Ennesser-Serville, Neal Widmer, Catalina Suescun, Halima Ramdami, Guillaume Prosnot, Maksym Proskurin, Ferney Osorio, Mariela Martinez, Jose Luis Rivera Gil, Benjamin Dethine, Diana Cardenas, Marie Gribouval, Anaëlle Hily. Specially, Javier Arrieta-Escobar helped me to prepare the ink used in DIW and gave me numerous advices on ink material properties characterization. Fangkai Xue gave me a lot of suggestions on numerical simulations and encouraged me to do work on numerical simulation, so I could consist on the numerical simulations and realize numerical simulations of the DIW process. Benjamin Ennesser-Serville taught me how to use the 3D printers and helped whenever I had problem using 3D printer, so I could conduct printing experiments successfully.

Finally, I would like to give thanks to my family for their endless love and unfailing support during all these years of study. Thank them for believing in me. And I would like to express my gratitude to the CSC for providing the scholarship to support my study and life in France.

Yongqiang Tu

Beijing

April 2023

Contents

List of Figures

List of Tables

Nomenclature

AM	Additive manufacturing
ANOVA	Analysis of variance
BJ	Binder jetting
BJ3DP	Binder jet 3D printing
CAD	Computer-aided design
CFD	Computational fluid dynamics
DED	Directed energy deposition
DF	Deposited filament
DIW	Direct ink writing
DLP	Digital light processing
DMD	Digital micro-mirror device
DMLS	Direct metal laser sintering
DOE	Design of experiments
DOF	Design of freedom
EBM	Electron beam melting
FDM	Fused deposition modeling
FEA	Finite element analysis
FEF	Freeform extruded filament
HBM	Hershel-Bulkley model
IJP	Inkjet printing
LOM	Laminated object manufacturing
MDDSEO	Maximum distance deviation between simulated and experimental outlines
ME	Material extrusion
MEAM	Material extrusion AM
MJ	Material jetting
ML	Machine learning

OA	Orthogonal array
PBDED	Powder based directed energy deposition
PBF	Powder bed fusion
PLA	Poly-lactic acid
RSM	Response surface methodology
SHL	Sheet lamination
SHS	Selective heat sintering
SL	Stereolithography
SLM	Selective laser melting
SLS	Selective laser sintering
SNR	Signal-to-noise ratio
TPP	Two-photon polymerization
UV	Ultraviolet
VOF	Volume of fluid
VPP	Vat photo polymerization
WBDED	Wire based directed energy deposition
2D	Two-dimensional
3D	Three-dimensional
G'	Storage modulus
G''	Loss modulus
τ	Shear stress
$\dot{\gamma}$	Shear rate
μ	Viscosity of the ink
μ_0	Limiting dynamic viscosity
τ_0	Yield stress
K	Consistency index
n	Flow index
θ_C	Static contact angle

R^2	Coefficient of determination
ρ	Density of the ink
σ	Surface tension coefficient
D_p	Piston diameter
d_n	Inner diameter of nozzle
D_n	Outer diameter of nozzle
L_n	Nozzle length
L_0	Initial filled length of ink
h	Distance between nozzle bottom and substrate
v_e	Average velocity of ink in nozzle
v_p	Piston velocity
v_n	Nozzle velocity
V^*	Dimensionless nozzle velocity, $= v_n / v_e$
H^*	Dimensionless height, $= h / d_n$
$\bar{w}_O$	Average width of the optimal printed line
d_l	Distance between lines
R_W	Ratio of d_l to $\bar{w}_O$
W	Weight of the printed layer
N_1	Number of measuring points set along the line length
$w_i (i = 1, 2, ..., N_1)$	Widths of line on each measuring point
$\bar{w}$	Average width of printed line
$el_i (i = 1, 2, ..., N_1)$	Dimensional errors on each measuring point along length
N_2	Number of measuring points set along x direction in printed rectangular object
N_3	Number of measuring points set along y direction in printed rectangular object

$lx_i (i = 1, 2, ..., N_2)$	Lengths on each measuring point along x direction of printed rectangular object
$ly_i (i = 1, 2, ..., N_3)$	Lengths on each measuring point along y direction of printed rectangular object
$\overline{lx}$	Average length in x direction of printed rectangular object
$\overline{ly}$	Average length in y direction of printed rectangular object
Lx	Designed dimension for rectangular object in x direction
Ly	Designed dimension for rectangular object in y direction
$erx_i (i = 1, 2, ..., N_2)$	Dimensional error for the printed rectangular object in x directions
$ery_i (i = 1, 2, ..., N_3)$	Dimensional error for the printed rectangular object in y directions
S	DOF of a factor
T	Number of experiments
DOF_{total}	Total DOF of factors and their interaction effects
L_T	OA with T experiments
η	Average SNR
α	Phase fraction for a mesh
V_i	Volume of the ink in a mesh
V_m	Total volume of a mesh
ρ_s	Density of the single continuum
μ_s	Viscosity of the single continuum
ρ_a	Density of the air
μ_a	Viscosity of the air
$\mathbf{U}$	Velocity field
p	Pressure
$\mathbf{g}$	Gravitational acceleration vector
$\mathbf{F}_\sigma$	Surface tension

κ	Surface curvature
$\mathbf{n}$	Normal vector to the ink surface
$\hat{\mathbf{n}}$	Unit vector normal to the ink surface
$\hat{\mathbf{n}}_w$	Unit vector normal to the substrate
$\hat{\mathbf{t}}_w$	Unit vector tangent to the substrate
t	Time
$\mathbf{U_r}$	Velocity vector compressing two-phase free surface
c	Controllable compression factor
E_f	Diameter prediction accuracy of numerical simulation of FEF
N_f	Number of measurement points in FEF
e_{fi}	Diameter difference between experimental and simulation results
d_{fi}	Diameter of FEF
β	Ratio of D_n to d_n, $= D_n / d_n$
γ	$=\left(\theta_C - \frac{\sin 2\theta_C}{2}\right)\left(\frac{1}{1-\cos\theta_C}\right)^2$
h_d	Height of DF
w_d	Width of DF
θ	Angle of deposited corners
$\mathbf{v_{n1}}$	Nozzle velocity on substrate 1
$\mathbf{v_{n2}}$	Nozzle velocity on substrate 2
v_{nx}	Velocity on substrate along x axis
v_{ny}	Velocity on substrate along y axis

Résumé Étendu En Français

1 Introduction générale

1.1 Contexte et objectif de la thèse

La fabrication additive (FA) est une technologie de fabrication avancée qui imprime directement des pièces tridimensionnelles (3D) en empilant des matériaux couche par couche sur la base d'un modèle numérique 3D de conception assistée par ordinateur (CAO) [1-5]. Par rapport aux techniques de fabrication traditionnelles telles que le forgeage, le moulage, le soudage et l'usinage (tournage, fraisage, rabotage, meulage, etc.), la FA présente les avantages de la numérisation, de l'économie de matière, de la diversification des matériaux et de la possibilité de fabriquer facilement des pièces complexes, qui répondent les exigences de haute précision, de liberté structurelle et de personnalisation pour le développement de nouveaux matériaux et de nouvelles structures dans l'ingénierie tissulaire, la médecine, l'ingénierie du caoutchouc, l'ingénierie céramique, les capteurs, l'aviation, l'aérospatiale, l'électronique, l'alimentation et d'autres applications industrielles [6-10]. Selon ISO/ASTM 52900 (2015), la fabrication additive est divisée en sept catégories basées sur le principe de fonctionnement : jet de liant (BJ), dépôt d'énergie dirigée (DED), extrusion de matériau (ME), jet de matériau (MJ), fusion sur lit de poudre (PBF), laminage de feuilles (SHL) et photopolymérisation en cuve (VPP).

L'écriture directe à l'encre (DIW) appartient à l'extrusion de matériau (MEAM) selon le principe de fonctionnement. Le principe de fonctionnement de DIW est le suivant : premièrement, le matériau est préparé sous forme de pâte ou de suspension avec une bonne imprimabilité appelée encre ; puis l'encre est extrudée à partir d'une buse en filaments continus à l'aide d'une force mécanique (piston ou entraînement par vis) ou d'une force pneumatique ; et enfin les filaments sont déposés en parties 3D par couches [11]. Par rapport à d'autres techniques de la FA, DIW présente les avantages exceptionnels de la diversité des matériaux et de la flexibilité des équipements [12-14]. En raison de ses avantages, DIW est devenu l'une des techniques FA les plus populaires ces dernières années.

Cependant, la compréhension et l'analyse du processus de DIW n'ont pas été entièrement étudiées, ce qui limite la précision de fabrication et la promotion de l'application de cette technique. Dans des études récentes, en raison du manque de compréhension et d'analyse des processus de DIW, les chercheurs doivent passer par de nombreux essais pour trouver une fenêtre imprimable des propriétés de l'encre et des paramètres de processus adaptés au DIW pour obtenir la qualité d'impression qui répond aux exigences d'utilisation [15-17], ce qui augmente considérablement les coûts et réduit l'attractivité des applications de DIW. Pour

résoudre ce problème, il est essentiel de faire des recherches sur l'analyse des processus pour DIW afin de bien comprendre ce processus et d'améliorer la convivialité de DIW. La simulation numérique est l'un des outils les plus puissants d'analyse de processus en AM. L'analyse de processus basée sur des simulations numériques présente des avantages en termes d'économie de temps de matériau/d'essai et de capture facile de la valeur des paramètres de processus critiques qui sont difficiles à obtenir par des mesures expérimentales. La recherche sur la modélisation des processus et l'analyse de DIW basée sur des simulations numériques fournira un soutien important pour le développement et l'orientation de DIW. Cependant, il existe actuellement peu de travaux systématiques sur la modélisation et l'analyse des processus basés sur des simulations numériques pour DIW. Pour combler cette lacune, l'objectif de cette thèse est de contribuer à la modélisation et à l'analyse des processus DIW basées sur des simulations numériques.

1.2 Contenu de la recherche

Le processus DIW est influencé à la fois par les propriétés du matériau de l'encre et les paramètres du processus. Les propriétés des matériaux d'encre et les paramètres de processus sont des conditions d'entrée dans les simulations numériques. Ainsi, une fois la caractérisation des propriétés des matériaux d'encre et la sélection des paramètres de processus sont étudiées,les résultats de la recherche sont utilisés comme conditions d'entrée pour les simulations numériques. Ensuite, des simulations numériques pour DIW sont réalisées. En tant que l'une des technologies FA, comme le montre la figure 1.1, l'ensemble des étapes du processus de DIW comprend :

- Étape 1 : Modélisation géométrique 3D à l'aide d'une conception descendante dans un logiciel de modélisation 3D comme Solidworks, ProE, UG, CATIA, 3DMAx, etc. ou en utilisant une conception d'inversion basée sur les données du modèle 3D de la technologie de réalité virtuelle ou du scanner 3D ;
- Étape 2 : Génération de G-code en important le format STL du modèle géométrique 3D et en définissant les paramètres de processus dans le logiciel Slicer ;
- Étape 3 : Impression dans une imprimante 3D DIW à l'aide du G-code généré via le processus de fabrication par couches.

En particulier, DIW peut imprimer des pièces 3D arbitrairement complexes par extrusion d'encre, points à ligne, lignes à couche et couches à pièces 3D, comme illustré dans le tableau de l'étape 3 de la figure 1.1. Parmi ce processus, le filament extrudé de forme libre (FEF), le filament déposé (DF) et le coin déposé sont les éléments les plus fondamentaux et les plus

critiques. Ainsi, la thèse porte sur les simulations numériques et les analyses de processus de ces éléments fondamentaux et critiques : FEF, DF et coin déposé.

En conclusion, pour atteindre l'objectif de la thèse, le contenu de la recherche comprend :

- Recherche sur la caractérisation des propriétés des matériaux d'encre et la sélection des paramètres de processus ;
- Recherche sur la simulation numérique des éléments de base et critiques dans DIW, y compris FEF, DF et coin déposé ;
- Vérifications expérimentales des simulations numériques proposées ;
- Analyse de processus basée sur les simulations numériques proposées.

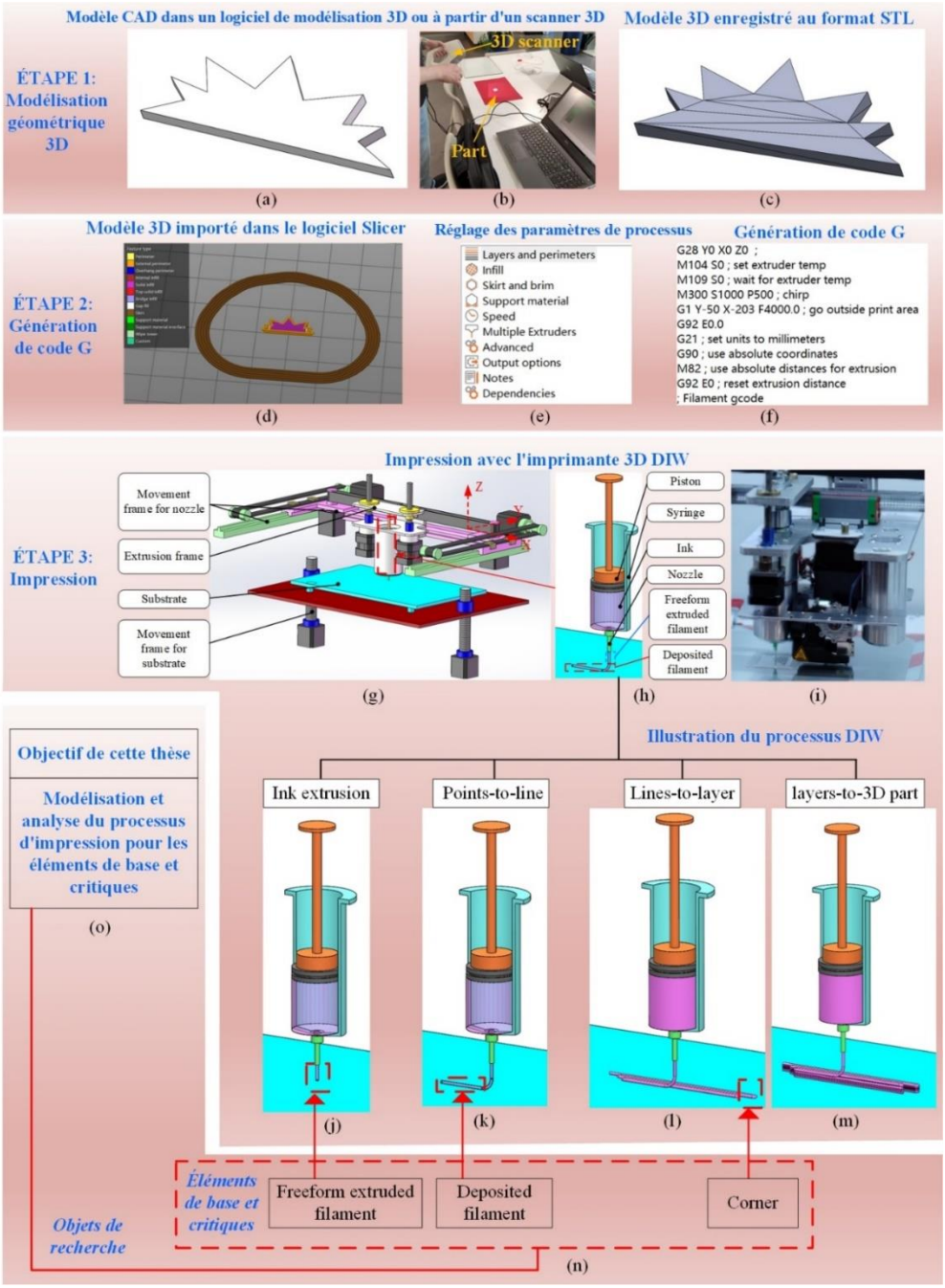

Figure 1.1 Illustration du processus de DIW et l'objetif de recherche résumé dans cette thèse : (a) modèle CAO construit dans un logiciel de modélisation 3D ; (b) Modèle CAO à partir d'un scanner 3D ; (c) Modèle CAO enregistré au format STL ; (d) Modèle 3D importé dans le logiciel Slicer ; (e) réglage des paramètres de processus dans le logiciel Slicer ; (f) G-code généré à l'aide du logiciel Slicer ; (g) composition mécanique de l'imprimante 3D DIW ; (h) encre dans la seringue ; (i) photo réelle de l'imprimante 3D DIW ; (j) processus d'extrusion d'encre; (k) processus point à ligne ; (l) processus lignes-couches ; (m) processus de pièces en couches en 3D ; (n) éléments de base et critiques du processus DIW ; (o) objetif de recherche résumé

1.3 Structure de la thèse

Cette thèse est structurée en cinq chapitres et le contenu de chaque chapitre est brièvement introduit comme suit :

Le chapitre 1 donne un aperçu du contexte et de l'objectif de la recherche. Enfin, la structure de la thèse est esquissée.

Le chapitre 2 présente l'état de l'art, une revue systématique de la littérature de DIW est menée d'abord pour résumer les caractéristiques, le développement, les défis et les solutions aux défis de DIW et un problème insuffisamment résolu est déterminé comme la question de recherche de cette thèse. Pour répondre à la question de recherche, la modélisation et l'analyse des processus pour DIW sont sélectionnées afin d'apporter une réponse. Ensuite, une littérature sur la modélisation et l'analyse des processus pour DIW est réalisée. Les entrées et les sorties de la modélisation de processus de DIW sont résumées et les méthodes de modélisation de processus numériques sont sélectionnées comme la méthode la plus appropriée pour la modélisation de processus et l'analyse de DIW. Enfin, l'objectif de cette thèse est repositionné par rapport à la revue de la littérature.

Le chapitre 3 présente les travaux sur la caractérisation des propriétés des matériaux d'encre et la sélection des paramètres de processus pour fournir les entrées de la modélisation. Pour la caractérisation des propriétés du matériau de l'encre, la densité, la tension superficielle, l'angle de contact statique et les propriétés rhéologiques sont obtenues pour l'encre utilisée. Pour la sélection des paramètres de processus, les paramètres de processus DIW sont identifiés par des analyses d'impression via un plan d'expérience. Ainsi, une méthode d'optimisation en deux étapes est proposée pour optimiser les paramètres de processus DIW pour la précision dimensionnelle des couches imprimées et l'analyse de l'importance de chaque paramètre de processus.

Le chapitre 4 présente les simulations numériques de FEF, DF et des coins déposés dans DIW. Dans un premier temps, la méthode de simulation numérique, volume de fluide (VOF), est introduite. Ensuite, des simulations numériques de FEF, DF et des coins déposés sont présentées à travers la modélisation géométrique, la génération de maillages, la détermination des conditions aux limites. Ensuite, des vérifications expérimentales sont menées pour vérifier les simulations numériques proposées. Enfin, l'analyse du processus est effectuée sur la base du modèle de simulation numérique proposé.

Le chapitre 5 présente la conclusion et les perspectives de la thèse.

2 État de l'art

2.1 Introduction

Ces dernières années, DIW a attiré une grande attention à la fois du milieu universitaire et de l'industrie, et DIW est devenu l'une des techniques FA les plus populaires. Cependant, en tant que technique qui s'est développée rapidement ces dernières années, il reste encore de nombreux problèmes à résoudre dans l'utilisation pratique de DIW et un état de l'art complet de DIW est essentiel pour comprendre son statut de développement et ses problèmes. Un état de l'art de la technique DIW a été d'abord mené et les problèmes potentiels liés à celle-ci ont été identifiés. Les résultats de l'état de l'art ont conclu à la modélisation et l'analyse des processus DIW à l'aide de simulations numériques sont comme un moyen efficace de résoudre les problèmes non résolus. Ainsi, une revue de la littérature sur la modélisation et l'analyse des processus à l'aide de simulations numériques pour DIW est en outre effectuée et les lacunes de la recherche sont résumées.

Le reste de ce chapitre est organisé comme suit. La section 2.2 présente la revue systématique de la littérature sur DIW. Elle présente d'abord la criticité de la technologie FA dans la section 2.2.1. Ensuite, les techniques FA les plus couramment utilisées sont présentées et les caractéristiques de chaque technique FA sont résumées pour analyser les avantages et les applications appropriées de DIW dans la section 2.2.2. Ensuite, le développement, les défis et les solutions existantes de DIW sont examinés et la question de recherche de cette thèse dans la section 2.2.3 a été formulée. Pour résoudre la question de recherche, la modélisation et l'analyse des processus pour DIW sont sélectionnées comme base de solution. Ainsi, la modélisation et l'analyse des processus pour DIW sont examinées dans la section 2.3. Les entrées et les sorties de la modélisation des processus sont résumées dans la section 2.3.1 et les méthodes de modélisation des processus sont examinées dans la section 2.3.2. Sur la base des

lacunes de la recherche résumées dans la revue de la littérature, la section 2.3.3 identifie l'objectif de cette thèse.

2.2 Une revue de la littérature sur DIW

Au cours des cinq dernières années, la technologie FA a suscité une grande attention et a été utilisée avec succès dans diverses applications présentant un grand potentiel commercial (Figure 2.1). Et comme le montre la Figure 2.2, les techniques de fabrication additive couramment utilisées comprennent : l'impression 3D par jet de liant (BJ3DP), la fabrication d'objets laminés (LOM), la modélisation par dépôt de fil fondu (FDM), l'écriture directe à l'encre (DIW), l'impression à jet d'encre (IJP), l'impression sélective frittage laser (SLS), fusion laser sélective (SLM), dépôt d'énergie dirigée à base de poudre (PBDED), dépôt d'énergie dirigée à base de fil (WBDED), stéréolithographie (SL), traitement numérique de la lumière (DLP) et polymérisation à deux photons (TPP).

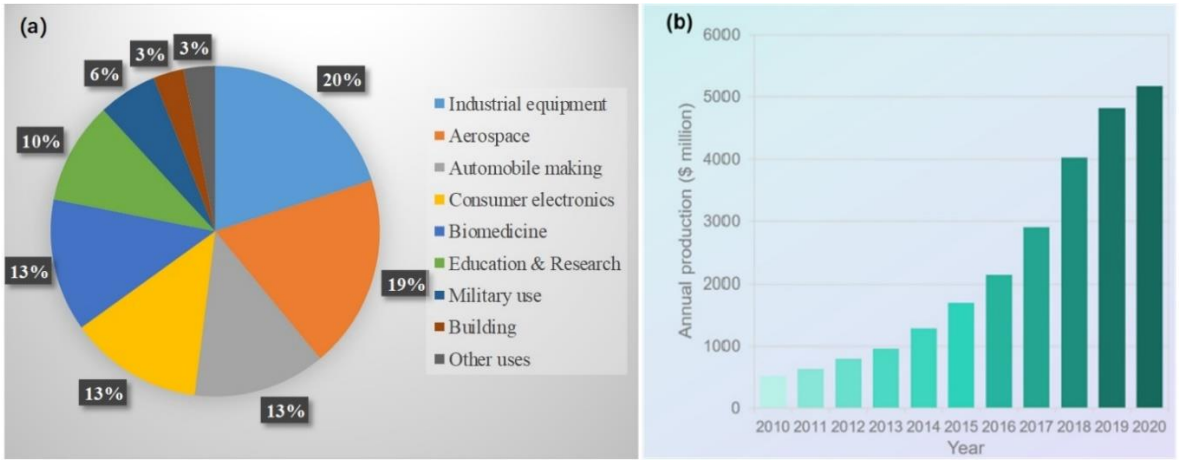

Figure 2.1 (a) Applications de la FA et part de production dans divers secteurs et (b) Production annuelle de pièces FA par des fournisseurs de services indépendants dans le monde entier (en millions de dollars américains) [24]

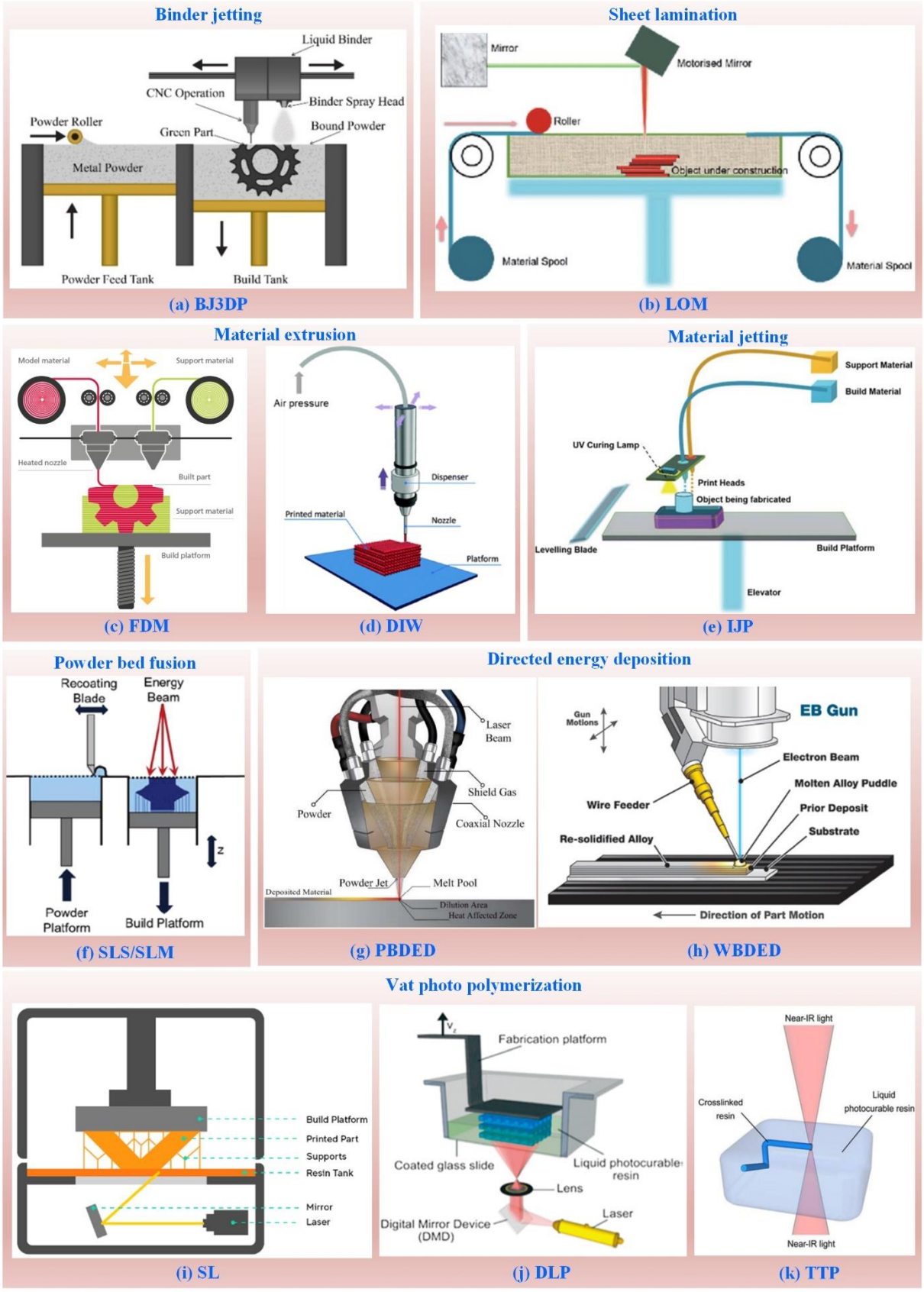

Figure 2.2 Classification et illustrations de différentes techniques FA couramment utilisées : (a) BJ3DP, (b) LOM, (c) FDM, (d) DIW, (e) IJP, (f) SLS/SLM, (g) PBDED, (h) WBDED, (i) SL, (j) DLP, (k) TTP

Les caractéristiques de chaque technique FA sont résumées dans le tableau 2.1 [24] :

Table 2.1 Caractéristiques, matériaux applicables, forme de la matière, méthode de formage, exigence d'impression et résolution de chaque technique FA [24]

Technique FM	Caractéristiques	Matériaux applicables	Forme de la matière	Méthode de formage	Exigence d'impression	Résolution
BJ3DP	Résistance limitée et surfaces rugueuses	Métaux, sable, céramique	Lisier & Poudre	Collage de liant	Besoin d'un liant	µm à mm
LOM	Faible vitesse et grande taille, faible précision, limité par le liant	Papier, plastique, métaux, céramique	Laminage	Empilage et découpe laser	Laminage	mm
FDM	Vitesse élevée et grande taille, faible précision, limitée par la température d'extrusion	Polymères thermoplastiques	Filament	Extrusion	A l'état de filament	mm
DIW	Grande vitesse, faible coût, large choix de matériaux	Polymères, bio-encre, métaux, ciment, céramique	Encrer	Extrusion	Viscosité et propriétés rhéologiques appropriées	Quelques 100 µm à mm
IJP	Moins de quantité de matière, limitée par les encres imprimables, faible vitesse d'impression	Polymères, bio-encre, métaux, céramiques	Encrer	Formation de gouttelettes	Faible viscosité avec collage rapide	Quelques 100 µm à mm
SLS	Vitesse lente, précision dimensionnelle élevée	Nylon, métaux	Poudre	Frittage de poudre	Fusible au laser	µm à mm
SLM	Vitesse lente, précision dimensionnelle élevée	Métaux	Poudre	Fusion de poudre	Fusible au laser	µm à mm
PBDED	Grande vitesse, grande taille	Métaux	Poudre	Fusion de poudre	Fondant par énergie	µm à mm
WBDED	Haute vitesse, grande taille, faible précision	Métaux	Fil	Fusion de fil	Fondant par énergie	mm
SL	Vitesse modérée, rendement élevé, bonne qualité de surface	Résines, céramiques	Bouillie	Polymérisation linéaire	Photodurcissables aux UV	Sous 100 µm
DLP	Haute vitesse, rendement élevé, bonne qualité de surface	Résines, céramiques	Bouillie	Polymérisation linéaire	Photodurcissables aux UV	Sous 100 µm
TPP	Slow speed, high cost, fine surface quality, highest printing precision	Résines, céramiques	Bouillie	Polymérisation non linéaire	Photopolymérisation à deux photons	Sous µm

Selon le tableau 2.1, les comparaisons de la diversité des matériaux, du coût, de la vitesse, de la résolution de chaque technique FA sont répertoriées comme suit:

(1) Diversité des matériaux

DIW> IJP>LOM>BJ3DP>FDM>SL, DLP, TPP>SLS>SLM, PBDED, WBDED

(2) Coût

SLM>SLS>PBDED>WBDED>TPP>SL>DLP>IJP>BJ3DP>LOM>FDM>**DIW**

(3) Vitesse

IJP, BJ3DP > DLP > LOM > **DIW** > FDM > WBDED > PBDED > SLM > SLS > SL > TPP

(4) Résolution

TPP>SL>DLP>SLM>SLS>PBDED>IJP>BJ3DP>**DIW**>FDM>WBDED>LOM

En raison des avantages exceptionnels de la diversité des matériaux et de la flexibilité des équipements, DIW est devenu l'une des techniques AM les plus populaires et les chercheurs ont effectué de nombreux travaux sur DIW pour la promotion de son application. Le DIW a été utilisé avec succès dans l'ingénierie du caoutchouc [62], l'ingénierie tissulaire [63], les batteries [64], les circuits électroniques [65], les bâtiments [66], l'ingénierie céramique [67], les capteurs et l'impression 4D [68] (Figure 2.3). Prévisible que de plus en plus de nouveaux matériaux seront préparés sous forme d'encres adaptées au DIW et appliqués dans un plus grand nombre d'applications nécessitant des matériaux ou des pièces structurels ou fonctionnels.

Figure 2.3 Matériaux appropriés et applications correspondantes au DIW : (a) encre polymère dans l'ingénierie du caoutchouc [62] ; (b) encre biologique dans le génie tissulaire [63];(c) encre métallique dans les batteries [64], circuits électroniques [65]; d) encre de ciment dans les bâtiments [66] ; e) encre céramique dans l'ingénierie céramique [67] ; (f) encre fonctionnelle dans l'impression 4D et les capteurs [68]

En tant que technique qui s'est développée rapidement ces dernières années, bien que de nombreux chercheurs aient effectué de nombreuses recherches sur le développement du DIW, de nombreux défis doivent encore être relevés pour améliorer la finition de surface lisse, la précision dimensionnelle et les propriétés (mécaniques et fonctionnelles) pour la promotion et l'industrialisation du DIW. Les principaux problèmes de DIW sont résumés comme suit [9] :

(1) Difficulté à construire de grands surplombs ou portées avec une précision géométrique parfaite malgré l'utilisation d'encre à rhéologie optimisée ;

(2) Difficulté de préparation de l'encre avec une rhéologie optimisée : l'encre doit s'écouler facilement sous contrainte de cisaillement et récupérer et conserver rapidement sa forme lors du dépôt ;

(3) Difficulté à extruder l'encre à travers des pièces extrêmement petites pour imprimer des pièces à haute résolution en raison du colmatage ;

(4) Difficulté à trouver rapidement des paramètres de processus appropriés pour l'encre préparée.

De nombreux chercheurs ont effectué diverses recherches pour proposer des suggestions et des références pour résoudre les problèmes. Les solutions aux problèmes ci-dessus proposées par les chercheurs sont résumées comme suit :

(1) Pour la question (1), les chercheurs ont utilisé des supports sacrificiels pour élargir la gamme de géométries pouvant être fabriquées par le DIW [90] ;

(2) Pour la question (2), la question de la recherche et de nombreux travaux sur DIW se concentrent principalement sur la préparation de l'encre, puis ils sélectionnent la meilleure encre en utilisant la caractérisation rhéologique à l'aide de tests de rhéologie, y compris le test de rampe de contrainte de cisaillement, le test de balayage du taux de cisaillement, le balayage de fréquence test et test de récupération [67] ;

(3) La question (3) peut être évitée en utilisant un lubrifiant de surface approprié tel que l'acide oléique pour réduire le frottement entre les particules et la formation d'agglomération [91] et en améliorant la conception des buses [92] ;

(4) Les chercheurs doivent passer par de nombreux essais pour trouver une fenêtre imprimable de propriétés d'encre et de paramètres de processus adaptés au DIW pour obtenir la qualité d'impression qui répond aux exigences d'utilisation [15-17].

La raison principale de la question (4) est que la recherche sur l'analyse du procédé DIW fait très défaut car la modélisation et l'analyse du procédé DIW n'ont pas été entièrement étudiées, ce qui limite la précision de fabrication et la promotion de l'application de cette technique. Cette question augmente considérablement les coûts et réduit l'attractivité des applications de DIW. Pour résoudre ce problème, il est essentiel de proposer des méthodes et des outils afin de réduire le nombre d'essais sur les encres. La modélisation et l'analyse numériques des processus DIW peuvent apporter une réponse à cette question.

2.3 Une revue de la littérature sur la modélisation et l'analyse des processus DIW

Le but de la modélisation de processus DIW est de construire la relation entre l'entrée et la sortie dans le processus d'impression 3D, qui est utilisée pour prédire la sortie en fonction de l'entrée avant l'impression. La revue de la littérature résume les entrées et les sorties de la modélisation pour DIW comme le montre la Figure 2.8. Les entrées sont les propriétés matérielles de l'encre et le réglage des paramètres du processus d'impression. Les sorties incluent le FEF, le DF, le coin déposé, la couche imprimée et la pièce 3D (Figure 2.9).

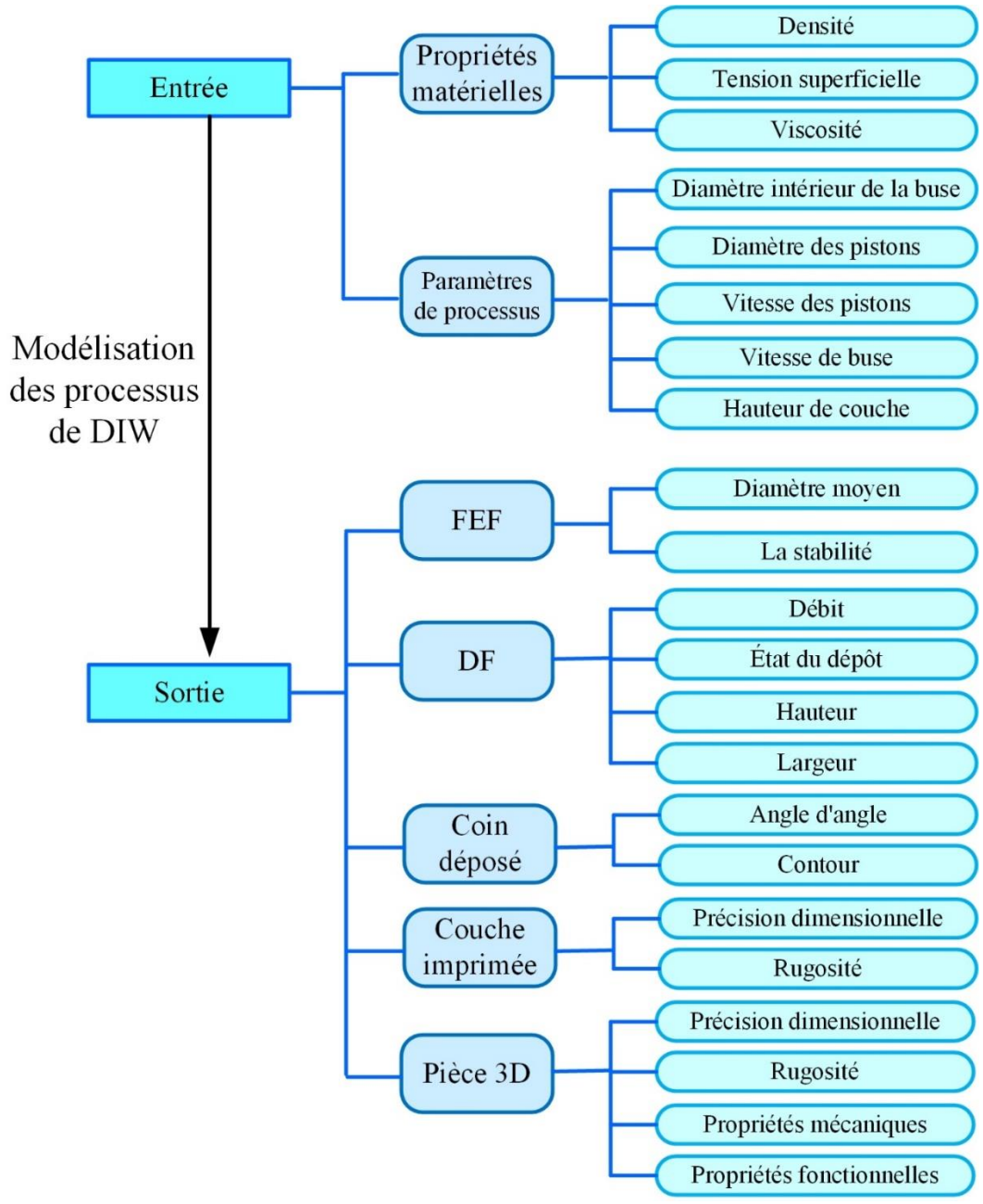

Figure 2.8 Entrées et sorties de la modélisation de processus DIW

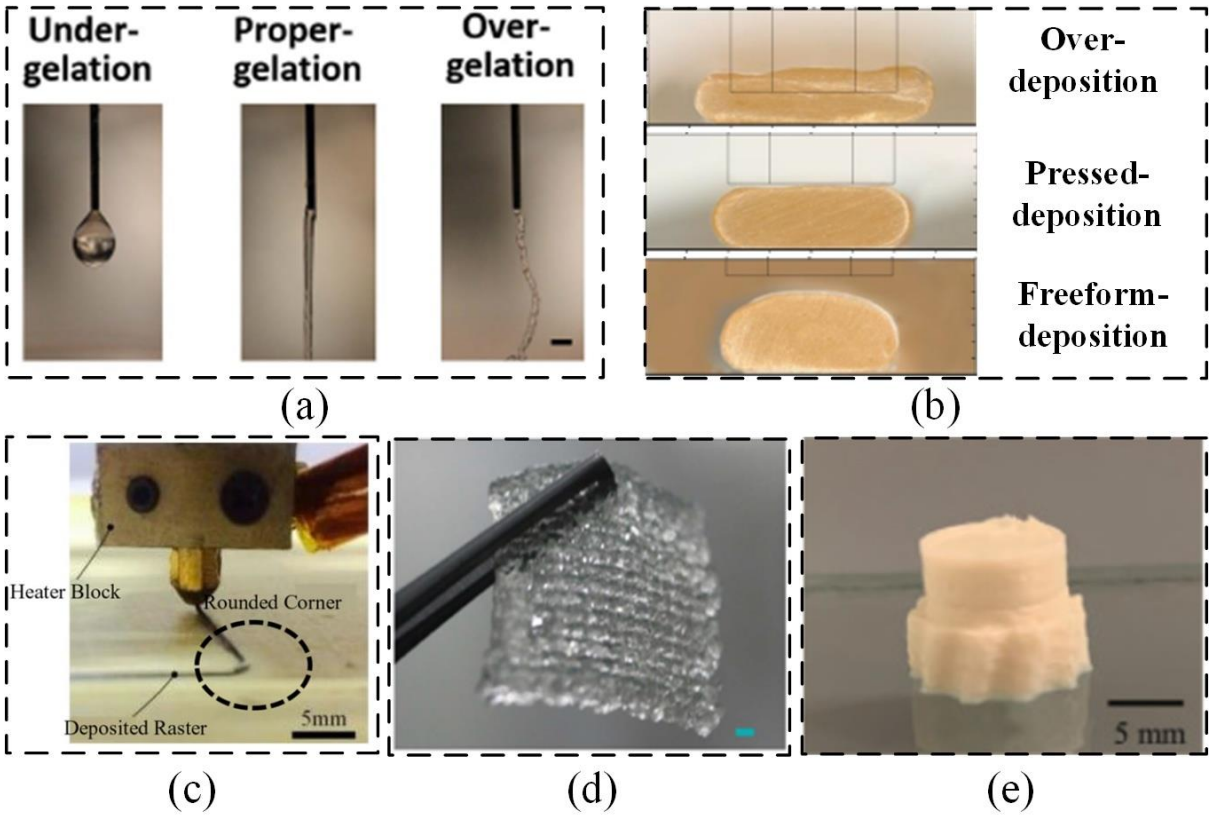

Figure 2.9 Photos physiques des sorties de la modélisation de processus pour DIW : (a) FEF, (b) DF, (c) coin déposé, (d) couche imprimée, (e) pièce 3D

La simulation numérique est l'un des outils les plus puissants d'analyse de processus en FA. L'analyse de processus basée sur des simulations numériques présente des avantages en termes d'économie de temps de matériau/d'essai et de capture facile de la valeur des paramètres de processus critiques qui sont difficiles à obtenir par des mesures expérimentales. La recherche sur la modélisation des processus et l'analyse de DIW basée sur des simulations numériques fournira un soutien important pour le développement et l'orientation de DIW. Cependant, il existe actuellement peu de travaux systématiques sur la modélisation et l'analyse des processus basés sur des simulations numériques pour DIW. Pour combler cette lacune, l'objectif de cette thèse est de contribuer à la modélisation et l'analyse des processus DIW basées sur des simulations numériques.

3 Caractérisation des propriétés des matériaux d'encre et sélection des paramètres de traitement

La qualité d'impression du processus DIW dépend des propriétés du matériau de l'encre et du réglage des paramètres du processus. Des études récentes [93-95] se sont concentrées sur la préparation des encres et la caractérisation des propriétés des matériaux d'encre, car les

propriétés des matériaux d'encre jouent le rôle le plus critique dans le processus d'extrusion, le retrait, la fidélité de forme et la stabilité structurelle. Les paramètres du procédé DIW concernés par l'équipement affectent considérablement la précision dimensionnelle des pièces [96]. Pendant ce temps, les propriétés des matériaux d'encre et les paramètres de processus sont des entrées de la modélisation de processus DIW. Ainsi, ce chapitre présente les recherches sur la caractérisation des propriétés des matériaux d'encre et la sélection des paramètres de processus pour fournir la base des entrées de modélisation.

Pour la caractérisation des propriétés du matériau de l'encre, la densité, la tension superficielle, l'angle de contact statique et les propriétés rhéologiques sont obtenues pour l'encre utilisée.

Pour la sélection des paramètres de processus. Récemment, la sélection des paramètres de processus DIW a été menée par de nombreux chercheurs [98, 158, 159]. Cependant, toutes ces études ont simplement déterminé une fenêtre d'imprimabilité au lieu d'une valeur optimale et peu d'études sont disponibles pour l'analyse de l'importance des paramètres de processus et l'optimisation pour DIW. Par conséquent, il est important d'étudier l'impact de chaque paramètre de processus et de trouver le réglage optimal des paramètres de processus pour améliorer la précision dimensionnelle des pièces fabriquée en DIW.

La méthode Taguchi [123] et les méthodes d'apprentissage automatique (ML) [108, 160] ont été largement utilisées pour contrôler les paramètres de processus de l'impression 3D basée sur l'extrusion de matériaux. Les méthodes ML permettent la sélection appropriée des paramètres avec peu d'analyses de processus, mais nécessitent un grand ensemble de données, du temps et des ressources informatiques supplémentaires [133]. La technique de Taguchi est plus efficace [161] avec une réduction significative du temps et du coût expérimentaux [126] et elle peut déterminer la signification de chaque paramètre par analyse de variance (ANOVA) [162]. Pour effectuer l'optimisation des paramètres du processus DIW avec un minimum de matériel et de temps, la méthode Taguchi est adoptée dans cette thèse.

Les propriétés des matériaux d'encre sont caractérisées pour l'encre utilisée dans cette thèse. Ensuite, les paramètres de processus sont sélectionnés pour l'encre utilisée dans l'imprimante 3D DIW. En particulier, dans la sélection des paramètres de processus, nous identifions les paramètres de processus DIW par des analyses d'impression et proposons une méthode d'optimisation en deux étapes pour optimiser les paramètres de processus DIW pour la précision dimensionnelle des couches imprimées et analyser l'importance de chaque paramètre de processus (Figure 3.5). Pour vérifier la méthode, des tests de confirmation sont effectués en

tenant compte de la comparaison des conditions et de la robustesse de la méthode sur d'autres formes. Ainsi,ces tests comparent l'adaptabilité des paramètres dans l'impression de pièces 3D à partir des analyses des couches imprimées pour la méthode proposée et de l'adaptabilité des paramètres dans les constructions 3D fabriquées à 100 % de remplissage ou avec porosités.

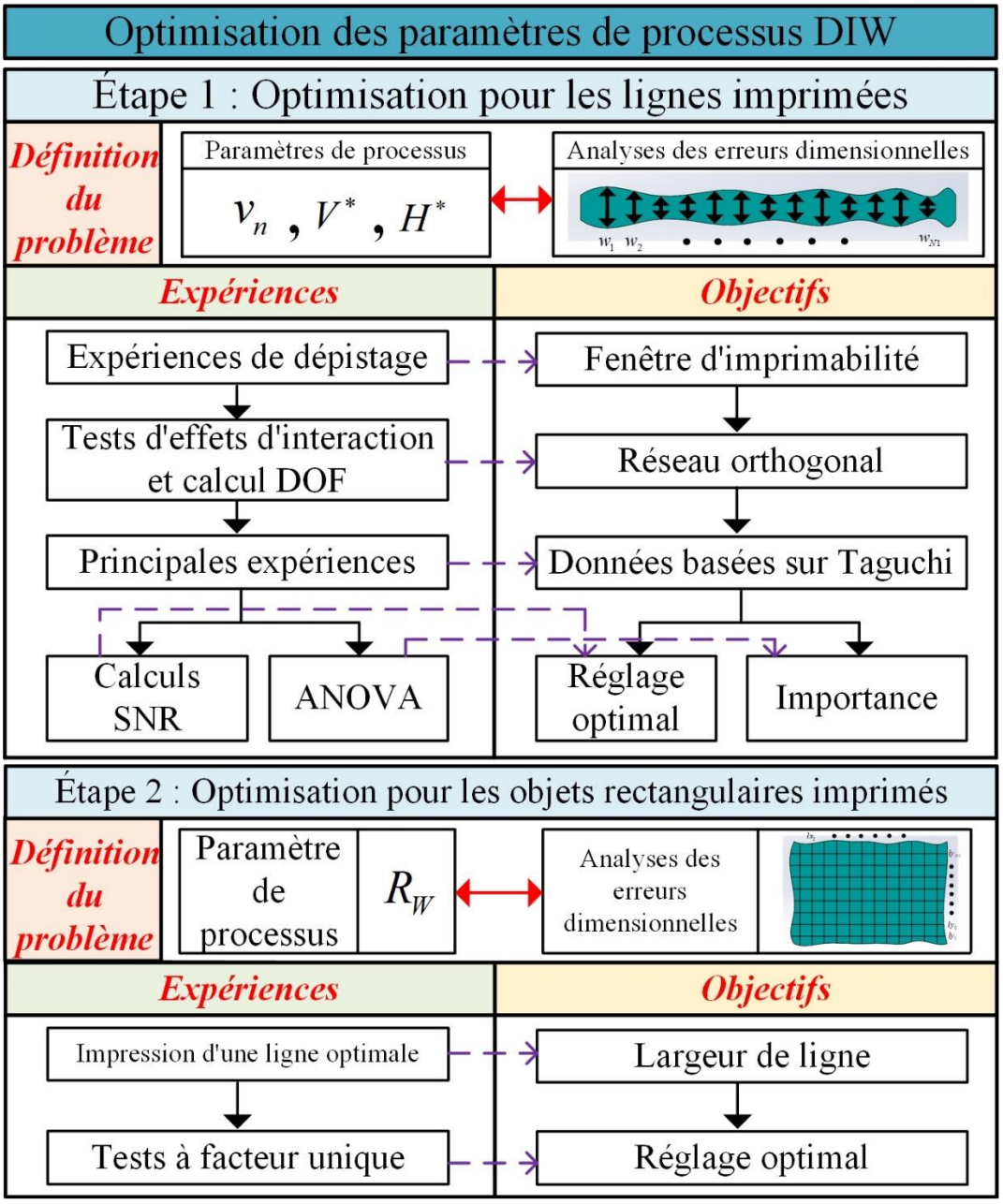

Figure 3.5 Cadre de la méthode en deux étapes proposée pour optimiser les paramètres du processus DIW pour les couches imprimées

4 Modélisation numérique, vérification expérimentale et analyse de processus DIW

Les résultats de la modélisation pour DIW incluent le filament extrudé de forme libre (FEF), le filament déposé (DF), le coin déposé, la couche imprimée et la pièce 3D. Cette thèse porte sur les simulations numériques des éléments les plus basiques en DIW : FEF, DF et coin déposé.

Premièrement, la méthode du volume de fluide (VOF) est sélectionnée comme méthode de simulation numérique et elle est brièvement décrite. Ensuite, des simulations numériques, des vérifications expérimentales et des analyses de processus DIW sont menées.

Pour la simulation numérique de FEF, il existe peu de travaux sur la modélisation et l'évaluation de FEF basés sur des méthodes de simulation numérique pour DIW. La modélisation par simulation numérique du FEF doit tenir pleinement compte des propriétés de l'encre et des paramètres de processus, car la qualité du FEF dépend à la fois des propriétés du matériau de l'encre et du réglage des paramètres de processus [119]. L'évaluation du FEF doit tenir compte à la fois du diamètre moyen et de la stabilité car ces deux indicateurs ont l'influence la plus significative sur la qualité d'impression [172]. L'objectif de la modélisation de processus et de l'analyse de FEF basée sur des simulations numériques est d'établir un modèle de FEF avec une méthode de simulation numérique, puis d'évaluer le FEF sur la base de ce modèle. Tout d'abord, un modèle de FEF est établi à l'aide d'une méthode de simulation numérique et deux indicateurs d'évaluation, le diamètre moyen et la stabilité, sont proposés pour évaluer le FEF. Enfin, l'encre sélectionnée, Nivea Crème, est utilisée sous trois niveaux de vitesse de piston pour vérifier la simulation numérique. Après vérification expérimentale, le modèle et les indicateurs d'évaluation sont utilisés pour analyser l'effet de la vitesse du piston sur le FEF et trouver des fenêtres imprimables appropriées pour les paramètres de processus.

Pour la simulation numérique de DF, plusieurs chercheurs ont établi des modèles de prédiction numérique pour DF dans MEAM. Comminal et al. [147] ont établi un modèle numérique des filaments déposés dans le MEAM (Material Extrusion Additive Manufacturing) mais ce travail manquait de validation expérimentale. Serdeczny et al. [173] ont utilisé une procédure expérimentale pour valider le modèle numérique et ont étudié l'influence des conditions de traitement sur la section d'un fil imprimé par extrusion de matériau FA à travers un modèle numérique. Gohl et al. [144] ont utilisé un outil de simulation de dynamique des fluides computationnelle (CFD) pour étudier l'effet des paramètres d'impression sur les filaments déposés en bio-impression. Goset et al. [174] ont présenté une étude numérique du

dépôt d'un simple brin d'acide polylactique (PLA) par MEAM via un modèle CFD. Bien que les travaux précédents aient montré que le DF est significativement influencé par les paramètres du processus, ils n'ont souvent pas réussi à réaliser des caractérisations quantitatives complètes de l'influence détaillée des paramètres du processus sur l'état de dépôt et la dimension du profil des filaments déposés. Pendant ce temps, il existe peu de travaux sur la prédiction numérique des filaments déposés dans DIW en tenant pleinement compte des propriétés du matériau de l'encre et du réglage des paramètres de processus. Ainsi, il est crucial et souhaitable d'étudier et de prédire pleinement l'état de dépôt et la dimension du profil des filaments déposés dans les processus DIW basés sur la prédiction numérique. Dans ce chapitre, un modèle de prédiction numérique 3D amélioré des filaments déposés dans DIW est établi avec la méthode du volume de fluide (VOF) pour prédire l'état du dépôt et la dimension du profil des filaments déposés. Des expériences de dépôt de filaments sont menées en utilisant l'encre sélectionnée pour vérifier le modèle proposé. En utilisant le modèle numérique proposé, l'état du dépôt est divisé en trois états et la dimension du profil sous chaque état est prédite. L'effet des paramètres de processus, y compris la vitesse de la buse sans dimension et la hauteur sans dimension sur l'état du dépôt et la dimension du profil, a été quantifié pour la première fois à l'aide de simulations numériques. La simulation numérique du DF démontre une approche efficace et économe en matériaux pour la prédiction de l'état de dépôt et de la dimension du profil du DF et l'étude des effets des paramètres de processus dans DIW avec des simulations numériques informatisées.

Quand à la simulation numérique du coin déposé, pour bien comprendre le processus DIW et améliorer la qualité géométrique des pièces en DIW, les méthodes de simulation numérique ont été largement utilisées pour modéliser le processus MEAM [144, 147, 149, 175]. Grâce aux avantages des simulations numériques proposées, les chercheurs ont évalué avec succès l'imprimabilité de nouvelles encres préparées, trouvé les paramètres de processus optimisés, analysé le processus d'extrusion de matériau et réalisé le jumeau numérique du processus MEAM avec une faible consommation de matériau et de temps expérimental [176- 178]. Comminal et al. ont simulé le dépôt de brins [147] et le dépôt de matériau le long d'un parcours d'outil avec un coin pointu [149] avec des modèles de dynamique des fluides computationnelle (CFD) pour étudier l'effet des paramètres de processus sur les filaments et les coins déposés, respectivement. Gohl et al. [144] ont mené des simulations informatiques pour DIW afin d'évaluer les encres nouvellement développées. Tu et al. [175] ont établi un modèle de filaments extrudés de forme libre avec simulation numérique, puis ils ont évalué les filaments sur la base du modèle pour DIW. Cependant, les travaux antérieurs [149] pour la simulation numérique des coins déposés ne pouvaient réaliser la simulation de coin que sous la condition d'un petit

angle inférieur à 90 ° mais n'ont pas réussi à réaliser la simulation de coin de n'importe quel angle. Ainsi, pour surmonter les limites des recherches précédentes sur la simulation numérique des coins déposés et réaliser pleinement la modélisation du processus DIW basée sur l'application de la simulation numérique, il est crucial et nécessaire de proposer une simulation numérique améliorée pour modéliser les coins déposés de n'importe quel angle. Dans ce chapitre, des simulations numériques 3D de coins déposés de n'importe quel angle dans DIW sont établies avec la méthode VOF et des expériences de dépôt de coin sont menées à l'aide de l'encre sélectionnée pour valider la simulation numérique proposée. La simulation numérique du coin de dépôt surmonte la limitation des travaux de recherche antérieurs dans la simulation numérique des coins déposés et démontre une approche efficace pour la prédiction des coins déposés de n'importe quel angle dans DIW avec une simulation numérique informatisée.

Dans ce chapitre, des simulations numériques des éléments les plus élémentaires de DIW, y compris FEF (Figure 4.2), DF (Figure 4.7) et le coin déposé (Figure 4.16), sont développées et des vérifications expérimentales sont effectuées pour vérifier les simulations numériques proposées (Figure 4.4 and Figure 4.9). Sur la base des simulations numériques proposées, des analyses de processus de DIW sont menées.

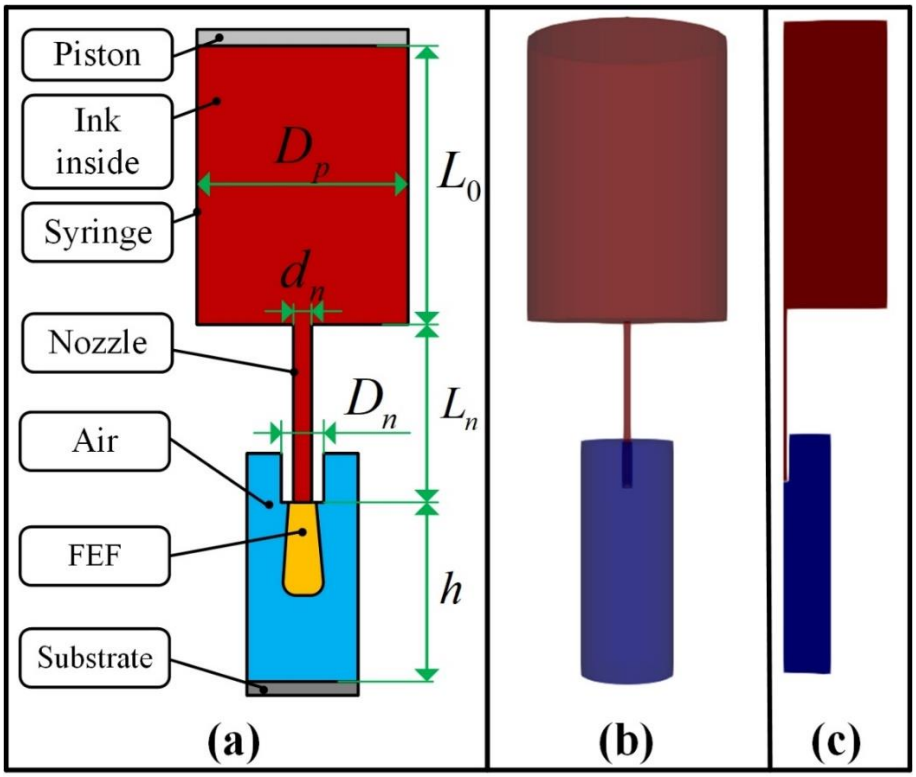

Figure 4.2 Modèle géométrique de FEF en simulation numérique pour DIW : (a) dimensions du modèle géométrique ; (b) modèle 3D établi au moment initial ; (c) modèle axisymétrique 2D simplifié au temps initial

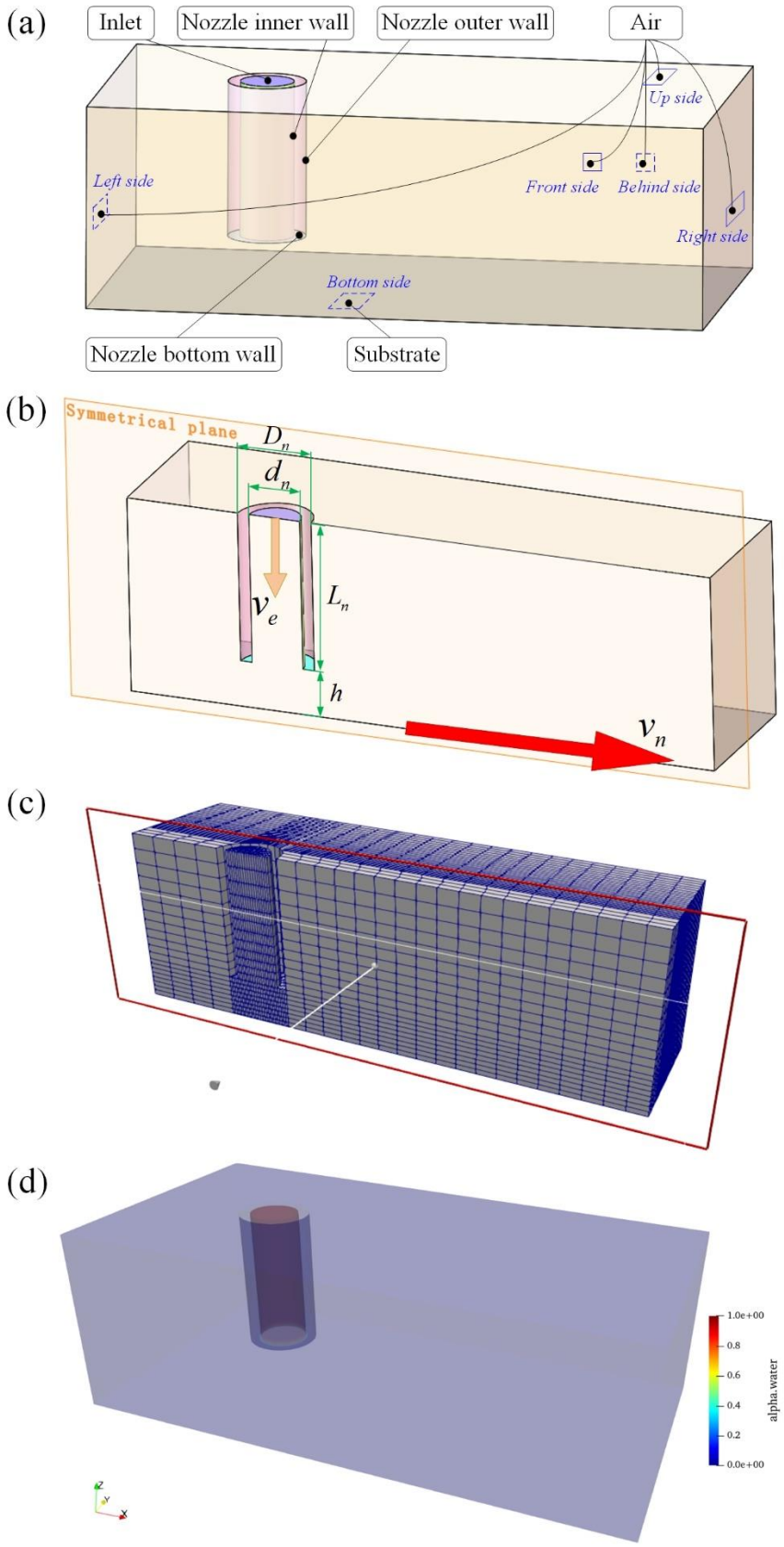

Figure 4.7 Modélisation numérique du profil 3D du DF : (a) modèle géométrique 3D ; (b) les paramètres critiques du modèle ; (c) maillages générés ; (d) condition initiale de la fraction de phase

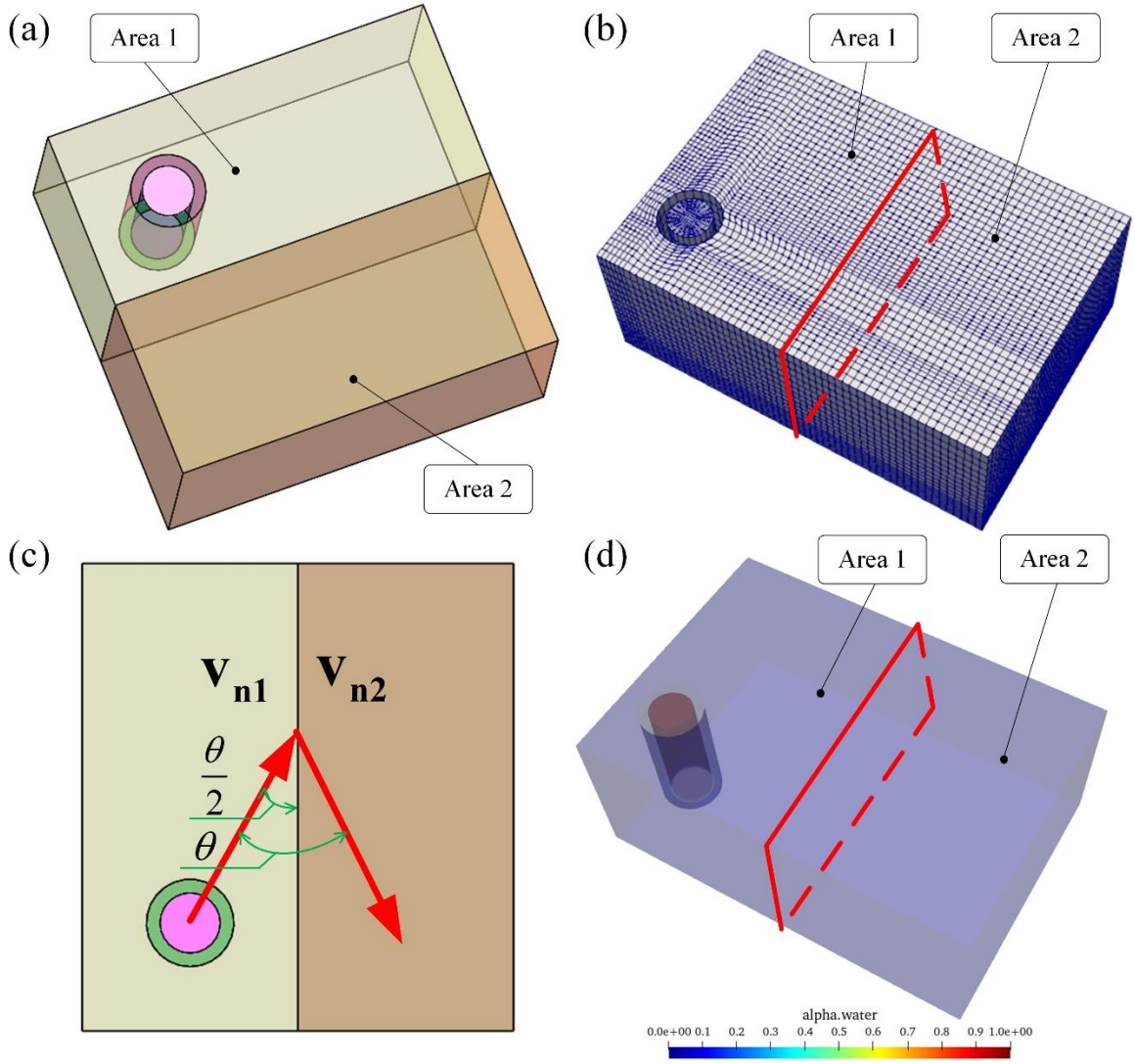

Figure 4.16 Modélisation numérique du profil 3D des coins déposés : (a) modèle géométrique 3D ; (b) maillages générés ; (c) condition de vitesse dans les substrats ; (d) condition initiale de la fraction de phase

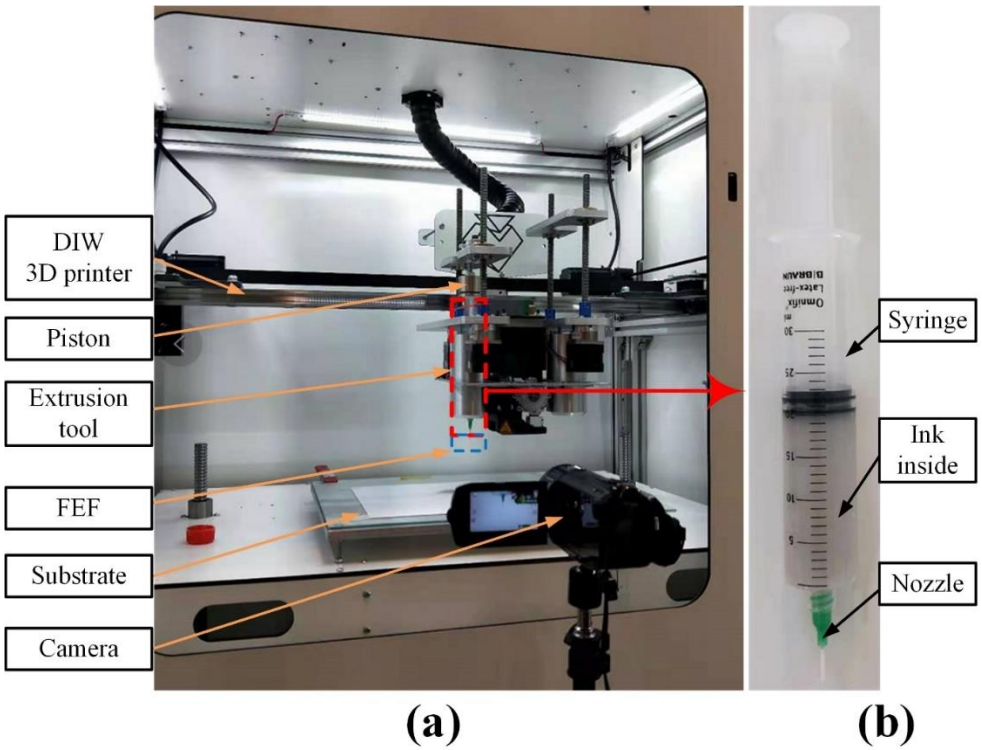

Figure 4.4 Configuration de validation expérimentale pour la simulation numérique de FEF : (a) production de FEF à l'aide d'une imprimante 3D DIW et observation de FEF à l'aide d'une caméra ; (b) outil d'extrusion dans l'imprimante DIW 3D

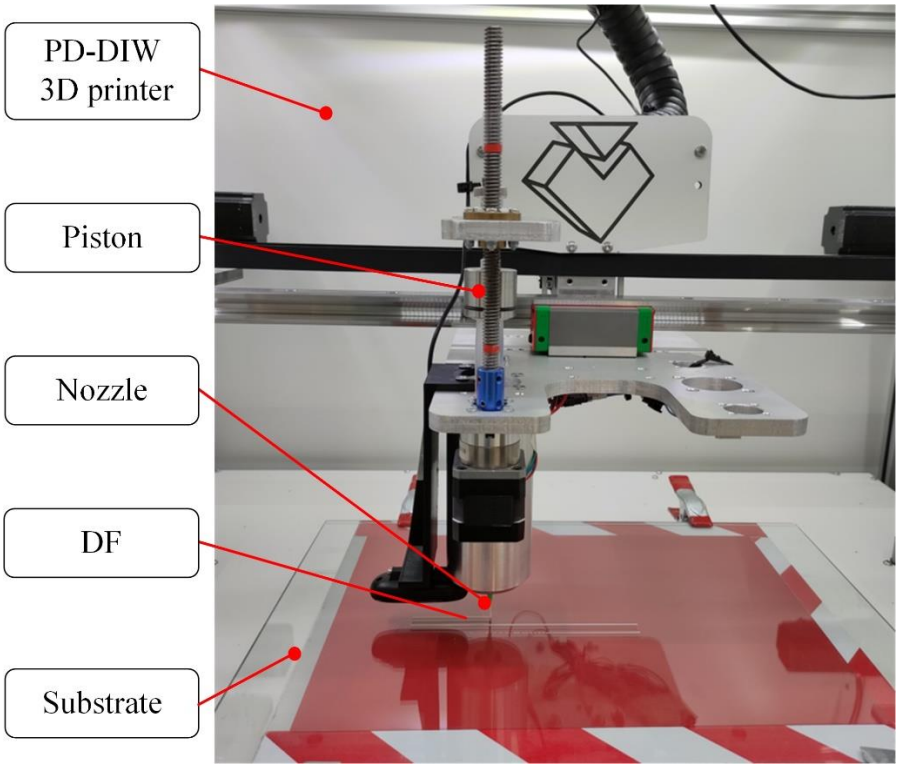

Figure 4.9 Montage expérimental pour des expériences de dépôt de filaments et des expériences de dépôt de coins

Pour la simulation numérique de FEF, un modèle numérique de FEF est établi avec une méthode de simulation numérique, puis le FEF est évalué sur la base de ce modèle. Deux indicateurs d'évaluation, diamètre moyen et stabilité, sont proposés pour évaluer le FEF. L'encre sélectionnée Nivea Crème est utilisée pour vérifier la méthode. Le modèle numérique établi de FEF est vérifié car la forme dans la simulation est conforme aux résultats expérimentaux et la précision de la prédiction du diamètre est meilleure que 0,08 mm. Après vérification expérimentale, le modèle et les indicateurs d'évaluation sont utilisés pour traiter les deux questions de l'analyse de processus pour FEF dans DIW comme suit :

(1) Analyser l'effet de la vitesse du piston sur le FEF : il existe une vitesse minimale du piston, 2 mm/s pour Nivea Crème pour le réglage de ve, pour produire un FEF continu et stable ; les diamètres moyens de FEF diminuent avec l'augmentation de la vitesse du piston. La stabilité diminue d'abord puis augmente avec la vitesse du piston augmente ;

(2) Trouvez des fenêtres imprimables appropriées pour les paramètres de processus : la fenêtre imprimable de réglage de ve est de 5 mm/s à 15 mm/s pour Nivea Crème.

Pour la simulation numérique de DF, l'influence détaillée des paramètres de processus sur l'état de dépôt et la dimension du profil n'a pas été entièrement caractérisée quantitativement dans les précédents travaux de prédiction numérique pour le DF de DIW. Dans ce chapitre, l'effet des paramètres de processus sur l'état du dépôt et la dimension du profil a été quantifié sur la base d'une prédiction numérique. Un modèle numérique 3D amélioré est établi en utilisant la méthode VOF et en considérant les propriétés globales du matériau d'encre. Le modèle numérique 3D amélioré surmonte le problème des modèles 2D simplifiés précédents dans la prédiction de la section transversale. Il surmonte également la lacune des modèles numériques 3D précédents en ignorant les propriétés importantes du matériau telles que le coefficient de tension superficielle et l'angle de contact statique qui limitent la précision de la prédiction. Les paramètres de processus critiques sont identifiés comme étant la vitesse sans dimension de la buse (V*) et la hauteur sans dimension (H*). Sur la base de la prédiction numérique, l'état de dépôt est caractérisé en trois types nommés sur-dépôt, dépôt pressé et dépôt de forme libre (Figure 2.9) et la dimension du profil sous chaque état de dépôt est prédite. L'efficacité de la prédiction numérique pour les filaments déposés est validée car ses résultats sont cohérents avec les résultats expérimentaux et ils sont également cohérents avec les résultats idéaux (théoriques). La précision de la prédiction numérique pour la dimension du profil est vérifiée car les erreurs relatives maximales de largeur et de hauteur entre les résultats expérimentaux et simulés sont respectivement de 10,13 % et 7,37 %, ce qui est significativement amélioré par rapport aux

valeurs rapportées de 20 % et 28 % dans la littérature. L'erreur relative maximale de la prédiction numérique pour la dimension du profil apparaît au bord de la fenêtre imprimable.

Sur la base de la prédiction numérique, les effets des paramètres de processus DF sont également étudiés. L'état de dépôt commence du sur-dépôt au dépôt pressé et enfin au dépôt de forme libre (Figure 2.9) lorsque V* et H* augmentent alors que la vitesse moyenne de l'encre dans la buse n'a pas d'effet significatif sur l'état de dépôt et la dimension du profil. L'état de dépôt doit être pris en considération pour l'effet des paramètres de procédé sur la dimension du profil : la largeur diminue avec V* en dépôt sous pression et en dépôt de forme libre ; la hauteur reste la même avec V* en dépôt pressé alors qu'elle diminue avec V* en dépôt de forme libre ; la largeur diminue avec H* en dépôt sous pression tandis qu'elle reste la même avec H* en dépôt de forme libre ; la hauteur augmente avec H* en dépôt pressé alors qu'elle reste la même avec H* en dépôt de forme libre. La simulation numérique et l'analyse de processus proposées pour DF caractérisent l'état de dépôt et étudient la dimension du profil dans chaque état de dépôt sur la base de l'utilisation de la prédiction numérique. La simulation numérique de DF suggère une prédiction numérique efficace et économe en ressources pour l'état de dépôt et la dimension du profil du DF et l'étude des effets des paramètres de processus dans DIW. Elle fournit également une base viable pour les travaux futurs sur l'élaboration de la modélisation numérique de l'ensemble du processus d'impression 3D DIW.

Pour la simulation numérique des coins déposés, les travaux de recherche antérieurs pour la simulation numérique des coins déposés ne pouvaient réaliser la simulation de coin que dans des conditions de petit angle et n'ont pas réussi à réaliser la simulation de coin de n'importe quel angle. Dans ce chapitre, une simulation numérique 3D améliorée des coins déposés est établie en utilisant la méthode VOF et en considérant les propriétés globales du matériau d'encre. La simulation numérique 3D améliorée surmonte la limitation des travaux précédents et réalise une modélisation de coin déposé de n'importe quel angle en construisant deux zones de calcul (Figure 4.16) où deux vitesses de buse avec l'angle de coin sont appliquées sur les substrats de deux zones de calcul. L'efficacité du modèle numérique proposé est validée par des expériences de dépôt de coins en utilisant l'encre sélectionnée dans une imprimante DIW 3D car les angles de coin simulés correspondent bien aux angles expérimentaux et la valeur maximale de MDDSEO est de 1,06 ± 0,06 mm. On observe que la précision de la simulation dans les coins est inférieure à celle dans les filaments. La raison de ce phénomène est due à la différence entre la vitesse de la buse appliquée sur le substrat dans la simulation numérique et la vitesse réelle de la buse dans les expériences uniquement pour la région d'angle, car la buse a besoin d'un

processus de décélération et d'accélération uniforme pour changer la direction de la vitesse de la buse dans la pratique. impression. Le MDDSEO des coins déposés diminue à mesure que l'angle de coin augmente.

Les simulations numériques de FEF, DF et des coins déposés suggèrent une simulation numérique efficace pour les sorties de modélisation dans DIW qui pourrait être utilisée dans les travaux d'analyse de processus DIW, y compris l'évaluation de l'imprimabilité de nouvelles encres préparées, l'optimisation des paramètres de processus et l'établissement d'un jumeau numérique. Ils fournissent également une base viable pour les travaux futurs sur l'élaboration de la modélisation numérique de l'ensemble du processus d'impression 3D DIW.

5 Conclusion et perspectives

5.1 Conclusion

La compréhension et l'analyse du processus DIW n'ont pas été entièrement étudiées, ce qui limite la précision de fabrication et la promotion de l'application de cette technique. La simulation numérique est l'un des outils les plus puissants d'analyse de processus en FA. L'analyse de processus basée sur des simulations numériques présente des avantages en termes d'économie de temps de matériau/d'essai et de capture facile de la valeur des paramètres de processus critiques qui sont difficiles à obtenir par des mesures expérimentales. La recherche sur la modélisation des processus et l'analyse de DIW basée sur des simulations numériques fournira un soutien important pour le développement et l'orientation de DIW. Cependant, il existe actuellement peu de travaux systématiques sur la modélisation et l'analyse des processus basés sur des simulations numériques pour DIW. Pour combler cette lacune, cette thèse effectue des recherches sur la modélisation et l'analyse des processus DIW .

Dans le chapitre 2, l'examen systématique de la littérature sur le DIW est effectué d'abord pour résumer les caractéristiques, le développement, les défis et les solutions aux défis de DIW et un problème insuffisamment résolu - la difficulté de trouver rapidement des paramètres de processus appropriés pour l'encre préparée - est déterminé comme la question de recherche de cette thèse. Pour résoudre la question de recherche, la piste de la modélisation et l'analyse des processus DIW est poursuivie pour résoudre le problème. Ensuite, une revue de littérature sur la modélisation et l'analyse de processus DIW est réalisée. Les entrées et les sorties de la modélisation des processus sont résumées et les méthodes de modélisation numérique des processus sont sélectionnées comme les plus appropriées pour la modélisation des processus et l'analyse de DIW. Cependant, il existe actuellement peu de travaux systématiques sur la

modélisation et l'analyse des processus basés sur des simulations numériques pour DIW. Sur la base de l'examen, l'objectif de cette thèse est formulé comme suit : contribuer à la modélisation et à l'analyse de processus DIW sur la base de simulation numérique.

Dans le chapitre 3, l'encre Nivea Crème et une imprimante 3D DIW à piston sont choisies pour vérifier les simulations numériques proposées. Avant la simulation numérique, les propriétés des matériaux d'encre sont caractérisées et le réglage optimal des paramètres de processus est calculé pour fournir la base des entrées de modélisation. Pour la caractérisation des propriétés du matériau de l'encre, la densité, la tension superficielle, l'angle de contact statique et les propriétés rhéologiques sont obtenues pour l'encre utilisée. Pour la sélection des paramètres de processus, les paramètres de processus DIW sont identifiés par des analyses de processus et une méthode en deux étapes est proposée pour optimiser les paramètres de processus DIW pour la précision dimensionnelle et analyser l'importance de chaque paramètre de processus. Des vérifications expérimentales vérifient la méthode de sélection des paramètres de procédé proposée et la robustesse de celle-ci sur d'autres formes et d'autres matériaux. Il a été également analysé l'adaptabilité des paramètres dans l'impression de pièces 3D à partir des analyses des couches imprimées selon la méthode proposée et l'adaptabilité des paramètres dans les constructions fabriquées à 100 % de remplissage ou avec des porosités.

Dans le chapitre 4, des simulations numériques des paramètres principaux de DIW, y compris FEF, DF et le coin déposé, sont proposées et des vérifications expérimentales sont menées pour vérifier les simulations numériques proposées. Sur la base des simulations numériques proposées, des analyses de processus DIW sont menées.

Pour la simulation numérique de FEF, le modèle numérique établi de FEF est vérifié car la forme dans la simulation est conforme aux résultats expérimentaux et la précision de prédiction du diamètre est inférieur à 0,08 mm. L'analyse du processus basée sur la simulation numérique du FEF montre que : 1) il existe une vitesse de piston minimale, 2 mm/s pour Nivea Crème pour produire un FEF continu et stable ; 2) les diamètres moyens de FEF diminuent avec l'augmentation de la vitesse du piston et la stabilité diminue d'abord puis augmente quand la vitesse du piston augmente ; 3) des fenêtres imprimables appropriées sont trouvées dans l'intervalle de 5 mm/s à 15 mm/s pour Nivea Crème.

Pour la simulation numérique de DF, l'effet des paramètres de processus sur l'état de dépôt et la dimension du profil a été quantifié sur la base de la prédiction numérique de DF. Un modèle numérique 3D amélioré est établi en utilisant la méthode VOF et en considérant les propriétés globales du matériau d'encre. Le modèle numérique 3D amélioré surmonte le problème des

modèles 2D simplifiés précédents dans la prédiction de la section transversale. Il surmonte aussi la lacune des modèles numériques 3D précédents qui ignorent les propriétés importantes du matériau telles que le coefficient de tension superficielle et l'angle de contact statique qui limitent la précision de la prédiction. Les paramètres de processus critiques sont identifiés comme étant la vitesse sans dimension de la buse et la hauteur sans dimension. Sur la base de la prédiction numérique, l'état de dépôt est caractérisé en trois types nommés sur-dépôt, dépôt pressé et dépôt de forme libre et la dimension du profil sous chaque état de dépôt est prédite.

Pour la simulation numérique des coins déposés, les travaux de recherche antérieurs pour la simulation numérique des coins déposés ne pouvaient réaliser la simulation de coin que dans des conditions de petit angle et n'ont pas réussi à réaliser la simulation de coin de n'importe quel angle. Une simulation numérique 3D améliorée des coins déposés est établie en utilisant la méthode VOF et en considérant les propriétés globales du matériau d'encre. La simulation numérique 3D améliorée surmonte la limitation des travaux précédents et réalise une modélisation de coin déposé de n'importe quel angle en construisant deux zones de calcul où deux vitesses de buse avec l'angle de coin sont appliquées sur les substrats de deux zones de calcul. L'efficacité du modèle numérique proposé est validée par des expériences de dépôt de coins en utilisant l'encre sélectionnée dans une imprimante DIW 3D car les angles de coin simulés correspondent bien aux angles expérimentaux et la valeur maximale de MDDSEO (deviation between simulated and experimental outlines) est de 1,06 ± 0,06 mm. On observe que la précision de simulation dans les coins est inférieure à celle dans les filaments et le MDDSEO des coins déposés diminue quand l'angle de coin augmente.

En conclusion, cette thèse mène de la recherche à travers des revues systématiques de la littérature et elle propose un cadre outillé pour la caractérisation des propriétés des matériaux d'encre, la sélection des paramètres du processus, les simulations numériques, la vérification expérimentale et l'analyse des processus DIW. Cette thèse propose une simulation numérique efficace pour les sorties de modélisation dans DIW qui pourrait être utilisée dans les travaux d'analyse de processus DIW, y compris l'évaluation de l'imprimabilité de nouvelles encres préparées, l'optimisation des paramètres de processus et l'établissement d'un jumeau numérique, ce qui est utile pour la compréhension du processus et l'analyse de processus DIW.

5.2 Perspectives

A la suite des travaux présentés au chapitre 1-4, bien d'autres perspectives peuvent être envisagées. Parmi ceux que j'espère suivre, il y a :

Pour la sélection des paramètres de processus, l'analyse quantitative des objets imprimés est limitée et la thèse n'obtient pas de relation quantitative entre l'entrée et la sortie basée sur la méthode expérimentale. Les travaux futurs mèneront une évaluation quantitative des objets imprimés à l'aide de la méthode de vision par ordinateur et une relation quantitative entre l'entrée et la sortie sera proposée sur la base des données quantitatives à l'aide de la méthodologie de surface de réponse.

Pour les simulations numériques de DIW, la thèse n'établit pas de simulations numériques de couches imprimées et de pièces 3D. Les travaux futurs établiront des simulations numériques des couches imprimées et des pièces 3D pour réaliser la modélisation de toutes les sorties pour DIW, y compris FEF, DF, coins déposés, couches imprimées et pièces 3D.

Pour l'analyse du processus de DIW, la thèse n'analyse pas complètement le processus dans l'évaluation de l'imprimabilité des nouvelles encres préparées, l'optimisation des paramètres du processus et la mise en place du jumeau numérique. Les travaux futurs mèneront un travail complet d'analyse des processus, y compris l'évaluation de l'imprimabilité des nouvelles encres préparées, l'optimisation des paramètres du processus et l'établissement d'un jumeau numérique, ce qui est utile pour la compréhension et l'analyse du processus DIW.

Listes de publications

Articles de journaux :

[1] **Yongqiang Tu**, Javier A. Arrieta-Escobar, Alaa Hassan, et al. Optimizing Process Parameters of Direct Ink Writing for Dimensional Accuracy of Printed Layers [J]. 3D Printing and Additive Manufacturing, 2021, published online. DOI: 10.1089/3dp.2021.0208

[2] **Yongqiang Tu**, Alaa Hassan, Javier A. Arrieta-Escobar, et al. Modeling and evaluation of freeform extruded filament based on numerical simulation method for direct ink writing [J]. The International Journal of Advanced Manufacturing Technology, 2022, 120: 3821-3829. DOI: 10.1007/s00170-022-08999-3

[3] **Yongqiang Tu**, Alaa Hassan, Ali Siadat, et al. Numerical simulation and experimental validation of deposited corners of any angle in direct ink writing [J]. The International Journal of Advanced Manufacturing Technology, 2022, 123: 559-570. DOI: 10.1007/s00170-022-10195-2

[4] **Yongqiang Tu**, Alaa Hassan, Ali Siadat, et al. Analytical modeling of deposited filaments for high viscosity material-based piston-driven direct ink writing [J]. The International Journal of Advanced Manufacturing Technology, 2022, 123: 3387-3398. DOI: 10.1007/s00170-022-

10511-w

Articles de conférence:

[1] **Yongqiang Tu**, Javier A. Arrieta-Escobar, Alaa Hassan, et al. Predictive modeling of extruded filament in the air for bioink in direct ink writing using numerical simulation [C]. Procedia CIRP, 2022, 112(4): 394-399. DOI: 10.1016/j.procir.2022.09.026

[2] **Yongqiang Tu**, Alaa Hassan, Ali Siaddat, et al. Multi-objective optimization based viscosity prediction for inks in direct ink writing numerical simulations [C]. Intelligent Networked Things, CINT 2022, Communications in Computer and Information Science, 2022, 1714: 147-157. DOI: 10.1007/978-981-19-8915-5_13

[3] **Yongqiang Tu**, Huiyun Gong, Alaa Hassan, et al. Computer vision-based evaluation of dimensional accuracy for MEAM in new product development [C]. Accepted. // The CIRP Design conference, 2023, Sydeny, NSW, Australia.

English Version

Chapter 1: General Introduction

1.1 Context and objective of the present study

Additive manufacturing (AM) is an advanced manufacturing technology that directly prints three-dimensional (3D) parts by stacking material layer by layer based on a digital 3D computer-aided design (CAD) model [1-5]. Compared with the traditional manufacturing techniques such as forging, casting, welding and machining (turning, milling, planing, grinding, etc.), AM has the advantages of digitization, material saving, material diversification and the ability to easily manufacture complex parts, which meet the requirements of high precision, structural freedom and customizability for the development of new materials and new structures in tissue engineering, medicine, rubber engineering, ceramic engineering, sensors, aviation, aerospace, electronics, food and other industrial applications [6-10]. According to ISO/ASTM 52900 (2015), AM is divided to seven categories based on the working principle: binder jetting (BJ), directed energy deposition (DED), material extrusion (ME), material jetting (MJ), powder bed fusion (PBF), sheet lamination (SHL) and vat photo polymerization (VPP).

Direct ink writing (DIW) belongs to the material extrusion AM (MEAM) according to the working principle. The working principle of DIW is: first, the material is prepared in paste or slurry type with good printability named ink; then the ink is extruded from a nozzle into continuous filaments using mechanical force (piston or screw drive) or pneumatic force; and finally the filaments are deposited into layer-wise 3D parts [11]. Compared with other AM techniques, DIW has the outstanding advantages in diversity in materials and flexibility in equipment [12-14]. Due to the advantages, DIW has become one of the most popular AM techniques in recent years.

However, the process understanding and analysis of DIW have not been fully studied, which limits the manufacturing accuracy and application promotion of this technique. Both ink material properties and process parameters setting influence the printed results of DIW. Ink material properties include density, surface tension efficient and rheological properties. Process parameters include nozzle inner diameter, syringe diameter, piston speed, nozzle speed and layer height. Thus, it is a challenge to establish a complete and accurate model for DIW due to the complex relationship between inputs and outputs for DIW. In recent studies, due to the lack

of process understanding and analysis of DIW, scholars need to go through numerous trials to find a printable window of ink properties and process parameters suitable for DIW to obtain the printing quality that meets the requirements of use [15-17].This largely increases cost and reduces application attractiveness of DIW. To solve this problem, it is of critical to do research on process modelling and analysis for DIW to fully understand this process and improve the usability of DIW. In conclusion, the research question in the application of DIW: it is of critical to establish a complete and accurate model for DIW because the process understanding and analysis of DIW have not been fully studied, which limits the manufacturing accuracy and application promotion of this technique; however, it is difficult to establish the model of DIW due to the complex relationship between inputs and outputs for DIW.

Numerical simulation is one of the most powerful tools in process analysis in AM. Process analysis based on numerical simulations has advantages in saving material/trial time and easily capturing critical process parameters value which are difficult obtained by experimental measurements. The research on process modeling and analysis of DIW based on numerical simulations will provide important support for the development and guidance of DIW. However, there is currently few systematic research works on process modeling and analysis based on numerical simulations for DIW. To bridge this gap, the objective of this thesis is to improve process modeling and analysis for DIW based on numerical simulations.

1.2 Research contents

Specially, DIW process is influenced by both ink material properties and process parameters. Besides, ink material properties and process parameters are input conditions in numerical simulations. Thus, firstly, ink material properties characterization and process parameters selections are studied and the research results are used as input conditions for the numerical simulations. Then, numerical simulations for DIW are conducted. As one of the AM technologies, as shown in Figure 1.1, the whole process steps of DIW include:

- Step 1: 3D geometrical modeling using top-down design in 3D modeling software like Solidworks, ProE, UG, CATIA,3DMAx, etc.; or using reversal design based on the 3D model data from virtual reality technology or 3D scanner;
- Step 2: G-code generation by importing STL format of 3D geometrical model and setting process parameters in Slicer software;
- Step 3: Printing in a DIW 3D printer using the generated G-code through the layer-wise manufacturing process.

Specially, DIW can print arbitrarily complex 3D parts through ink extrusion, points-to-line, lines-to-layer, and layers-to-3D part processes as illustrated in Step 3 chart in Figure 1.1. Among this process, freeform extruded filament (FEF), deposited filament (DF) and deposited corner are the most basic and critical elements (Step 3 chart in Figure 1.1). Thus, the thesis focuses on the numerical simulations and process analyses of these basic and critical elements: FEF, DF and deposited corner.

In conclusion, to achieve the objective of the thesis, research contents include:

- Research on ink material properties characterization and process parameters selection;
- Research on numerical simulation of basic and critical elements in DIW including FEF, DF and deposited corner;
- Experimental verifications of the proposed numerical simulations;
- Process analysis based on the proposed numerical simulations.

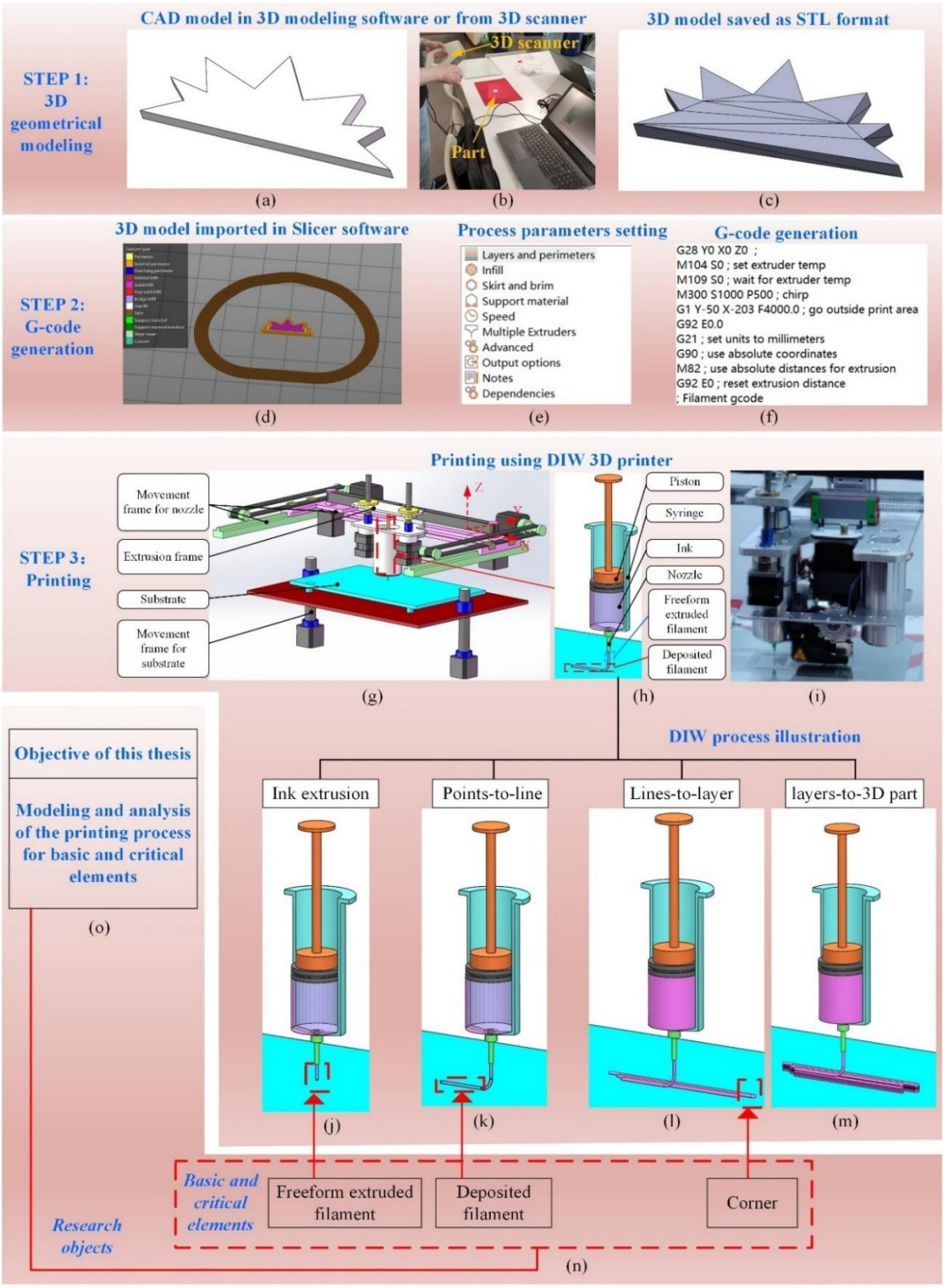

Figure 1.1 Process illustration of DIW and summarized research object in this thesis: (a) CAD model built in 3D modeling software; (b) CAD model from 3D scanner; (c) CAD model saved as STL format; (d) 3D model imported in Slicer software; (e) process parameters setting in Slicer software; (f) generated G-code using Slicer software; (g) mechanical composition of DIW 3D printer;(h) ink in the syringe; (i) real photo of DIW 3D printer; (j) ink extrusion process; (k) points-to-line process; (l) lines-to-layer process; (m) layers-to-3D part process; (n) basic and critical elements in DIW process; (o) summarized research object

1.3 Thesis structure

This thesis is structured in five chapters and the content of each chapter is briefly introduced as follows:

Chapter 1 gives an overview of the research context and objective. Based on the research objective, research contents are summarized. Finally, the thesis structure is outlined.

Chapter 2 studies the state of the art, a systematic literature review of DIW is conducted firstly to summarize features, development, challenges and solutions for challenges of DIW.As results, insufficiently solved problem is determined and the related research question of this thesis is formalized. To answer the research question, process modeling and analysis for DIW is selected as approach. Afterwards, a literature review of process modeling and analysis for DIW is conducted. Inputs and outputs of process modeling of DIW are summarized and numerical process modeling methods are selected as the most suitable method for process modelling and analysis of DIW. Finally, the objective of this thesis is determined based on the literature review.

Chapter 3 presents the works on ink material properties characterization and process parameters selection to provide the basis for modeling inputs. For ink material properties characterization, density, surface tension, static contact angle and rheology properties are obtained for the used ink. For process parameters selection, DIW process parameters are identified through printing analyses and a two-step optimization method is proposed to optimize DIW process parameters for dimensional accuracy of printed layers and analyze the significance of each process parameter.

Chapter 4 presents the numerical simulations of FEF, DF and deposited corners in DIW. Firstly, the numerical simulation method, volume of fluid (VOF), is introduced. Then, numerical simulations of FEF, DF and deposited corners are presented through geometrical modeling, meshes generation, and boundary conditions determination. Then, experimental verifications are conducted to verify the proposed numerical simulations. Finally, process analysis is conducted based on the proposed numerical simulation model.

Chapter 5 presents the conclusion and perspectives of the thesis.

Chapter 2: State of the art

2.1 Introduction

In recent years, DIW has attracted great attention both from academia and industry, and DIW has become one of the most popular AM techniques. However, as a technique that has developed rapidly in recent years, there are still many problems needed to be solved in the practical use of DIW and a thorough state-of-art of DIW is critical to understand its development status and problem. Based on the summarized problem in the state-of-art of DIW, process modeling and analysis using numerical simulations is selected as an effective way to solve the insufficiently solved problem. Thus, a literature review on process modeling and analysis using numerical simulations for DIW is further carried out and research gaps are summarized based on the literature review. Based on the summarized research gaps, detailed objectives are proposed.

The rest of this chapter is organized as follows. Section 2.2 presents the systematic literature review of DIW. The review introduces the criticality of AM technology in Section 2.2.1 firstly. Then, the most commonly used AM techniques are introduced and features of each AM technique are summarized to analyze the advantages and suitable applications of DIW in Section 2.2.2. Afterward, development, challenges and solutions for challenges of DIW are reviewed and an insufficiently solved problem is determined as the research question of this thesis in Section 2.2.3. To solve the research question, process modeling and analysis for DIW is selected as approach. Thus, process modeling and analysis for DIW is reviewed in Section 2.3. Inputs and outputs of process modeling are summarized in Section 2.3.1 and process modeling methods are reviewed in Section 2.3.2. Based on the research gaps summarized in the literature review, Section 2.3.3 identifies the objective of this thesis.

2.2 A literature review on DIW

2.2.1 Criticality of AM technology

Thanks to the layer-wise manufacturing principle, AM is able to build materials into freeform and complex geometries from digitally modeled geometrical objects directly without requiring additional tooling [18] to realize complex structural and functional requirement of

parts. Meanwhile, AM can largely reduce cost of manufacturing by reducing material consumption and labor cost based on automated direct printing. Therefore, AM technology has gained great attention over the past five years in applications ranging from the industrial equipment, to aerospace, automobile making, consumer electronics, biomedicine, education & research, military use, building and other uses [19-23] (Figure 2.1 (a)).Over the past several years, the AM production cost has gone down in terms of low-cost step motors, mechanical components as well as equipment, such as lasers, digital projectors, precision extruders, and a growing library of printable materials has been established for feed stocks. AM's significant business potential and applications have also drawn great attention from materials companies, industries and government organizations. AM industry has now experienced significant growth and production of additively manufactured parts has been increasing at an average annual rate of about 26% for the past 10 years (Figure 2.1 (b)) [24].

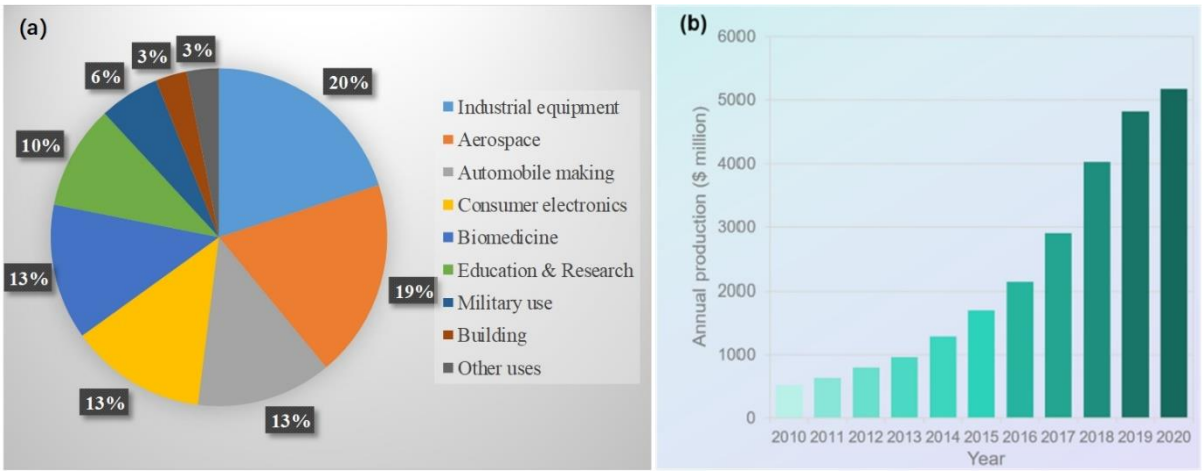

Figure 2.1 (a) AM applications and production share in various sectors and (b) Annual production of AM parts from independent service providers worldwide (in million US dollars)[24]

2.2.2 AM techniques

The AM techniques are divided into seven categories based on the working principle according to ISO/ASTM 52900 (2015). As shown in Figure 2.2, the commonly used AM techniques include: binder jet 3D printing (BJ3DP), laminated object manufacturing (LOM), fused deposition modeling (FDM), direct ink writing (DIW), inkjet printing (IJP), selective laser sintering (SLS), selective laser melting (SLM), powder based directed energy deposition (PBDED), wire based directed energy deposition (WBDED), stereolithography (SL), digital light processing (DLP) and two-photon polymerization (TPP).

2.2.2.1 Binder jet 3D printing (BJ3DP)

BJ3DP belongs to binder jetting AM and BJ3DP is a process in which a liquid binder is jetted on layers of powdered materials, selectively joined, and then followed by densification process [25]. As illustrated in Figure 2.2 (a), in this process, solid powder is spread on a powder bed and a printing head ejects a liquid binder that binds the powder together in the areas same as the slicer of the 3D part in a layer-by-layer sequence. The resolution of BJ3DP is determined by the size and shape of the powder material as well as the feature size of the binder droplet (the typical resolution of BJ3DP is few 100 μm to mm) [26, 27]. The binder solution should have appropriate rheological properties for smooth ejection through the print head. A typical feature generated by the process is a high residual porosity in the printed part, due to the requirement of using rather coarse powders to enable the spreading of defect-free layers. Furthermore, thin features cannot be easily produced using this method [28]. BJ3DP provides very good flexibility in geometry design and is best for the printing of parts for which precision in resolution and surface finish is less of a requirement [29].

2.2.2.2 Laminated object manufacturing (LOM)

LOM belongs to sheet lamination AM and LOM is a process in which layers of adhesive-coated paper, plastic, or metal laminates are successively glued together and cut to shape with a knife or laser cutter (Figure 2.2 (b)). Objects printed with this technique may be additionally modified by machining or drilling after printing. Finally, 3D parts can be obtained after binder removal and sintering. Typical layer resolution for this process is defined by the material feedstock and usually ranges in thickness from one to a few sheets of copy paper. The LOM technique may suffer poor surface quality, delamination, anisotropy along the build direction and planar direction due to weak interfacial bonding between the sheets [30]. The resolution of LOM is in mm. In terms of complexity, LOM is restricted to the fabrication of structures with simple geometries and relatively larger dimensions. Also, the removal of unprocessed material is time-consuming and expensive, causing substantial amount of material waste [31].

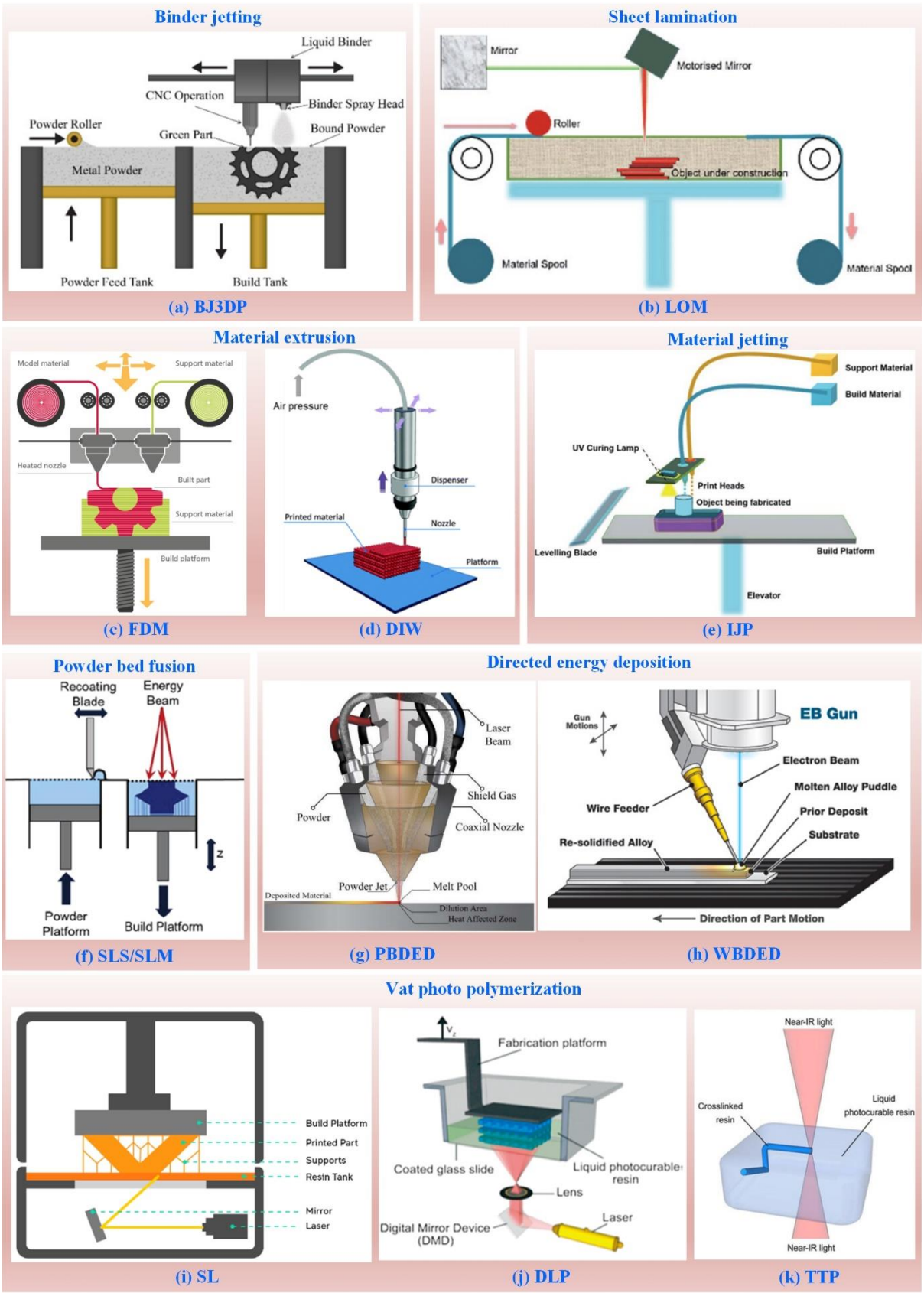

Figure 2.2 Classification and illustrations of different commonly used AM techniques: (a) BJ3DP, (b) LOM, (c) FDM, (d) DIW, (e) IJP, (f) SLS/SLM, (g) PBDED, (h) WBDED, (i) SL, (j) DLP, (k) TTP

2.2.2.3 Material extrusion AM (MEAM)

MEAM has recently become widespread for the layer-by-layer fabrication of 3D parts and components even with highly complex shapes. This technology involves extrusion through a nozzle by means of a plunger-, filament- or screw-based mechanism. MEAM offers greater design freedom, larger building volumes and more cost-efficient production than liquid and powder-based AM processes [32]. This technology mainly contained two techniques: fused deposition modeling (FDM) and direct ink writing (DIW).

(1) Fused deposition modeling (FDM)

FDM process involves the extrusion of thermoplastic composite filaments melted by a moving nozzle which is heated with temperature kept above the glass transition temperature of the polymeric material involved onto a build platform in a layer-by-layer fashion, and the material solidifies immediately on the previously printed layer due to cooling to create 3D objects (Figure 2.2 (c)). The major difference compared with DIW is that heating is involved in the FDM process. The disadvantages of FDM are lower printing resolution (about 100 μm), staircase effect and inherent anisotropy of the printed parts, mainly caused by the filament-based layer-by layer printing process [33].

(2) Direct ink writing (DIW)

As illustrated in Figure 2.2 (d), DIW is an extrusion-based method using a non-Newtonian viscous ink with composed rheological properties and configuration of liquid and solid phases as printing material at room temperature [9]. Similar to FDM, the resolution of DIW is also significantly influenced by the diameter of the nozzle, which can be in the range of dozens to hundreds of micrometers, leading to the staircase effect causing low resolution (100-1200 μm for the x-y layer and 100-400 μm for z resolution), poor surface finish and high anisotropy in geometrical and mechanical properties for the printed parts [34]. However, owing to the wide choice of material and low-cost process, DIW has become increasingly popular for the application needing high freedom in materials with relative low accuracy requirement.

2.2.2.4 Inkjet printing (IJP)

IJP belongs to material jetting AM and this technique was originally introduced for office printing applications but have since then developed also into a valuable tool for research applications and for the fabrication of microstructures. As shown in Figure 2.2 (e), inkjet printing utilizes a dispensing unit to deposit small volumes of liquid material onto a substrate. The major advantage of this technology is the reliable handling of minute amounts of material which can be processed into defined droplets [35]. The resolution of IJP is around 50 μm. The

main limitation of IJP is the technique has limited capability of printing overhanging or hollow structures due to difficulty in support preparation [36, 37].

2.2.2.5 Power bed fusion (PBF)

PBF AM uses either a laser or electron beam to melt and fuse material powder together, which main includes direct metal laser sintering (DMLS), electron beam melting (EBM), selective heat sintering (SHS), selective laser sintering (SLS) and selective laser melting (SLM). Among these techniques, SLS and SLM are most popular in PBF AM techniques as they have better quality in accuracy and mechanical properties.

(1) Selective laser sintering (SLS)

SLS belongs to PBF AM. SLS involves layer-by-layer spreading of powder, followed by selectively scanning and sintering using a high-power laser for bulk joining of the powder to build the final 3D part (Figure 2.2 (f)) [38]. After the SLS process is completed, the printed part is de-powdered and subjected to high temperature treatments for binder removal. SLS does not require extra support structure for hanging components, as the printed part is always embedded in the loose powder bed. The resolution of SLS is 20-150 μm. SLS has been extensively used for the fabrication of a broad range of materials in powder form, such as polymers, metals and composite powders [39-41].

(2) Selective laser melting (SLM)

SLM uses similar mechanism with a laser beam of much higher energy density to fully melt and fuse metallic powders to produce near net-shape parts with near full density (up to 99.9% relative density) in a single step (Figure 2.2 (f)) [42]. SLM is performed under controlled atmospheric conditions and has dominated the metal AM industry for its excellent quality in accuracy and mechanical properties, particularly for manufacturing median to large-size metallic components with topologically optimized structures [43-45]. The resolution of SLM is 20-100 μm.

2.2.2.6 Direct energy deposition (DED)

DED is a metal AM technology where an energy source – usually an electron beam, laser or arc – is directed toward a plate or other substrate material where it impinges with wire or powder feedstock material and melts, leaving deposited material on the substrate [46]. DED techniques are divided into two categories named powder based directed energy deposition (PBDED) (Figure 2.2 (g)) and wire based directed energy deposition (WBDED) (Figure 2.2 (h)) according to the feedstock in powder or wire [47, 48]. Both PBDED and WBDED contain

a robotic arm and a source (electron beam, laser beam process or arc). DED can produce similar parts to those created with conventional machining. Thus, DED is commonly used in parts need to be for applications where conventional manufacture is expensive or slow with in the aerospace, defense, power and marine sectors [49, 50]. Moreover, DED is increasingly replacing conventional methods for the repair of parts such as the repair of damaged turbine blades or propellers [51].

2.2.2.7 Vat photo polymerization (VPP)

VPP utilizes a localized energy source to fuse curable polymeric material for the layer-wise fabrication of 3D geometry [52]. The most commonly used VPP techniques are stereolithography (SL), digital light processing (DLP) and two-photon polymerization (TPP). VPP has the highest resolution among AM techniques: both SL and DLP have resolution below 100 μm and TPP has resolution in sub μm.

(1) Stereolithography (SL)

SL has become vastly popular for its ability to produce high-accuracy, isotropic, and watertight prototypes and parts in a range of advanced materials with fine features and smooth surface finish [53]. As shown in Figure 2.2 (i), SL uses a vat of liquid photopolymers resin that can be cured [54]. The build plate moves in small increments and the liquid polymer is exposed to light where the Ultraviolet (UV) laser draws a cross-section layer by layer. The process repeats until a model is created. The object is 3D printed by pulling the object out of the resin (bottom-up) which creates space for the uncured liquid resin at the bottom of the container and can then form the next layer of the object.

(2) Digital light processing (DLP)

DLP is developed from SL [55]. The major difference of DLP from SLA is that DLP uses a projection of UV light or visible light from a digital projector to flash a single image of the layer across the entire resin at once [56, 57]. In DLP, the digital micro-mirror device (DMD) chip is one important component, which is composed of an array of reflective aluminium micro-mirrors that redirect incoming light from the UV source to project an image of a designed pattern or a layer of a 3D CAD model (Figure 2.2 (j)). The projection of an image that is composed of small square pixels called “voxels” passes through an optical lens and cures the photo-curable polymer resin.

(3) Two-photon polymerization (TPP)

TPP is a maskless direct laser writing technology [58]. In TPP, the light-matter interaction only takes place within the volume of a focused laser spot (Figure 2.2 (k)). The simultaneous

absorption of two photons in the focused spot triggers the locally confined polymerization of an exposed photoresist. The laser focus can be moved through the volume of the photoresist along all three spatial dimensions. Complex 3D structures are written along the laser's trajectory. Thanks to its versatility, TPP fabrication has applications in many fields, including micro optics, photonics, micromechanics, and biomedicine [59-61]. The advantage of TPP is that it has the highest resolution in AM techniques (sub μm). However, it has the disadvantage of slow speed and high cost.

2.2.2.8 Features of each AM technique

Each AM technique has its own features, applicable materials, printing requirement and resolution. Various structural or functional parts manufacturing applications can find the most suitable AM technology according to the features and applicable materials of each AM technology. Features, applicable materials, feedstock form, forming method, printing requirement and resolution of each AM technique are summarized in Table 2.1[24].

Table 2.1 Features, applicable materials, feedstock form, forming method, printing requirement and resolution of each AM technique [24]

AM technique	Features	Applicable materials	Feedstock form	Forming method	Printing requirements	Resolution
BJ3DP	Limited strength and rough surfaces	Metals, sand, ceramics	Slurry & Powder	Binder bonding	Dissolvable in solvents and act as binder	μm to mm
LOM	Low speed and large size, low precision, limited by binder	Paper, plastic, metals, ceramics	Sheets	Stacking and laser cutting	Sheets	mm
FDM	High speed and large size, low precision, limited by extrusion temperature	Thermoplastic polymers	Filament	Extrusion	In filament state	mm
DIW	High speed, low cost, wide choice of materials	Polymers, bio-ink, metals, cement, ceramics	Slurry	Extrusion	Appropriate viscosity and rheological properties	Few 100 μm to mm

Table 2.1 (Continued) Features, applicable materials, feedstock form, forming method, printing requirement and resolution of each AM technique [24]

AM technique	Features	Applicable materials	Feedstock form	Forming method	Printing requirements	Resolution
IJP	Less material quantity, limited by printable inks, low printing speed	Polymers, bio-ink, metals, ceramics	Slurry	Binder bonding	Low viscosity with rapid bonding	Few 100 μm to mm
SLS	Slow speed, high dimensional accuracy	Nylon, metals	Powder	Powder sintering	Meltable by laser	μm to mm
SLM	Slow speed, high dimensional accuracy	Metals	Powder	Powder fusion	Meltable by laser	μm to mm
PBDED	High speed, large size	Metals	Powder	Powder fusion	Meltable by source	μm to mm
WBDED	High speed, large size, low precision	Metals	Wire	Wire fusion	Meltable by source	mm
SL	Moderate speed, moderate cost, high efficiency, good surface quality	Resins, ceramics	Slurry	Linear polymerization	Dissolvable and UV photocurable moieties	Sub 100 μm
DLP	High speed, moderate cost, high efficiency, good surface quality	Resins, ceramics	Slurry	Linear polymerization	Dissolvable and UV photocurable moieties	Sub 100 μm
TPP	Slow speed, high cost, fine surface quality, highest printing precision	Resins, ceramics	Slurry	Non-linear polymerization	Dissolvable and two-photon absorption moieties	Sub μm

Comparisons of diversity in materials, cost, speed, resolution of each AM techniques are listed as follows:

(1) Diversity in materials

DIW> IJP >LOM>BJ3DP>FDM >SL, DLP, TPP>SLS>SLM, PBDED, WBDED

(2) Cost

SLM >SLS>PBDED >WBDED>TPP>SL>DLP>IJP>BJ3DP>LOM>FDM>**DIW**

(3) Speed

IJP, BJ3DP >DLP>LOM> **DIW**>FDM> WBDED>PBDED>SLM>SLS>SL>TPP

(4) Resolution

TPP>SL>DLP>SLM>SLS>PBDED>IJP>BJ3DP>**DIW**>FDM>WBDED>LOM

(5) Manufacturing scales

DIW, FDM, WBDED>IJP, BJ3DP>LOM>SLS, SLM, PBDED>SL, DLP>TPP

(6) Ability to produce lightweight and optimized parts

TPP>SL, DLP>SLM, SLS, PBDED>IJP>BJ3DP>WBDED>FDM, **DIW** >LOM

According to the comparisons of each AM technique, DIW has the outstanding advantages in diversity in materials, low cost and also has competitiveness in speed. Particularly, diversity in materials make DIW as one of the most popular AM techniques. But DIW is not as good as VPP, PBF and IJP in resolution. Thus, DIW is often used in applications when printing resolution and surface roughness are not the primary concerns and as long as the prepared ink can possess specific rheological characteristics. Material currently suitable for DIW include polymer material, biological material, conductive metal material, cement, ceramic material and functional material. As shown in Figure 2.3, the application fields of DIW using the mentioned materials cover rubber engineering [62], tissue engineering [63], batteries [64], electronic circuits [65], buildings [66], ceramic engineering [67], sensors and 4D printing [68]. It is foreseeable that more and more new materials will be prepared as inks suitable for DIW and applied in more applications needing structural or functional materials or parts.

Figure 2.3 Suitable materials and corresponding applications for DIW: (a) polymer ink in rubber engineering[62]; (b) biological ink in tissue engineering[63];(c) metal ink in batteries[64], electronic circuits[65]; (d) cement ink in buildings[66];(e) ceramic ink in ceramic engineering[67]; (f) functional ink in 4D printing and sensors [68]

2.2.3 Development and challenges of DIW

2.2.3.1 Development of DIW

DIW, which is also named as Direct Write Fabrication [69] and Robocasting [70], was firstly proposed by Cesarano et al. in 1998 [71] and was patented in 2000 (US Patent: US6027326A) [72]. As shown in Figure 2.4 (a), The published patent describes the principle of DIW as: the ink is put into a syringe with a precision nozzle firstly; then, the ink is extruded to form extruded filaments and the nozzle is moved by computer control in a two dimensional (2D) pattern of each layer; finally, the nozzle is moved vertically and 3D parts are achieved by layer-by-layer accumulation. Further, the ink requirements are also illustrated in Figure 2.4 (b): (1) a shear thinning viscosity characteristic during extrusion to ensure good printability; (2) a

good shape retention characteristic when stacked after extrusion. Figure 2.4 (c) shows the 3D parts constructed by DIW.

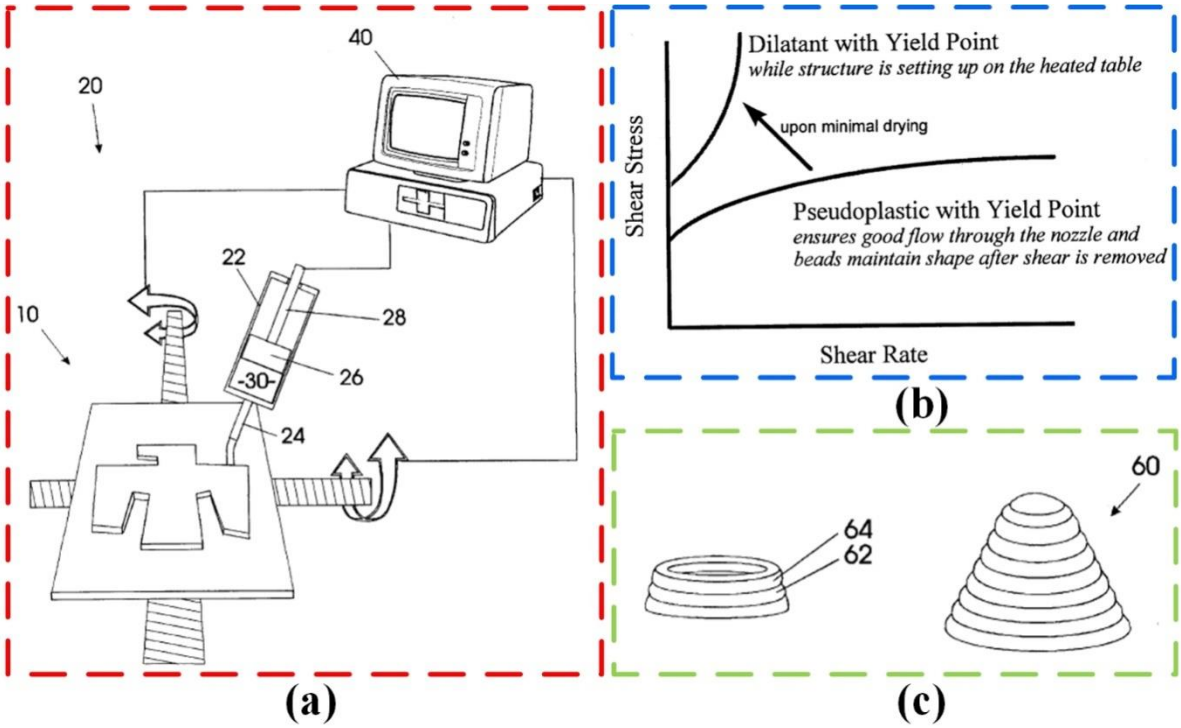

Figure 2.4 DIW technique proposed in the patent in 1998: (a) working principle, (b) ink requirements, (c) 3D parts constructed by DIW[72]

After the patent was disclosed, many research institutions discovered the obvious advantages of material compatibility, low cost and high efficiency of DIW compared with other AM techniques, and then carried out studies on material, process and applications for this technique. The more famous ones are Lewis Laboratory of Harvard University, DREAMS Lab of Virginia Tech, Manufacturing Processes and Machinery Lab of Washington State University, Swiss Federal Laboratories for Materials Science and Technology. Among them, the Lewis Lab of Harvard University has made the greatest contribution. Lewis Lab has been focusing on DIW since it was public. With more than 20 years of research, it has made significant contributions to its theoretical research, material preparation, process modeling, application and industrialization, which has greatly promoted the development and application of DIW. As shown in Figure 2.5, Lewis lab has firstly prepared new materials and pioneered the application in many new fields: in 2012, they prepared silk/hydroxyapatite(HA) ink for tissue engineering [73]; in 2013, they prepared lithium oxide ink for batteries [34]; in 2014, carbon ink was developed for electronics [74]; in 2015, wearable sensors were prepared using ion conductive ink [75]; in 2016, cellulose inks and polymer inks were prepared and were successfully applied to 4D printing [76] and soft robotics [77], respectively; in 2017, silver nano-ink was developed

for radio frequency devices [78]. The focus and key technology of Lewis Lab research is to analyze and control the rheological properties of ink, so that the filaments printed by DIW can be directly stacked layer by layer at room temperature and maintain good shape stability.

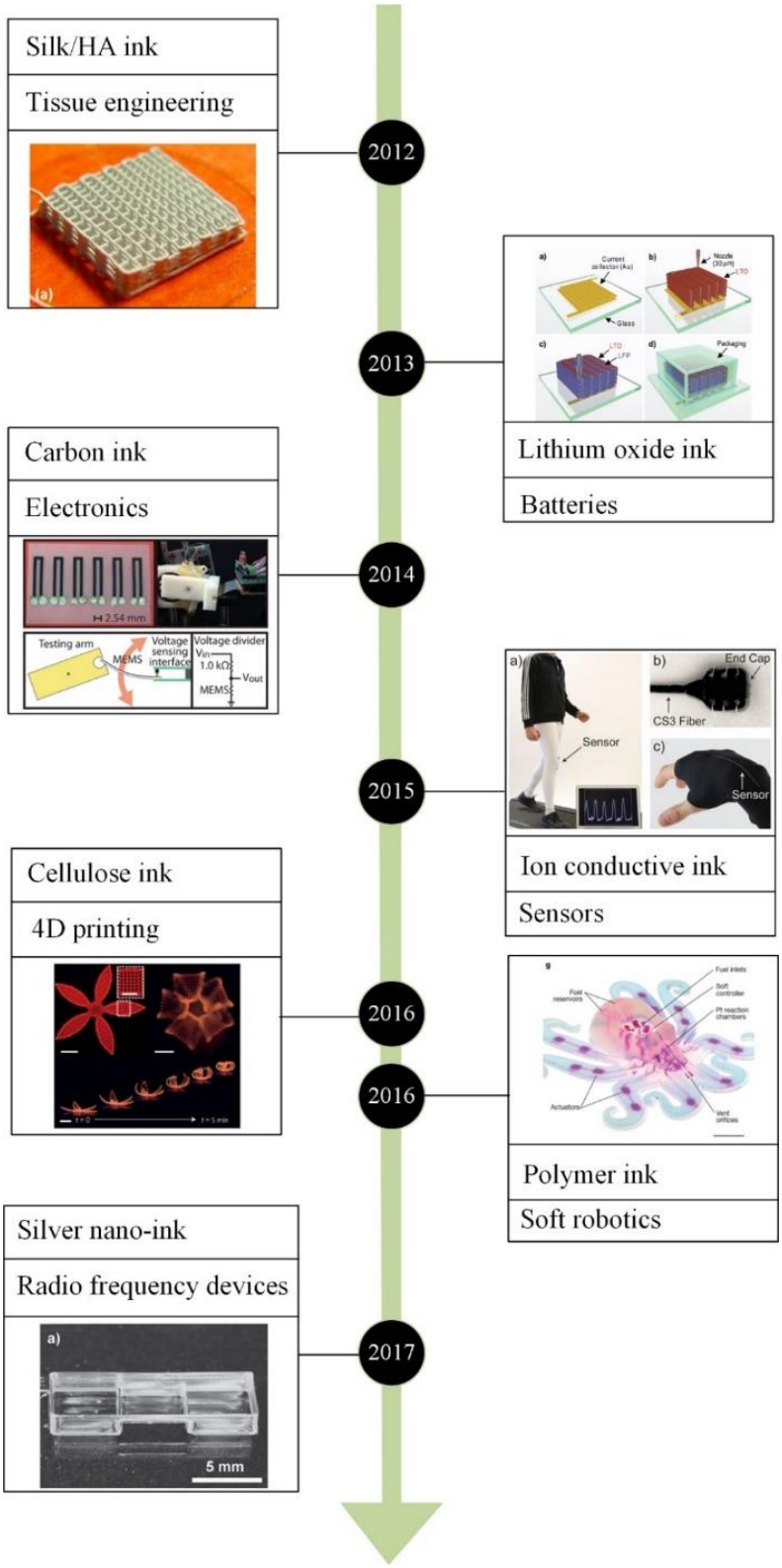

Figure 2.5 Contributions of Lewis lab on DIW in recent years[73], [34], [74], [75], [76], [77], [78]

Nowadays, with the development of DIW on materials, process and applications, DIW has become as one of the most popular AM techniques.

2.2.3.2 Extrusion and deposition forms of DIW

(1) Extrusion methods

Extrusion methods of DIW include pneumatic force-driven, piston-driven and screw-driven (Figure 2.6). The ability to extrude the viscosity of the ink material is: pneumatic force-driven<piston-driven<screw-driven. Compared with the pneumatic force-driven and screw-driven DIW, piston-driven DIW has advantage in flow rate stability as the flow rate in piston-driven DIW is dependent only on the piston movement [79], which is of great benefit to the quality of printed parts [80].

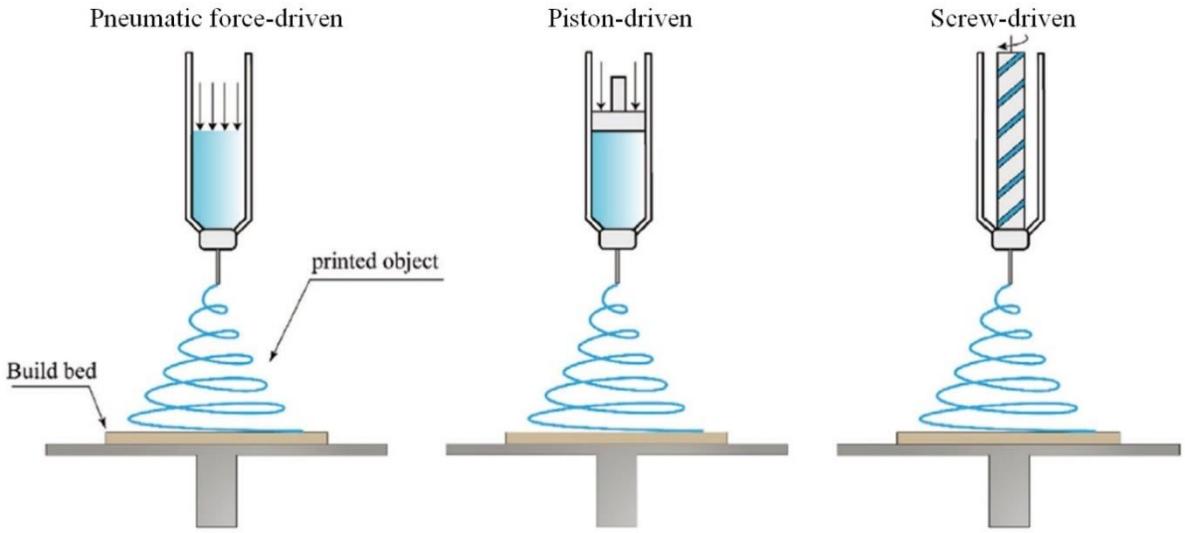

Figure 2.6 There extrusion methods of DIW: pneumatic force-driven, piston-driven and screw-driven [81]

(2) Deposition forms

For ink deposition, two strategies are used according to self-support ability of inks in DIW [82] (Figure 2.7): the first one is to prepare high viscosity inks with shear-thinning and viscoelastic properties which can be extruded from a nozzle and have self-support ability after deposition to form 3D parts in room temperature directly (Figure 2.7 (a)) [83, 84]; the second one is to use assisted-deposition methods like UV-thermal curing (Figure 2.7 (b)) [85], suspended hydrogels (Figure 2.7 (c)) [86] or chemical process (Figure 2.7 (d)) [87] for inks with low viscosity and poor self-support ability. Compared with the low viscosity material based DIW with assisted-deposition systems, high viscosity material based DIW has advantage of low cost, high processing efficiency and high accuracy [88, 89]. Thus, due to the advantages of piston-driven extrusion method and direct deposition forming method based on high

viscosity material in DIW, high viscosity material based piston-driven DIW is the most popular choice in DIW. Thus, the term "DIW" in this thesis refers specifically to high viscosity material based piston-driven extrusion DIW.

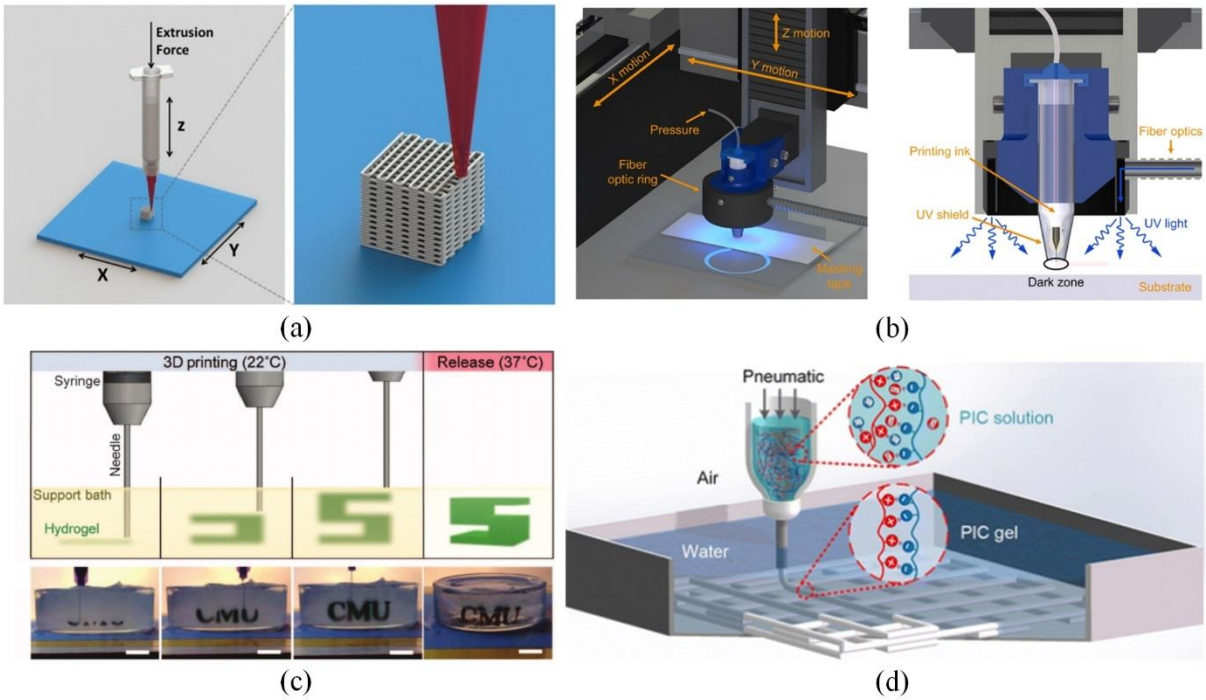

Figure 2.7 Deposition strategies for DIW: (a) deposition directly; (b) deposition with UV-thermal curing [85]; (c) deposition with suspended hydrogels [86]; (d) deposition with chemical process [87]

2.2.3.3 Challenges and solutions of DIW

(1) Challenges of DIW

As a technique that has developed rapidly in recent years, although many scholars have done a lot of research on the development of DIW, there are still many challenges need to be solved to improve smooth surface finish, dimensional accuracy and properties (mechanical and functional) for the promotion and industrialization of DIW. The main challenges of DIW are summarized as follows [9]:

(1) Difficulty in building large overhangs or spans with perfect geometrical accuracy despite using ink with optimized rheology;

(2) Difficulty in ink preparation with optimized rheology: the ink needs to flow easily under shear stress and rapidly recovers and retains its shape upon deposition;

(3) Difficulty to extrude ink through extremely small to print high resolution parts as clogging;

(4) Difficulty to quickly find suitable process parameters for the prepared ink.

(2) Solutions of the challenges of DIW

Many scholars have done various research to come up with suggestions and references to solve the challenges. The solutions to the above challenges proposed by scholars are summarized as follows:

(1) For question (1), the researchers used sacrificial supports to grow the range of geometries that can be manufactured by the DIW [90];

(2) For question (2), the research hotspot mainly focus on the preparation of ink and then select the best ink using rheological characterization using rheology tests including shear stress ramp test, shear rate sweep test, frequency sweep test and recovery test [67];

(3) Question (3) can be avoided by using an appropriate surface lubricant such as oleic acid to reduces the friction between particles and agglomeration formation [91] and by improving nozzle designs [92];

(4) For question (4), scholars need to go through numerous trials to find a printable window of ink properties and process parameters suitable for DIW to obtain the printing quality that meets the requirements of use [15-17].

The main reason of question (4) is the research on the modelling and analysis of the DIW process is very lacking as the process modeling and analysis of DIW have not been fully studied, which limits the manufacturing accuracy and application promotion of this technique. The question largely increases cost and reduces application attractiveness of DIW. To solve this problem, it is critical to do research on process modeling and analysis for DIW.

2.2.4 Discussion

Over the past five years, AM technology has gained a great attention and has been successfully used in various applications showing a great business potential. Owing to the outstanding advantages in diversity in materials and flexibility in equipment, DIW has become one of the most popular AM techniques and researchers have done numerous works on DIW for its application promotion. However, as a technique that has developed rapidly in recent years, there are still many challenges need to be solved for DIW. Specially, the research on the analysis of the DIW process is very lacking as the process modeling and analysis of DIW have not been fully studied, which limits the manufacturing accuracy and application promotion of this technique. To solve this problem, it is critical to do research on process modeling and analysis for DIW.

2.3 A literature review on process modeling and analysis for DIW

2.3.1 Input and output of process modeling for DIW

The purpose of process modeling for DIW is to construct the relationship between input and output in the printing process in order to predict the output according to the input before printing.

2.3.1.1 Input of process modeling for DIW

For the input, the quality of DIW depends on the material properties of the ink including density, surface tension and viscosity [93-95] and the DIW process setting includes nozzle inner diameter, syringe diameter, piston speed, nozzle speed and layer height [96]. Thus, in process modeling for DIW, the inputs are the material properties of the ink and the printing process parameters setting (Figure 2.8).

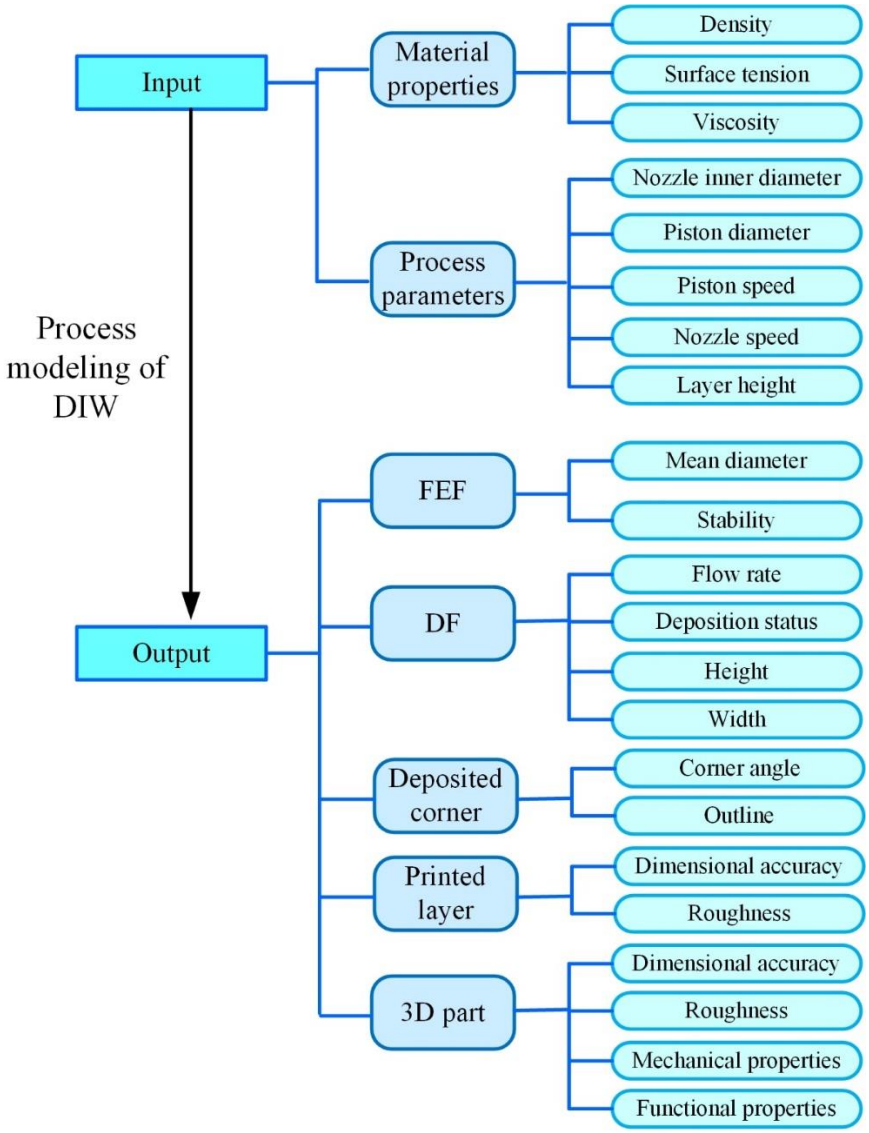

Figure 2.8 Input and output of process modeling for DIW

2.3.1.2 Output of process modeling for DIW

Firstly, Freeform extruded filaments (FEF) are extruded filaments in the air between the nozzle bottom and the substrate in DIW (Figure 2.9 (a)). During the DIW, producing continuous, tubular FEF with diameters close to the actual nozzle inner diameter is a prerequisite and also a characterization for a high printing quality [82]. For instance, Ouyang et al. [97] characterized ink printability through shape statuses of FEF as three status: "under-gelation", "proper-gelation" and "over-gelation"; Paxton et al. [98] focused on the formation properties of FEF as an initial screening to assess ink printability; Smith et al. [82] proposed a term considering the measured diameter of the FEF and nozzle inner diameter to define printability; Dávila et al. [99] evaluated ink printability through observation of FEF formation; He et al. [100] chose suitable ranges for process parameters setting in DIW 3D printers by observing shapes of FEF. Therefore, FEF is one of the most basic output of process modeling for DIW and mean diameter and stability are two indicators to evaluate the FEF.

Secondly, FEF is deposited on the substrate forming as deposited filament (DF) (Figure 2.9 (b)). The quality of the DIW 3D printed parts depends on the deposition status and profile dimension of DF [101]. Kazemian et al. [102] proposed a real-time extrusion quality monitoring technique for cement ink based DIW by observing DF using computer vision. Tu et al. [103] divided the deposition status into "over-deposition", "pressed-deposition" and "freeform-deposition" based on the shapes of DF. Thus, DF is also one of the most basic output of process modeling for DIW and flow rate, deposition status, height and width are critical indicators for DF.

Thirdly, from DF to a layer, DF needs to change direction and deposited corners are formed (Figure 2.9 (c)). The geometrical quality of 3D parts fabricated by DIW is influenced by the deposition quality of deposited corners [104]. Several scholars have done researches on improving the geometrical quality of MEAM by controlling quality of deposited corners [105-108]. Akhoundi et al. [105] improved the quality of corners through printing speed optimization to realize high-quality printed composites with different geometric shapes for MEAM. Giberti et al. [106] presented a path planning technology to maintain a constant velocity along the trajectory in corners aimed at improving dimensional quality for MEAM. Jin et al. [107] proposed an optimized path planning technique to decrease the number of sharp corners in MEAM to improve deposition quality of printed parts. Li et al. [108] improved precision of deposited corners and parts of MEAM by in-situ monitoring and predicting 3D geometric

deviation. Thus, deposited corner is one of the most basic output of process modeling for DIW and corner angle and outline are elements of concern in process analysis for deposited corners.

Fourthly, a printed layer is deposited constructed by DF and deposited corners (Figure 2.9 (d)). Dimensional accuracy of printed layers could affect the whole part quality. At present, monitoring and control of printed layers is a research focus in AM quality control [109, 110]. He and Huang [111] predicted the in-plane shape of printed layers to improve the geometric accuracy of AM built products. He et al. [112] captured the image of each printed layer to control the whole process of FDM. Mohammad et al. [113] proposed a quality monitoring framework for 3D printing through monitoring each layer. Finally, a 3D part is printed by the layer-wise deposition (Figure 2.9 (e)). Thus, printed layer and 3D part are outputs of process modeling for DIW. For printed layers, the indicators include dimensional accuracy and roughness. For 3D parts, the indicators include dimensional accuracy, roughness, mechanical properties and functional properties.

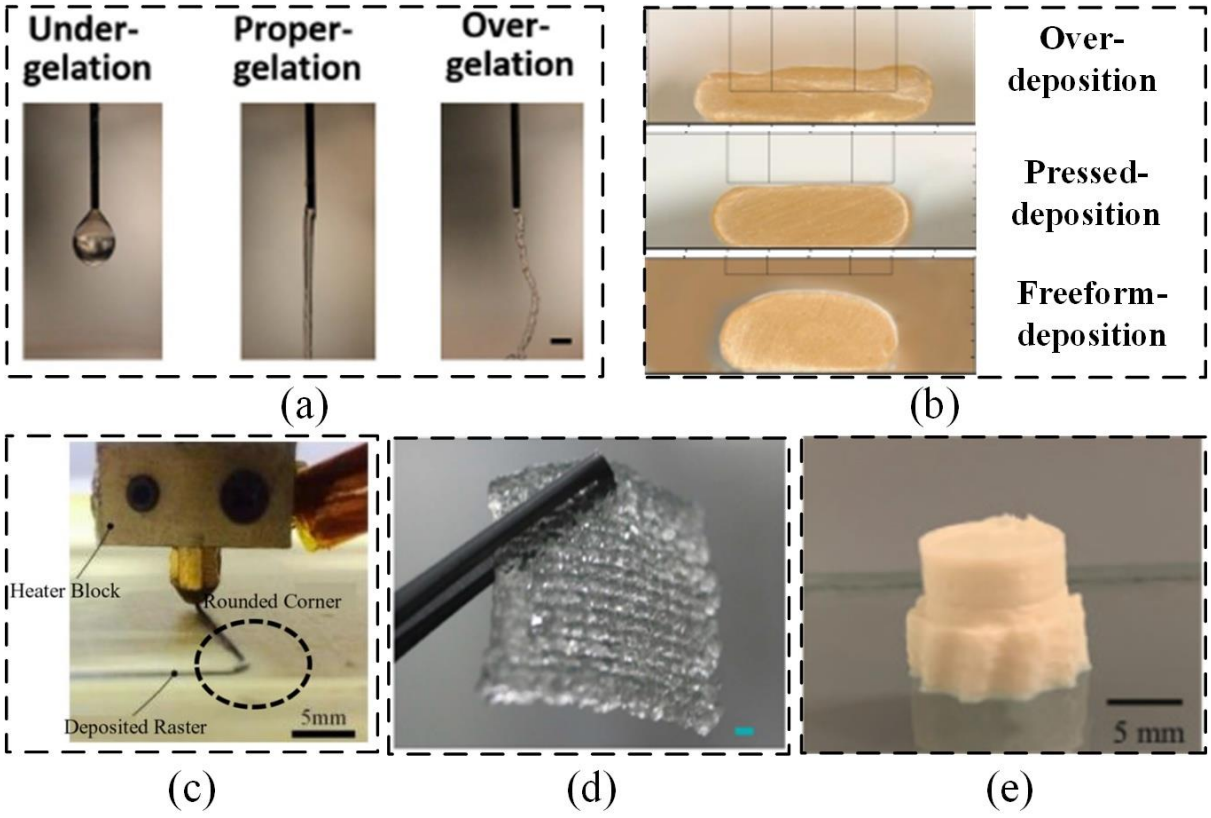

Figure 2.9 Physical photos of outputs of process modeling for DIW: (a) FEF, (b) DF, (c) deposited corner, (d) printed layer, (e) 3D part

2.3.2 Process modeling methods

Process modeling methods for MEAM include: analytical modeling methods [114], experimental data based modeling methods [115] and numerical simulation methods [116]. Each method is reviewed as follows.

2.3.2.1 Analytical modeling methods

Analytical modeling methods give a process model based on the mathematical description and derivation of physical process. Owing to the quickness and simplicity of the analytical modeling methods in the modeling of the flow rate of DF in DIW, many scholars have established models of the flow rate for the pneumatic force-driven DIW through the analytical modeling methods [117-120]. However, few works gave the complete mathematical description for flow rate of piston driven DIW. Meanwhile, analytical modeling methods are currently applied to obtain flow dynamics parameters such as extrusion rate, shear stress, and real-time viscosity during DIW but it is difficult to obtain shape of DF, printed layers and 3D parts directly. Some scholars also give mathematical descriptions of shape of DF using analytical modeling method with approximation assumptions in the derivation [121, 122]. For example, Vlasea et al. [123] described an analytical model for line width of DF by simplifying the DF's cross-sectional profile as an elliptical segment. Lee et al. [121] developed a model for DIW to predict the width of DF with an equation describing the DF's area of a half-ellipse. Suntornnond et al. [122] proposed a mathematical model to predict the width of DF by assuming the DF's cross-sectional profile was circular. Haghbin et al. [124] predicted the sizes of DF using three geometric models of rectangle, oblong and ellipse for material extrusion-based 3D printing. All these studies established analytical models of the DF by first assuming that the cross-sectionals of DF were constant shapes and the shapes were simplified as circle, half-ellipse, ellipse, rectangle or oblong. However, cross-sectional shapes of DF will change under different conditions of inks and process parameters [125]. Thus, the simplification in analytical modeling of DF limited the model prediction accuracy in profile dimensions' prediction.

2.3.2.2 Experimental data based modeling methods

Experimental data based modeling methods obtain data by using design of experiments (DOE) and obtain the model of DIW based on experimental data, which can give an intuitive description of process parameters and final prediction results. The main experimental data based modeling methods for AM include: Taguchi method [126], response surface methodology (RSM) [127] and machine learning (ML) method [128].

(1) Taguchi method

The Taguchi method was proposed by Dr. Genichi Taguchi in Japan. The purpose of Taguchi method is to obtain the optimal process parameters with the least test time and cost through DOE and to determine the contribution of each process parameter by analysis of variance (ANOVA) [129]. The Taguchi method uses "signal" and "noise" to represent the expected value (mean value) and unexpected value (variance), respectively, and uses the signal-to-noise ratio (SNR) as an indicator for quality. Because the Taguchi method has the characteristics of minimizing the test cost, it has been widely used in the process parameter optimization and process modeling of MEAM. For example, Namsoo et al. [130] used the Taguchi method to optimize the process parameters of screw extrusion 3D printing process; Emily et al. [131] used the Taguchi method to analyze the influence of parameters including printing temperature, post-processing temperature and post-processing time on the strength of parts obtained by extrusion based 3D printing and to select the optimal process parameters setting; Ala'aldin et al. [132] used the Taguchi method to analyze the impact of various parameters including filling ratio, filling pattern, layer thickness and extrusion temperature on the mechanical strength and dimensional accuracy of products in extrusion based 3D printing.

(2) Response surface methodology (RSM)

The purpose of RSM is to obtain an intuitive graphical optimization area through DOE and data analysis. Firstly, experimental data are obtained through DOE. Then, functional relationship between process parameters and target responses is obtained using data fitting. Finally, the functional relationship is used to guide the multi-optimization problem to find the optimal process parameters [133]. At present, RSM is widely used in the field of process parameters optimization for manufacturing [134, 135].

(3) Machine learning (ML) method

The ML method is an advanced method based on artificial intelligence that can perform pattern recognition from complex data sets [136] with the advantage of not requiring complex process analysis. According to the learning method, ML methods can be divided into supervised learning, unsupervised learning and reinforcement learning.

Supervised learning

Supervised learning uses a computer program to learn from a set of labeled data in a training set to identify unlabeled data from a test set with the highest accuracy. The purpose of supervised learning is to obtain the relationship between data from the data set through computer programs, so as to predict the corresponding labels for new feature data without

labels [137]. Commonly used supervised learning algorithms include linear regression algorithm, polynomial regression, decision tree, random forest, support vector machine, artificial neural network, convolutional neural network, and recurrent neural network [138].

Unsupervised learning

Unsupervised learning infers from unlabeled data [139], which is a data-driven ML method that can discover patterns or groupings hidden by similar data (i.e., clusters) in a given random dataset. Unsupervised learning is widely used in anomaly detection [140], recommender systems [141] and market classification [142]. Commonly used unsupervised learning algorithms include K-means algorithm and K-medoids algorithm.

Reinforcement learning

Reinforcement learning is a semi-supervised form of ML that allows the model to interact with the environment and learn to take the best actions that will yield the greatest reward. It does not require a training dataset and the model learns from its own actions. Reinforcement learning is currently widely used in robotic arms [143], self-driving cars [144] and AlphaGo [145]. Commonly used reinforcement learning algorithms include Q-learning algorithm, deep Q-learning algorithm, deterministic policy gradient algorithm, and deep deterministic policy gradient algorithm.

However, the disadvantage of the ML method is that it requires a large amount of data sets, additional material/time consumption and computing resources.

(4) Limitations of experimental data-based modeling methods

In summary, experimental data-based modeling methods including Taguchi method, RSM and ML methods have been widely used in manufacturing process modeling. However, these methods are limited by the experimental equipment. Some parameters are not easy to measure in DIW directly such as the speed of extruded filaments. At the same time, the model constructed by this method usually does not contain time parameter which results that it cannot be used for prediction in real time. Finally, the method requires extensive experimentation, time, material and cost.

2.3.2.3 Numerical simulation methods

As an important supplement to analytical modeling methods and experimental data based modeling methods, numerical simulation methods can provide a large amount of information on the AM process and has been widely used in the process modeling and analysis of MEAM. For example, Liravi et al. [146] used finite element analysis (FEA) to establish a model of high-viscosity material flow during extrusion 3D printing; Göhl et al. [147] used computational fluid

dynamics (CFD) software IPS IBOFlow to predict ink printability in DIW; Balani et al. [148] used numerical simulation to determine the velocity profile, shear force and real-time viscosity of PLA material in FDM; Liu et al. [149] used numerical simulation to evaluate the dynamic process of FDM; Comminalet al. used numerical simulation methods to conduct extensive modeling studies on MEAM, including simulation modeling of extrusion of high-viscosity materials [150], CFD simulation modeling of extrusion filament deposited on the substrate [151], simulation modeling of extrusion filament corners [152] and simulation modeling of polymer material flow in the nozzle [153].

The most commonly used numerical simulation methods are: volume of fluid (VOF) method [154], level set method [155], phase field method [156], lattice Boltzmann method [157] and direct interface tracking method [158]. The idea of VOF method is to introduce the volume fraction and treat the two-phase flow as a single flow model with variable material properties including density and viscosity. And then VOF uses the volume fraction to determine the position of the liquid free surface. The idea of the level set method is to regard the tracked moving interface as the zero isosurface of the level set function and extend the velocity of the interface to the level set function, and obtain the position of the fluid interface by solving the level set function. The idea of the phase field method is to use a very thin finite thickness to represent the phase interface and the state parameters on the interface are continuously distributed and have a high gradient. The idea of the lattice Boltzmann method is to simulate fluid flow at the mesoscopic scale by solving the discrete Boltzmann equation. The direct interface tracking method defines the marker variables of the two-phase flow interface position and uses a fixed grid in the entire flow field; finally, the position and shape of the two-phase flow interface at each moment is tracked by solving the governing equations on the fixed grid. Among these methods, VOF method is currently the most commonly used method for process modeling of MEAM process due to its simplicity, robustness, and accuracy [159, 160].

Numerical simulation is one of the most powerful tools in process modeling analysis in AM. Process analysis based on numerical simulations has advantages in saving material/trial time and easily capturing critical process parameters value which are difficult obtained by experimental measurements. Although a large number of studies have used numerical simulation modeling methods to establish process models of MEAM, there is currently few systematic works on process modeling and analysis based on numerical simulations for DIW. Thus, to improve the manufacturing accuracy and application promotion of DIW, it is

meaningful and critical to do research on process modeling and analysis based on numerical simulations for DIW.

2.3.3 Conclusion

The purpose of process modeling for DIW is to construct the relationship between inputs and outputs in the printing process, which is used to predict the outputs according to the inputs before printing. The inputs are summarized as the material properties of the ink (density, surface tension and viscosity) and the printing process parameters setting (nozzle inner diameter, piston diameter, piston speed, nozzle piston, layer height). The outputs include the FEF, DF, deposited corner, printed layer and 3D part. Numerical simulation is one of the most powerful tools in process analysis in AM. Process analysis based on numerical simulations has advantages in saving material/trial time and easily capturing critical process parameters value which are difficult obtained by experimental measurements. The research on process modeling and analysis of DIW based on numerical simulations will provide important support for the development and guidance of DIW. However, the literature review shows that there is currently few systematic works on process modeling and analysis based on numerical simulations for DIW. To bridge this gap, the objective of this thesis is to do research on process modeling and analysis for DIW based on numerical simulations. The next two chapters describe in detail the proposed numerical approach and its results.

Chapter 3: Ink material properties characterization and process parameters selection

3.1 Introduction

The printing quality of DIW process depends on ink material properties and process parameters setting. Recent studies [93-95] focused on inks preparation and ink material properties characterization as ink material properties play the most critical role in extrusion process, shrinkage, shape fidelity and structural stability. DIW process parameters concerned with the equipment considerably affect the parts' dimensional accuracy [96]. Meanwhile, ink material properties and process parameters are inputs of process modelling of DIW. Thus, this chapter presents our research work on ink material properties characterization and process parameters selection to provide the basis for modeling inputs of DIW.

For ink material properties characterization, density, surface tension, static contact angle and rheology properties are obtained for the used ink through experimental methods.

For process parameters selection. Recently, the selection of process parameters for DIW has been conducted by many scholars [98, 161, 162]. However, all these studies just determined a printability window instead of an optimal value and few studies are available for process parameters significance analysis and optimization for DIW. Therefore, it is imperative to investigate the significance of each process parameter and find optimal process parameters setting to improve dimensional accuracy of parts in DIW.

Taguchi method [126] and machine learning (ML) methods [108, 163] have been widely used to control process parameters of material extrusion-based 3D printing. ML methods enable the proper parameters selection with little process analyses but need large dataset, additional time and computing resources [136]. Taguchi technique is more efficient [164] with a significant slash in experimental time and cost [129] and it can determine the significance of each parameter by analysis of variance (ANOVA) [165]. To perform DIW process parameters optimization with minimum material and time, Taguchi method is adopted in this chapter.

This chapter starts with the presentation of ink material properties characterized for the used ink in this thesis. Then, process parameters are selected for the used ink in the DIW 3D printer. Especially, in process parameters selection, we identify DIW process parameters

through printing analyses and propose a two-step optimization method to optimize DIW process parameters for dimensional accuracy of printed layers and analyze the significance of each process parameter. To verify the method, confirmation tests are conducted considering the condition comparison and the method robustness on other shapes as well as parameter adaptability in 3D parts printing from printed layers' analyses for the proposed method and parameter adaptability in constructs fabricated as 100% infill or with porosities.

3.2 Ink properties characterization

3.2.1 Ink used in this thesis

The objective of this thesis is to develop an approach on process modeling and analysis for DIW based on numerical simulations. Ink preparation is not research content in this thesis. Thus, a well-printable ink is selected and used directly in this thesis.

Nivea Crème (Art. No. 80104) (Beiersdorf Global AG, Germany) is chosen as the ink reference material to verify the proposed numerical simulations because Nivea Crème is used as printability reference for inks to test the process parameters in DIW and can represent numerous printable inks in DIW [98]. Nivea Crème meets the requirements of DIW inks material properties (shear thinning ability during extrusion and shape retention after deposition) and many inks in DIW are designed and produced to have the same printability of Nivea Crème.

The main ingredients of the Nivea Crème include water, mineral oil, petrolatum, glycerin, microcrystalline wax, lanolin alcohol, paraffin, panthenol, magnesium sulfate, decyl oleate, octyldodecanol, aluminum searates, fragrance, citric acid, magnesium stearate, methylchloroisothiazolinone, methylisothiazolinone. Among these ingredients, water is solvent; glycerin is humectant; lanolin alcohol is emulsion stabilizer; microcrystalline wax is thickening agent and binder. And microcrystalline wax has the greatest effect on the rheological properties and printability of the Nivea Crème ink.

3.2.2 Ink material properties characterization tests

3.2.2.1 Density, surface tension, static contact angle

A 5 mL pycnometer and analytical balance XSR (both from Mettler Toledo, France) are used to assess ink density by measuring a mass of 5 mL of the ink (measuring accuracy: 0.008 mg).

A tensiometer K9 (KRÜSS, Germany) is used to measure the surface tension coefficient using the Du Noüy ring method (measuring accuracy: 0.1 mN/m).

Static contact angle is measurement by observing the cross-sectional profile of DF in DIW without stretch or squeeze using the method proposed in the paper [125]. In this method, a section of DF is printed in the steady-state coiling regime to ensure the DF is not stretched by the translational motion of the nozzle or not squeezed by over deposition of DF.

All measurements of density, surface tension and static contact angle are performed at 25 ℃ and repeated three times.

3.2.2.2 Rheology characterization

A complete rheological characterization for Nivea Crème is conducted as ink rheology plays the most critical role in DIW. A rheometer ARES (TA Instruments, USA) with a 25 mm plate-plate geometry at a gap distance of 1 mm is used in ink rheology characterization. Especially, shear stress ramp test, shear rate sweep test, frequency sweep test and recovery test are conducted to determine yield stress, viscosity, modulus (including storage modulus (G') and loss modulus (G'')) and recovery characteristic, respectively. Shear stress ramp test and shear rate sweep test are used to characterize the shear-thinning rheology property of the ink. Frequency sweep test and recovery test are used to characterize the shape retention rheology property of the ink.

In shear stress ramp test, shear stress is changed from 2 Pa to 900 Pa and the shear stress are set to 10 points evenly distributed within 100 Pa. In shear rate sweep test, shear rate is changed from 0.0125 to 100 s^{-1} and the shear rates are set to 5 points per decade. In frequency sweep test, angular frequency is changed from 100 rad/s to 1 rad/s in 1rad/s interval. In recovery test, from 0-200 s, the shear rate value is set as 0.0125 s^{-1}; from 200-300 s, the shear rate value is set as 895 s^{-1}; from 300-500 s, the shear rate value is set as 0.0125 s^{-1}. All measurements are performed at 25 ℃ and repeated three times.

The Hershel-Bulkley model (HBM) has been verified and adopted as a suitable and reliable model to represent the viscosity of the inks in DIW with shear-thinning and shape retention rheology property [161, 166]. Using the HBM, the shear stress and the viscosity of inks can be expressed by Eq. (3.1) and Eq. (3.2), respectively.

$$\tau = \tau_0 + K\dot{\gamma}^n \tag{3.1}$$

$$\mu = \min\left(\mu_0, \tau_0/\dot{\gamma} + K\dot{\gamma}^{n-1}\right) \tag{3.2}$$

Where τ (unit: Pa), $\dot{\gamma}$ (unit: s^{-1}), μ (unit: $Pa \cdot s$) are variables named as shear stress, shear rate, dynamic viscosity for inks in flow; μ_0 (unit: $Pa \cdot s$), τ_0 (unit: Pa), K (unit: $Pa \cdot s^n$), n (unit: dimensionless) are rheological properties called as limiting dynamic viscosity, yield

stress, consistency index, flow index for inks. If stress< τ_0, the ink behaves as a rigid solid, otherwise it behaves as a fluid. For n <1, the ink is shear-thinning, whereas the ink is shear-thickening. A large μ_0 means that the ink will only flow in response to a large applied force.

μ_0 and τ_0 are determined using experimental viscosity-shear stress curve obtained by shear stress ramp test: abscissa and ordinate of intersection point between two linear regressions at the plateau-region and viscosity-drop regions of the viscosity-shear stress diagrams are μ_0 and τ_0, respectively. K and n are determined through regression between Eq. (3.2) and experimental viscosity-shear rate data obtained by shear rate sweep test.

3.2.3 Ink material properties characterization results

3.2.3.1 Results of density, surface tension, static contact angle

The density and surface tension coefficient of the Nivea Crème are obtained by density and surface tension tests and the results are: density ρ is 972 kg/m^3 and surface tension coefficient σ is 43 mN/m.

For static contact angle, as shown in Figure 3.1 (a), a section of filament is printed in the steady-state coiling regime which ensured the filament is not stretched by the translational motion of the nozzle. As shown in Figure 3.1 (b), static contact angle θ_C is measured directly through photo of cross-sectional profile of the filament and the value of θ_C is 180 °.

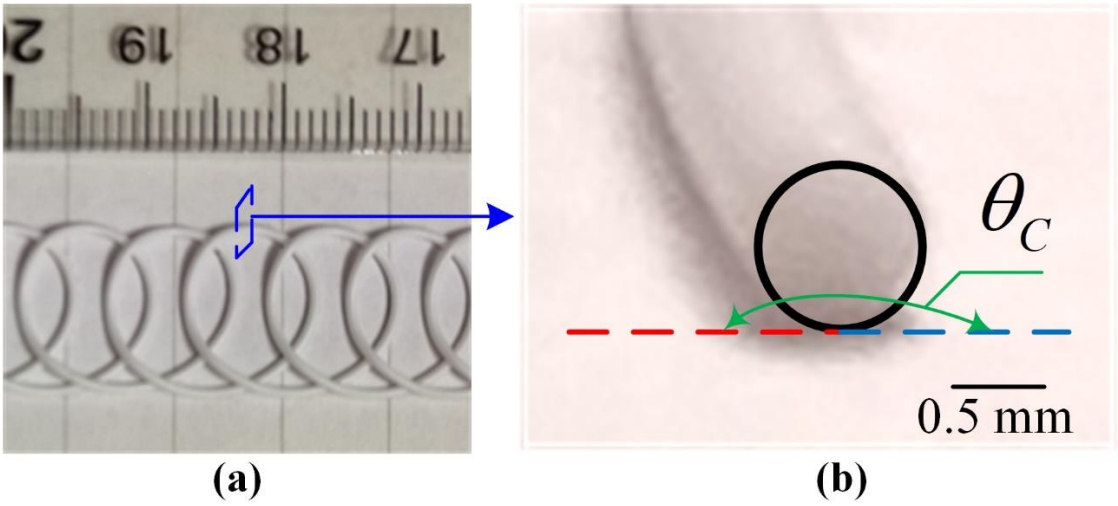

Figure 3.1 Experimental results of static contact angle of the Nivea Crème: (a) top view of filament printed in the steady-state coiling regime, (b) cross-sectional profile of the filament

3.2.3.2 Results of rheology characterization

Results of rheology characterization are plotted in Figure 3.2. The result shear stress ramp test (Figure 3.2 (a)) shows that the ink stays rest when the shear stress value is below yield

stress and starts to flow when the shear stress value exceeds yield stress. Figure 3.2 (b) shows the shear-thinning characterization of the ink as viscosity decreases with the increase of shear rate. The ink exhibits a solid-like response as its storage modulus (G') exceeds its loss modulus (G'') (Figure 3.2 (c)), which means the ink has low shrinkage and good shape fidelity. Moreover, the structural stability of the ink is also good as shown in Figure 3.2 (d): from 0-200 s, the viscosity stays stable and in high value when shear rate value is near 0; from 200-300 s, the viscosity stays stable and in low value when shear rate value is 895 s^{-1}; from 300-500 s, the shear rate value recoveries to near 0 and the viscosity recoveries to stay stable and in high value. In conclusion, Nivea Crème is verified as a well-printable ink through the rheological characterization.

Then, parameters in HBM viscosity model are obtained through data analyses of Figure 3.2 (a) and Figure 3.2 (b). As shown in Figure 3.2 (a), μ_0 and τ_0 are determined using the intersection point of two tangents in the diagram of shear stress ramp test data where one is stable platform line (red dotted line) in the plateau-region and the other one is the quickly-drop line (purple dotted line) in the viscosity-drop region. Abscissa and ordinate of the intersection point are μ_0 and τ_0, respectively. The results are: $\mu_0 = 1.58 \times 10^6$ $Pa \cdot s$; $\tau_0 = 563$ Pa.

As shown in Figure 3.2 (b), shear thinning parameters, K and n, are obtained by fitting Eq. (3.2) with the viscosity-shear rate data using data regression. The results are: $K = 867$ $Pa \cdot s^n$; $n = 0.045$. The coefficient of determination (R^2) and p-value of fitting results are 0.9947 and 0.0000<0.05, verified the fitting results is correct.

In conclusion, results of ink material properties are all obtained and listed in Table 3.1.

Table 3.1 Ink material properties of the selected ink Nivea Crème

Parameter	Density ρ (kg/m^3)	Surface tension coefficient σ (mN/m)	Static contact angle θc (°)	Limiting dynamic viscosity μ_0 (Pa.s)	Yield stress τ_0 (Pa)	Consistency index K (Pa.s^n)	Flow index n
Value	972	43	180	1.58×10^6	563	867	0.045

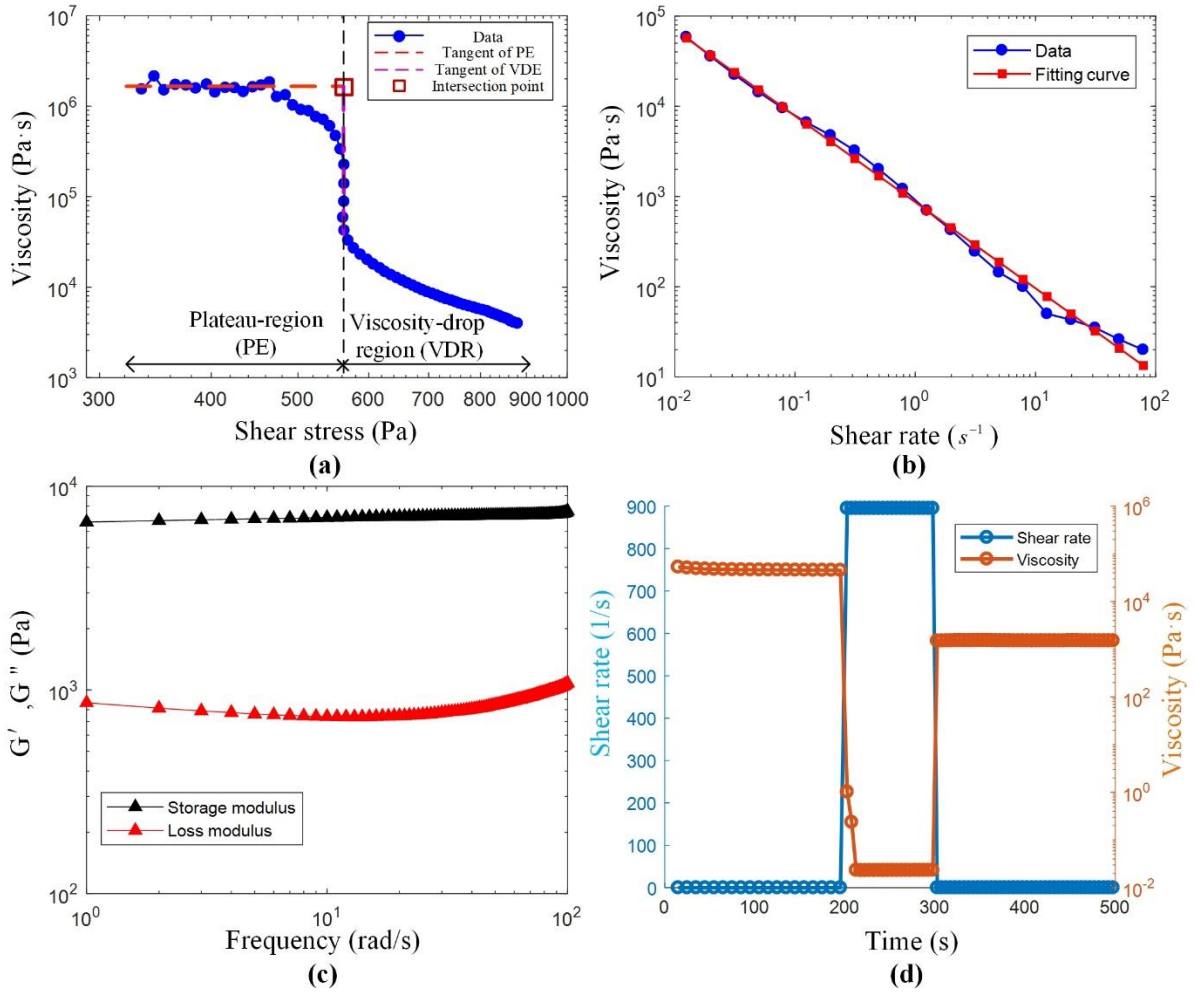

Figure 3.2 Rheological characterization of Nivea Crème (Art. No. 80104): (a) limiting dynamic viscosity and yield stress determination through shear stress ramp test; (b) viscosity as a function of shear rate; (c) storage (G') and loss (G'') modulus as a function of frequency; (d) stability analysis through recovery test

3.3 Process parameters selection

3.3.1 DIW 3D printer used in this thesis

A piston driven DIW 3D printer TM-081 (Tobeca Company, France) is used in this thesis as illustrated in Figure 3.3 (a). The piston movement is driven by a mechanical system, which extrudes out ink in the syringe through the nozzle into the air and finally on the substrate. Then, a three-axis movement frame guides the nozzle to move in x and y directions to deposit the extruded filaments on a planar region as nozzle is fixed in z direction. Afterward, the nozzle moves to the next layer and 3D parts are printed layer by layer.

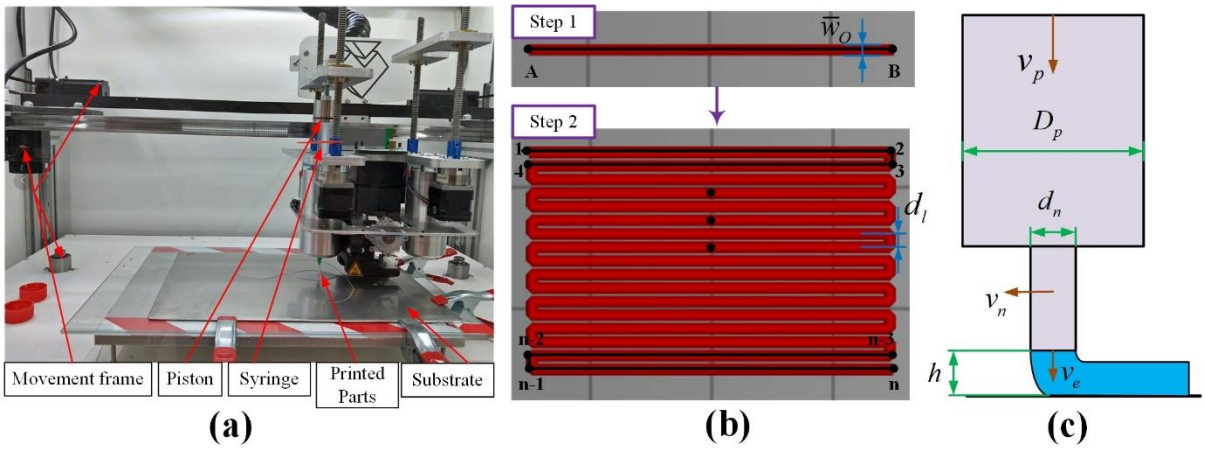

Figure 3.3 Process parameters identification for DIW process: (a) the DIW 3D printer used in this thesis; (b) the DIW process; (c) process parameters setting in Step 1

3.3.2 Identification of process parameters

Process parameters are identified through DIW process analysis. As shown in Figure 3.3 (b), DIW process for a printed layer includes two steps. Step 1 is to print a line by moving nozzle from point A to point B. Then, a layer is printed by arranging lines tightly in Step 2. Thus, DIW process parameters for printed layers are divided into two categories as:

1) Process parameters for printing a line;

2) Extra process parameter from lines to a layer.

3.3.2.1 Process parameters for printing a line

The process parameters for printing a line is illustrated in Figure 3.3 (c). Piston diameter D_p and inner diameter of nozzle d_n are dependent on equipment and considered as constants. Their values are 21.6 mm and 0.84 mm, respectively. v_p (piston velocity), v_n (nozzle velocity) and h (gap between nozzle bottom surface and substrate) are identified as controllable process parameters. v_e (average velocity of extruded filament on the nozzle bottom surface), which is dependent on v_p and equipment, is uncontrolled process parameters.

In extrusion-based AM, optimal v_n depends on v_p [152] and optimal h depends on d_n [150]. If v_p, v_n and h are set independently without regard to the relationship between these parameters, the optimization would be inefficient and even incorrect. Thus, process parameters for printing a line are identified as: v_n, V^* (dimensionless nozzle velocity, defined as v_n / v_e) and H^* (dimensionless height, defined as h / D_p). Because the ink extrusion and deposition process are considered as an isothermal, incompressible and laminar flow, the average velocity

on each cross section in the nozzle is the same and v_e can be expressed as follows using conservation of mass.

$$v_e = \left(D_p / d_n\right)^2 v_p \tag{3.3}$$

3.3.2.2 Extra process parameter from lines to a layer

As illustrated in Figure 3.3 (b), $\bar{w}_O$ (average width of the optimal printed line) of printed line under optimal condition is measured in Step 1. Then, a rectangular object (reprehensive of the printed layers) is printed by controlling d_l (distance between lines) line by line. In extrusion-based AM, optimal d_l depends on $\bar{w}_O$ [151]. Thus, extra process parameter from lines to a layer is identified as R_W (ratio of d_l to $\bar{w}_O$) and d_l could be determined as follows:

$$d_l = R_W \cdot \bar{w}_O . \tag{3.4}$$

R_W mainly reflects the impact of W (the weight of the printed layer) on distortion in x-y plane (detailed relationship between R_W and W as well as its derivation process are shown in the Appendix A of Appendices).

Consequently, DIW process parameters are identified as:

1) Process parameters for printing a line: v_n, V^* and H^*;

2) Extra process parameter from lines to a layer: R_W.

3.3.3 Definition and measurement method of dimensional errors

Dimensional errors are divided into dimensional error for printed lines and dimensional error for printed layers according to the two categories of identified process parameters. x-y plane dimensional accuracy is of primary interest and dimensional accuracy in the z axis can be ignored for layer accuracy analyses because previous studies [109, 111, 113] have verified that the use of control charts with image data only considering x-y plane dimensions for each layer could improve quality of parts in 3D printing significantly.

3.3.3.1 Dimensional error for printed lines and its measurement method

(1) Definition of dimensional error for printed lines

As illustrated in Figure 3.4 (a), N_1 measuring points are set along the line length uniformly and widths of line on each measuring point are measured as $w_i (i = 1, 2, ..., N_1)$. Average width of the printed line is calculated as follows:

$$\bar{w} = \sum_{i=1}^{N_1} w_i / N_1 . \tag{3.5}$$

Because the designed dimension of line is not specified and the most concerned quality of the printed lines is stability, which means the line width need to be always same along the deposition direction, the referenced dimension of line is defined as the average width $\bar{w}$ and the dimensional errors $el_i (i = 1, 2, ..., N_1)$ on each measuring point along length are defined as follows:

$$el_i = w_i - \bar{w}, (i = 1, 2, ..., N_1) \tag{3.6}$$

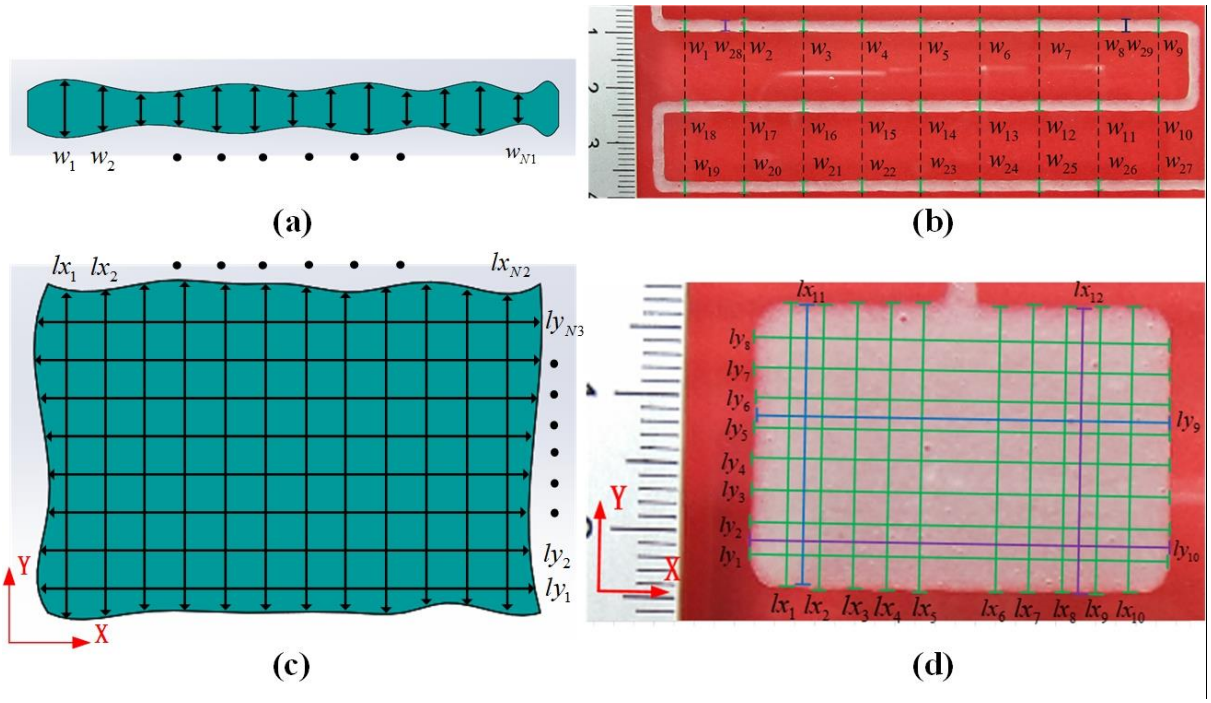

Figure 3.4 Definition and measurement method of dimensional errors: (a) definition of dimensional errors for printed lines; (b) measuring points setting for printed lines; (c) definition of dimensional errors for printed rectangular objects; (d) measuring points setting for printed rectangular objects

(2) Measurement method of dimensional error for printed lines

As shown in Figure 3.4 (b), to reduce measurement error and consider the printing stability in the whole range, three lines are printed (each line is 100 mm long) and 9 measuring points are set for each line uniformly. 27 measuring points are uniformly distributed along lines as w_1 to w_{27}. Minimum and maximum widths of lines except 27 measuring points are measured as w_{28} and w_{29}. Thus, totally 29 dimensional errors are used for dimensional accuracy analysis of printed lines. In practice, a ruler is put beside printed lines as reference dimension and photo of printed lines with ruler is taken using a camera (Canon LEGRIA HF R86 Noir, Canon Inc., Japan). Then, photo is imported into MATLAB and widths are measured using virtual ruler of the graphic processing tools in MATLAB.

3.3.3.2 Dimensional error for printed rectangular objects and its measurement method

(1) Definition of dimensional error for printed rectangular objects

As illustrated in Figure 3.4 (c), N_2 and N_3 measuring points are set along x and y directions in the printed rectangular object uniformly and lengths on each measuring point along x and y direction are measured as $lx_i (i = 1, 2, ..., N_2)$ and $ly_i (i = 1, 2, ..., N_3)$. Average lengths for x and y directions are calculated as follows:

$$\overline{lx} = \sum_{i=1}^{N_2} lx_i / N_2 \tag{3.7}$$

$$\overline{ly} = \sum_{i=1}^{N_3} ly_i / N_3 \tag{3.8}$$

Designed dimensions for rectangular object in x and y directions are Lx and Ly. Dimensional errors for the printed rectangular object in x and y directions are defined as follows:

$$erx_i = lx_i - Lx, (i = 1, 2, ..., N_2) \tag{3.9}$$

$$ery_i = ly_i - Ly, (i = 1, 2, ..., N_3) \tag{3.10}$$

(2) Measurement method of dimensional error for printed rectangular objects

To reduce measurement error and consider the printing stability in the whole range, measuring points setting for printed rectangular objects are shown in Figure 3.4 (d). Designed dimensions for rectangular object in x and y directions are Lx =30 mm and Ly =20 mm, respectively. In x direction, 10 measuring points are set uniformly as lx_1 to lx_{10}. Minimum and maximum lengths except 10 points are measured as lx_{11} and lx_{12}. In y direction, 8 measuring points are set uniformly as ly_1 to ly_8, and minimum and maximum lengths except 8 points are measured as ly_9 and ly_{10}. Thus, 12 lengths are measured in x direction as lx_1 to lx_{12}; and 10 lengths are measured in y direction as ly_1 to ly_{10}. Totally, 22 dimensional errors are used for dimensional accuracy analysis of printed rectangular objects. In practice, the lengths measurement method is same as widths measurement for printed lines using ruler beside the printed object and MATLAB.

3.3.4 Framework for DIW process optimization and orthogonal array selection procedure

3.3.4.1 Framework for DIW process optimization

The framework of DIW process optimization contains two steps and the two-step process parameters optimization method is shown in Figure 3.5. Step 1 is to optimize process parameters for printing a line. In step 1, continuity and uniformity of FEF and DF and printed rectangular objects on the substrate are observed in screening experiments to determine printability windows for each process parameter. Then, interaction effect tests are conducted and design of freedom (DOF) for experiments is calculated followed by orthogonal array (OA) selection for Taguchi design. Next, main experiments of line printing based on Taguchi method are conducted. SNR calculations and ANOVA are performed for Taguchi method based data to find the optimal combination and evaluate the significance respectively. Step 2 is to optimize extra process parameter from lines to a layer. In Step 2, the average width of printed lines under optimal condition is obtained firstly. Then, single-factor tests of rectangular object printing are conducted to find the optimal R_W. Finally, the optimal combination of total identified process parameters is summarized through step 1 and step 2 of the framework.

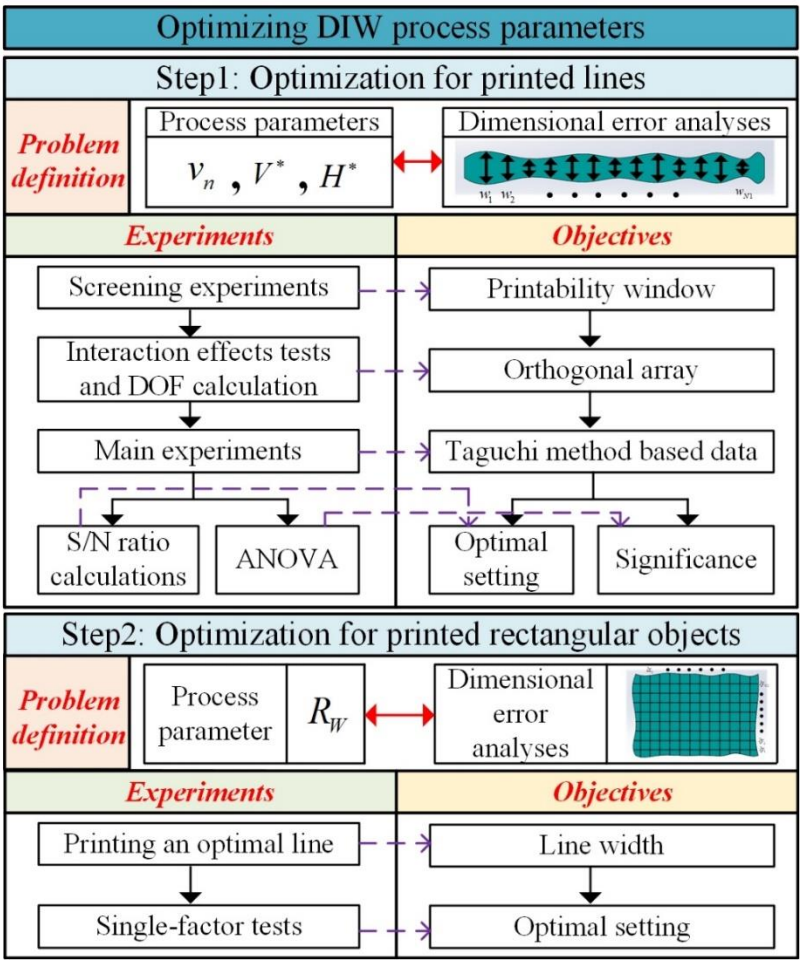

Figure 3.5 Framework of the proposed two-step method for optimizing DIW process parameters for printed layers

3.3.4.2 Orthogonal array (OA) selection procedure

Instead of conducting full factorial experiments, Taguchi method based experiments of different process conditions are conducted through an OA, minimizing the number of experiments while ensuring the validity and robustness of the data [167]. The OA is selected based on DOF calculation considering the number of factors, interactions between them and the number of levels of each factor [168]. The procedure for OA selection is as follows:

(1) Determine the number, levels and interaction effects of factors.

(2) Calculate the total DOF of factors. DOF for a single factor is equal to one less than the number of levels of that factor. DOF for a two-factor interaction effect is equal to $(S_1-1)\times(S_2-1)$ as S_1 and S_2 are DOF of the two factors. Total DOF of factors is cumulative sum of DOF of all single factors and DOF of all two-factor interaction effects.

(3) OA is selected from commonly used standard OAs based on total DOF of factors as number of experiments should require Eq. (3.11) as follows [169]:

$$T \geq DOF_{total} + 1 \tag{3.11}$$

Where T is number of experiments; DOF_{total} is total DOF of factors and their interaction effects.

3.4 Process parameters selection results

3.4.1 Optimization of printed line

3.4.1.1 Printability windows

The term 'printability window' is defined as the combination of process parameters required for successful extrusion for DIW [98]. In experiments, printability window determination criterions include three points: continuity and uniformity of 1) FEF; 2) DF and 3) printed rectangular object on the substrate.

In screening experiments of FEF, v_p is calculated using Eq. (3.3) by fixing V^* as 1 and changing v_n from 1 mm/s to 20 mm/s (interval is 2 mm/s). In screening experiments of DF, v_n is fixed in printability window; then V^* is changing from 0.2 to 1.2 (interval is 0.2) and H^* is changing from 0.2 to 1.2 (interval is 0.1), respectively. In screening experiments of printed rectangular objects on the substrate, v_n, V^* and H^* are fixed in printability window; and R_W is changing from 0.2 to 1 (interval is 0.1).

Through screening experiments, printability windows of each process parameter for the prepared ink are listed as: (5~11) mm/s for v_n; (0.6~1) for V^*; (0.6~1.2) for H^* and (0.5~0.9) for R_W.

3.4.1.2 Orthogonal array (OA) selection

The lower value, middle value and higher value of printability windows for each factor in step 1 (v_n, V^* and H^*) are considered to be level 1, 2 and 3 respectively as listed in Table 3.2.

Table 3.2 Levels of process parameters in step 1

Parameter	Range	Level 1	Level 2	Level 3
v_n	(5~11) mm/s	5	8	11
V^*	0.6~1	0.6	0.8	1
H^*	0.6~1.2	0.6	0.9	1.2

In this step, two-factor interaction effects are considered. In interaction effect tests, one factor of v_n, V^* and H^* is fixed and the remaining two factors are changed to print lines for

interaction effect analysis of the remaining two factors. Average widths of printed lines under each process parameters setting are calculated as indicator to analyze interaction effects. Interaction effect graphs are plotted in Figure 3.6 (a) (detailed information of interaction effect tests is summarized in the Appendix B of Appendices).

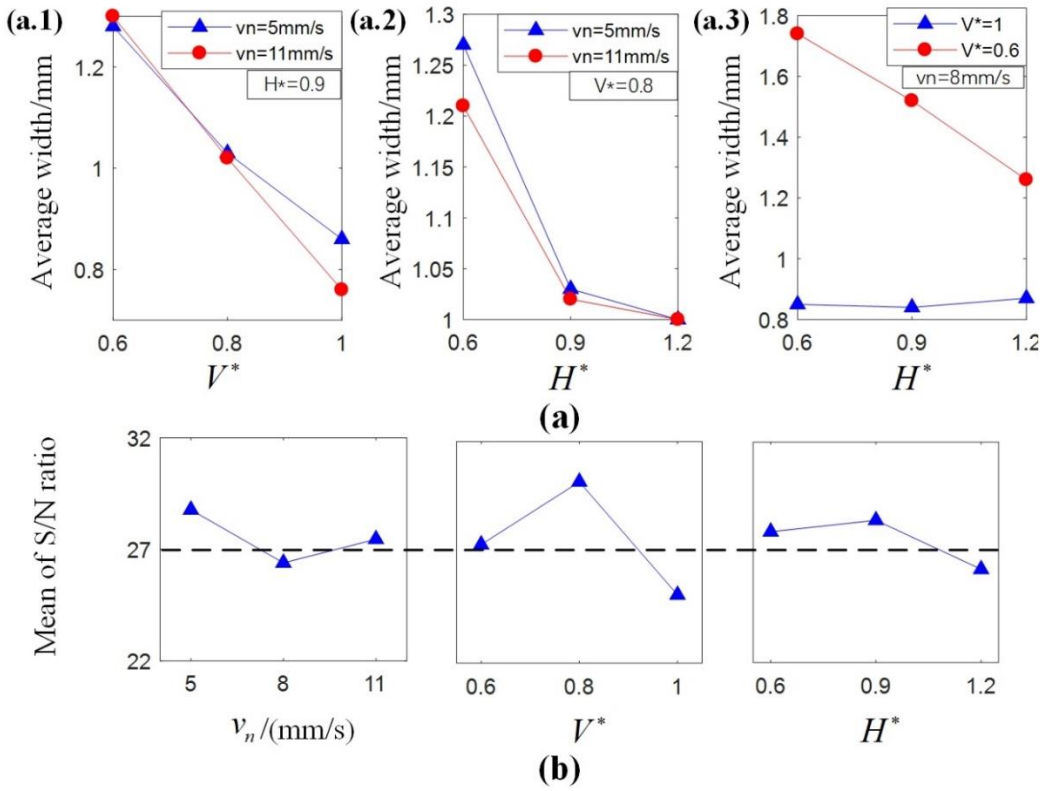

Figure 3.6 (a) Interaction effect graphs of step1 for: (a.1) $v_n \times V^*$; (a.2) $v_n \times H^*$; (a.3) $V^* \times H^*$ and (b) mean SNR graph for main experiments in step 1

Interaction effect graph is a tool to study whether influence of one factor affects the function of the other factors [170]. In the graph, parallel line shows no interaction effect and the intersect or intersect trend between lines means a high degree of interaction [171]. As illustrated in Figure 3.6 (a), interaction effects of $v_n \times V^*$, $v_n \times H^*$ and $V^* \times H^*$ should be considered as two lines in graphs intersect for $v_n \times V^*$ as well as $v_n \times H^*$ and had intersect trend for $V^* \times H^*$. Thus, three factors (v_n, V^* and H^*) and three interaction effects ($v_n \times V^*$, $v_n \times H^*$ and $V^* \times H^*$) are considered in calculation for total DOF of factors.

DOF of single factor and their interaction effects are calculated according to Section 3.3.4.2 and the calculation result of total DOF of factors is 21. Thus, according to Eq. (3.11), L_{27} OA (L_T means OA with T experiments) is selected for main experiments of step 1 as shown in Table 3.3, from commonly used standard OAs for three-level Taguchi design including L_9, L_{18} and L_{27}.

Table 3.3 Experimental plan and calculated SNR for main experiments of step 1

Experiment number	Experimental condition			SNR of dimensional errors
	v_n /(mm/s)	V^*	H^*	
N1	5	1	0.6	22.51
N2	5	1	0.9	27.14
N3	5	1	1.2	22.73
N4	5	0.8	0.6	24.36
N5	5	0.8	0.9	36.83
N6	5	0.8	1.2	33.42
N7	5	0.6	0.6	29.24
N8	5	0.6	0.9	30.33
N9	5	0.6	1.2	32.41
N10	8	1	0.6	23.80
N11	8	1	0.9	22.40
N12	8	1	1.2	22.07
N13	8	0.8	0.6	37.32
N14	8	0.8	0.9	33.76
N15	8	0.8	1.2	25.78
N16	8	0.6	0.6	23.53
N17	8	0.6	0.9	25.37
N18	8	0.6	1.2	23.45
N19	11	1	0.6	36.61
N20	11	1	0.9	24.71
N21	11	1	1.2	23.74
N22	11	0.8	0.6	27.22
N23	11	0.8	0.9	26.96
N24	11	0.8	1.2	25.94
N25	11	0.6	0.6	26.78
N26	11	0.6	0.9	28.56
N27	11	0.6	1.2	26.52

3.4.1.3 SNR analysis

Main experiments of step 1, containing 27 experimental runs, are conducted as shown in Table 3.3. Based on the requirements of response, SNR is divided into three categories namely medium-the-better, higher-the-better and lower-the-better [172]. In optimization of printed lines, the dimensional error is the lower-the-better to enhance the printing accuracy. Hence, Eq. (3.12) is used to calculate the SNR; and results are listed in Table 3.3.

$$\eta = -10\log\left(\frac{1}{N_m}\sum_{i=1}^{N_m} y_i^2\right) \tag{3.12}$$

Where η is the average SNR, N_m is the number of experiments conducted at level i and y_i is the evaluation value (dimensional error).

The mean SNR response of each process parameters in each level is calculated and listed in Table 3.4. Figure 3.6 (b) represents the mean SNR graph. Higher SNR represents the minimum variation difference between the desired output and evaluated output. Therefore, optimal process parameters for high dimensional accuracy using Taguchi method are found as: v_n=5 mm/s, V^*=0.8, H^*=0.9.

Table 3.4 Mean SNR response table for dimensional error of main experiments in step 1

Process parameters	Mean SNR for dimensional error			Max-Min	Rank
	Level 1	Level 2	Level 3		
v_n	28.77	26.38	27.45	2.39	2
V^*	27.35	30.18	25.08	5.10	1
H^*	27.93	28.45	26.23	2.22	3

3.4.1.4 ANOVA results

ANOVA is a tool to investigate the significant effect and indicate the contribution of process parameters in machinability researches [173]. ANOVA results for dimensional error of printed lines obtained using Minitab software is shown in Table 3.5. From Table 3.5, it is found that dimensional error is significantly influenced by V^* followed by $v_n \times V^*$, $v_n \times H^*$, H^*, v_n and $V^* \times H^*$. The contribution percentages of process parameters setting for V^*, H^* and v_n on dimensional error are 27.78%, 6.64% and 6.37%, respectively, meaning V^* is the most important process parameters for dimensional error of printed lines for the selected ink. Meanwhile, interaction effects of $v_n \times V^*$, $v_n \times H^*$ and $V^* \times H^*$ influenced dimensional error in

26.65%, 7.01% and 4.41% percentage of contribution respectively. Thus, OA selection for Taguchi design should consider interaction effects of $v_n \times V^*$, $v_n \times H^*$ and $V^* \times H^*$ as interaction effects of $v_n \times V^*$, $v_n \times H^*$ and $V^* \times H^*$ have big influences on dimensional error. V^* is highly significant in dimensional error at 95% level of confidence as p-value<0.05. Thus, V^* is principal in single process parameters setting which should be paid more attention in DIW for the selected ink.

Table 3.5 Mean SNR response table for dimensional error of main experiments in step 1

Source	DOF	Sum of squares (SS)	Mean squares (MS)	F-ratio	p value	Contribution (%)
v_n	2	62.90	31.45	1.21	0.349	6.37
V^*	2	274.31	137.15	5.26	0.035	27.78
H^*	2	65.58	32.79	1.26	0.335	6.64
$v_n \times V^*$	4	263.16	65.79	2.52	0.124	26.65
$v_n \times H^*$	4	69.26	17.31	0.66	0.635	7.01
$V^* \times H^*$	4	43.52	10.88	0.42	0.792	4.41
Error	8	208.77	26.10			21.14
Total	26	987.50				100

3.4.2 Optimization of printed rectangular objects

(1) Line width under optimal process parameters

At the beginning of step 2, lines are printed using optimal process parameters obtained in step 1 to get line width under optimum condition. Average width of the optimal printed line is calculated using Eq. (3.5) as 1.31 mm.

(2) Single-factor tests

In order to get a layer from lines, distance between lines d_l is calculated by Eq. (3.4). In Eq. (3.4), average width of optimal lines $\bar{w}_O$ is obtained at the beginning of step 2; and only single-factor R_W determines printing results in step 2. Single-factor tests, containing 5

experimental runs, are conducted as shown in Table 3.6 to find the optimal value of R_W. The lower-the-better SNR is used and results are listed in Table 3.6. Higher SNR represents better dimensional accuracy. Therefore, optimal R_W is found as: R_W =0.9.

Table 3.6 Single-factor tests for step 2

Experiment number	NR1	NR2	NR3	NR4	NR5
R_W	0.5	0.6	0.7	0.8	0.9
SNR of dimensional error	1.96	0.88	1.73	0.38	16.95

Consequently, optimal DIW process parameters for a layer fabricated in the prepared ink are selected as: v_n =5 mm/s, V^* =0.8, H^* =0.9, R_W =0.9.

3.5 Experimental verifications

To verify the selected process parameters and the parameters robustness on other shapes and other materials; parameter adaptability in 3D parts printing from printed layers' analyses for the proposed method and parameter adaptability in constructs fabricated as 100% infill or with porosities. Experimental verifications are presented in this section.

(1) Experimental verification for method robustness on shapes

To validate that the optimum conditions can be generalized to layers in other shapes, three shapes as Shape A (disk), Shape B (leaf) and Shape C (maple leaf) are printed under optimal condition achieved by proposed method and condition A (v_n =8 mm/s, V^* =1, H^* =0.9, R_W =0.8). As shown in Figure 3.7 (a), the dimensional quality under optimal condition is higher than that under condition A, verifying the method robustness in other shapes.

(2) Experimental verification for method robustness on materials

To verify the method robustness on materials, a well-printable cellulose-based ink is chosen proposed by the literature [68]. The ingredients of the cellulose-based ink are: 2.36% cellulose fibers, 0.59% hydroxyethylcellulose (HEC), 1.77% carboxymethyl cellulose (CMC), 0.47% montmorillonite, 0.47% citric acid (CA) and 94.34% demineralized water. The viscosity of cellulose-based ink (μ_0 =1650 $Pa \cdot s$; τ_0 = 90 Pa; K =133 $Pa \cdot s^n$; n =0.268) is much lower than that of Nivea Crème (μ_0 =1.58×10^6 $Pa \cdot s$; τ_0 = 563 Pa; K =867 $Pa \cdot s^n$; n =0.045). Thus, the cellulose-based ink has no shape retention ability after extrusion, which is just able to be printed in one layer.

The optimized process parameters for the cellulose-based ink in DIW obtained using the proposed method are: v_n =10 mm/s, V^* =0.6, H^* =0.3, R_W =0.5. As shown in Figure 3.7 (a),

printed layers in three shapes using the cellulose-based ink have high dimensional accuracy same as Nivea Crème, verifying the method robustness on materials. Moreover, compared with the optimized process parameters for cellulose-based ink (low viscosity) and Nivea Crème (high viscosity), it could be concluded that ink with higher viscosity in DIW needs smaller values for v_n and larger values for V^*, H^* and R_W.

(3) Experimental verification for parameter adaptability in 3D parts printing

In order to verify the adaptability of optimized process parameter from printed layers' analyses in 3D parts printing, three 3D models are printed using the same optimized process parameters and layer height is set as h for printed layers in Nivea Crème based DIW. As shown in Figure 3.7 (b), the printed 3D parts had good dimensional quality by comparing printed parts under optimal condition and condition A (v_n=8 mm/s, V^*=1, H^*=0.9, R_W=0.8), verifying that the proposed method has parameter adaptability in 3D parts printing from printed layers.

(4) Experimental verification for parameter adaptability in constructs with porosities

To verify the adaptability of optimized process parameter for constructs with porosities, confirmation tests are conducted as shown in Figure 3.8. Two grids named as Grids A and Grids B are designed as shown in Figure 3.8 (a): the total dimensions of grids A and grids Bare same in 31.2 mm × 31.2 mm; and the dimensions of porosity in grids A and grids B are 3 mm × 3 mm and 6.8 mm × 6.8 mm, respectively. As shown in Figure 3.8 (b) and Figure 3.8 (c), the printed single-layer and 10-layers grids had good dimensional quality by comparing printed grids under optimal condition and condition A (v_n=8 mm/s, V^*=1, H^*=0.9, R_W=0.8), verifying that the proposed method has parameter adaptability in constructs with porosities.

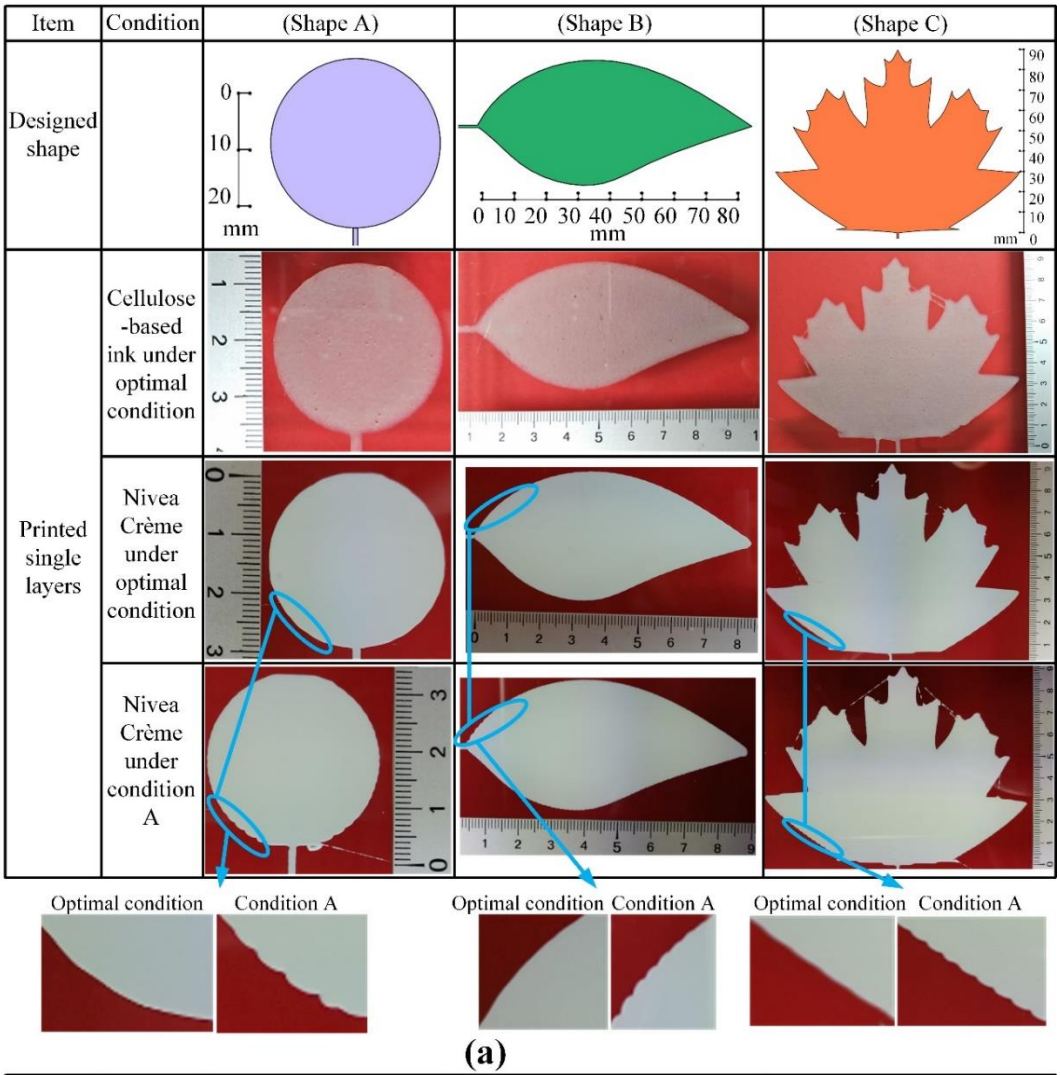

Figure 3.7 Experimental verifications for the selected process parameters in (a) verification of method robustness on layer shapes and materials; (b) verification for parameter adaptability in 3D parts printing

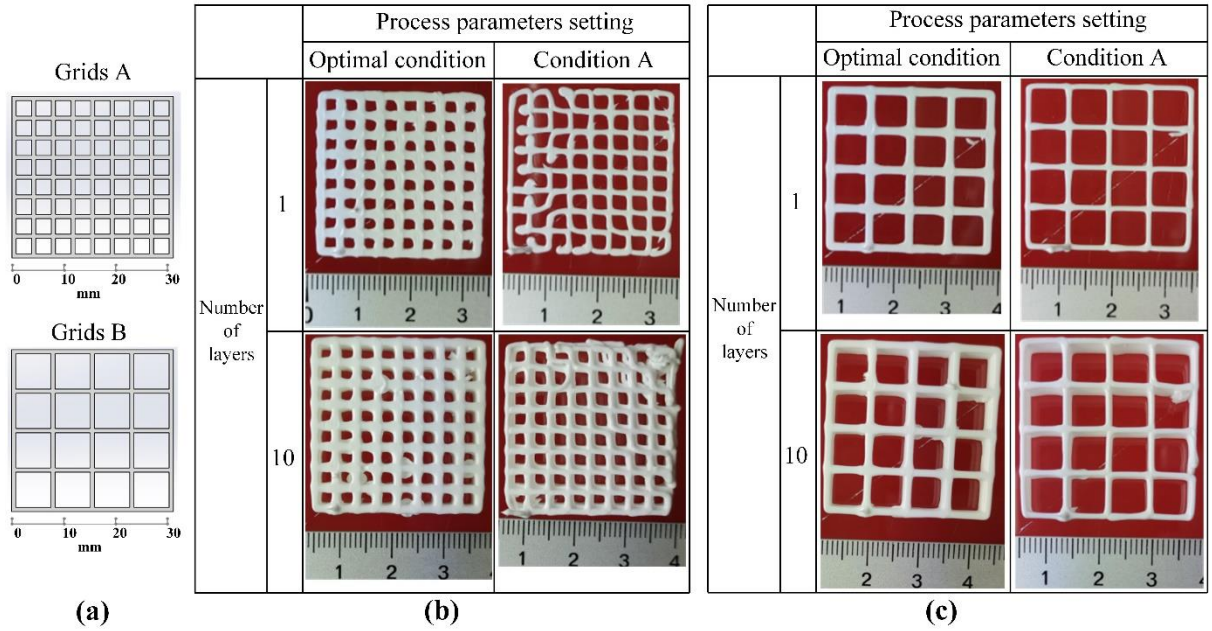

Figure 3.8 Experimental verifications for the selected process parameter in constructs with porosities: (a) two designed grids: grids A and grids B; (b) printed grids A under optimal condition and condition A in single layer and 10-layers; (c) printed grids B under optimal condition and condition A in single layer and 10-layers.

3.6 Conclusion

In this chapter, ink material properties are characterized and optimal process parameters setting is selected to provide the basis for modeling inputs. For ink material properties characterization, density, surface tension, static contact angle and rheology properties are obtained for the used ink.

For process parameters selection, the DIW process parameters are identified through process analyses and a two-step method is proposed to optimize DIW process parameters for dimensional accuracy and analyze the significance of each process parameter.

In the DIW process parameters identification, DIW process parameters for printed layers are divided into two categories and identified by process analysis as: 1) process parameters for printing a line and 2) extra process parameter from lines to a layer. The process parameters identification considers the relationship between intermediate process parameters as well as main sources of errors in the experiments. Thus, the process parameters selection method improves the efficiency and accuracy of the optimization process. In the two-step optimization method for identified DIW process parameters, Step 1 is to optimize process parameters for printing a line and Step 2 is to optimize the parameter from lines to a layer. Experimental verifications verify the proposed method and the its robustness on other shapes and other materials; parameter adaptability in 3D parts printing from printed layers' analyses for the

proposed method and parameter adaptability in constructs fabricated as 100% infill or with porosities. This proposed two-step optimization method satisfies the requirement of high quality DIW process by finding optimum process parameters setting with minimum materials and time. The proposed process parameters selection method allows a rapid and reproducible process parameters optimization of a wide variety of inks in DIW.

In conclusion, ink material property characterization and process parameters selection are conducted and presented in this chapter in order toprovide the basis for the numerical modeling of DIW.

Chapter 4: Numerical modeling, experimental verification and process analysis for DIW

4.1 Introduction

As summarized in the literature in Section 2.3.1, outputs of modeling for DIW include freeform extruded filament (FEF), deposited filament (DF), deposited corner, printed layer and 3D part. This thesis focuses on the numerical simulations of the most basic elements in DIW: FEF, DF and deposited corner.

Firstly, volume of fluid (VOF) method is selected as numerical simulation method and introduced. Then, numerical simulations, experimental verifications and process analyses for DIW are presented.

For numerical simulation of FEF, there is few works on modeling and evaluation of FEF based on numerical simulation methods for DIW. Numerical simulation modeling of FEF should fully consider ink's properties and process parameters as the quality of FEF depends both on ink's material properties and process parameters setting [119]. Evaluation of FEF should consider both the mean diameter and the stability as these two indicators have the most significant influence on the printing quality [174]. The aim of process modeling and analysis of FEF based on numerical simulations is to establish a model of FEF with numerical simulation method and then evaluate the FEF based on this model. First, model of FEF is established using numerical simulation method and two evaluation indicators, mean diameter and stability, are proposed to evaluate the FEF. Then, the selected ink, Nivea Crème, is used under three levels of piston velocity to verify the numerical simulation. After experimental verification, the model and evaluation indicators are used to analyze effect of the piston velocity on FEF and find suitable printable windows for process parameters.

For numerical simulation of DF, several researchers have established numerical prediction models for DF in MEAM. Comminal et al. [150] established a numerical model of deposited filaments in MEAM but this work lacked experimental validation. Serdeczny et al. [175] used an experimental procedure to validate the numerical model and investigated the influence of the processing conditions on cross-section of a strand printed by material extrusion AM through a numerical model. Göhl et al. [147] used a computational fluid dynamics (CFD) simulation

tool to study the effect of printing parameters on deposited filaments in bio-printing. Gosset et al. [176] presented a numerical study of the deposition of a single strand of poly-lactic acid (PLA) by MEAM via a CFD model. Although the previous works found that DF is significantly influenced by process parameters, they often failed to realize full quantitative characterizations of the detailed influence of the process parameters on the deposition status and profile dimension of deposited filaments. Meanwhile, there is few works on numerical prediction for deposited filaments in DIW by fully considering the ink material properties and process parameters setting. Thus, it is crucial and desirable to fully study and predict the deposition status and profile dimension of the deposited filaments in DIW processes based on numerical prediction.

In this chapter, an improved 3D numerical prediction model of deposited filaments in DIW is established with VOF method to predict deposition status and profile dimension of deposited filaments. Filaments deposition experiments are conducted using the selected ink to verify the proposed model. Using the proposed numerical model, the deposition status is divided into three statuses and profile dimension under each status is predicted. The effect of process parameters including the dimensionless nozzle velocity and the dimensionless height on deposition status and profile dimension has been quantified using numerical simulations for the first time. The numerical simulation of DF demonstrates a material-saving and effective approach for prediction of deposition status and profile dimension of the DF and the investigation of the effects of process parameters in DIW with computer based numerical simulations.

For numerical simulation of deposited corner, to fully understand the DIW process and improve the geometrical quality of parts in DIW, numerical simulation methods have been widely used to model the MEAM process [147, 150, 152, 177]. With the benefits of the proposed numerical simulations, researchers have successfully evaluated the printability of new prepared inks, found the optimized process parameters, analyzed the material extrusion process and realized digital twin of the MEAM process with small consumption of material and experimental time [178-180]. Comminal et al. simulated the strand deposition [150] and the material deposition along a toolpath with a sharp corner [152] with computational fluid dynamics (CFD) models to study the effect of process parameters on deposited filaments and corners, respectively. Göhl et al. [147] conducted computer based simulations for DIW to evaluate newly developed inks. Tu et al. [177] established a model of freeform extruded filaments with numerical simulation and then evaluate the filaments based on the model for

DIW. However, the previous work [152] for numerical simulation of deposited corners could only achieve the corner simulation under the condition of small angle which is less than 90 ° but failed to realize corner simulation of any angle. Thus, to overcome the limitation of the previous research for numerical simulation of deposited corners and fully realize DIW process modeling based on the application of numerical simulation, it is crucial and required to propose an improved numerical simulation to model deposited corners of any angle.

In this chapter, 3D numerical simulations of deposited corners of any angle in DIW are established with VOF method and corner deposition experiments are conducted using the selected ink to validate the proposed numerical simulation. The numerical simulation of deposition corner overcomes the limitation of previous research works in numerical simulation of deposited corners and demonstrates an effective approach for prediction of deposited corns of any angle in DIW with computer based numerical simulation.

4.2 Volume of fluid (VOF) method

The 3D numerical modeling for outputs in DIW is a two-phase flow simulation to capture the interface between the ink and air. Numerical methods for two-phase flow problem include level set method [155], phase field method [156], lattice-Boltzmann method [157], direct interface tracking method [158] and VOF method [154]. Among these numerical methods, the VOF method has been widely used in numerical simulation of filaments in MEAM due to its simplicity, robustness and straightforward implementation [159]. Thus, VOF method is adopted as simulation method in this thesis.

4.2.1 Theory of VOF

In VOF, the ink and air are treated as a single continuum and the phase fraction α is defined to distinguish the interface between the two-phase fluid as follows [181]:

$$\alpha = \frac{V_i}{V_m} \tag{4.1}$$

Where α is the phase fraction for a mesh; V_i is the volume of the ink in a mesh; V_m is the total volume of a mesh. As shown in Figure 4.1, α =0 when the mesh is filled with air and α =1 when the mesh is filled with ink. In the meshes along boundary between ink and air, the value of α belongs to (0,1). α =0.5 is defined as the cut-off value to capture the sharp front of interface between the ink and air.

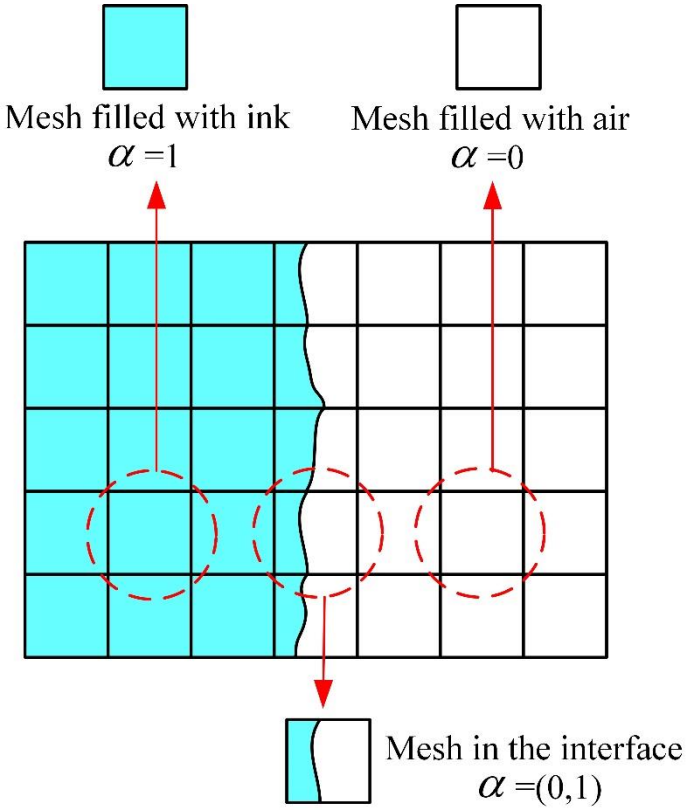

Figure 4.1 Illustration of phase fraction in volume of fluid (VOF) method

Fluid properties of the single continuum are weighted with the phase fraction as follows:

$$\rho_s = \alpha\rho + (1-\alpha)\rho_a \tag{4.2}$$

$$\mu_s = \alpha\mu + (1-\alpha)\mu_a \tag{4.3}$$

Where ρ_s and μ_s is density and viscosity of the single continuum; ρ and ρ_a is density of the ink and air, respectively; μ and μ_a is viscosity of the ink and air, respectively. μ is expressed using the Hershel-Bulkley model (HBM) due to its shear-thinning behaviour as shown in Eq. (3.2).

The following assumptions about the numerical simulations of DIW are formulated:

- The deposition process is considered isothermal as the process is conducted at room temperature;
- The material is considered incompressible with constant ρ;
- The ink adheres to the surfaces of the nozzle without slip and the static contact angle between ink and the substrate is considered;
- The filaments flow is laminar.

Based on these assumptions, the governing equations for the numerical simulation include continuity equation, momentum equilibrium equation and phase fraction equation. Each equation is written as follows [182].

Continuity equation:

$$\nabla \cdot \mathbf{U} = 0 \tag{4.4}$$

Where $\mathbf{U}$ is velocity field of the fluid.

Momentum equilibrium equation:

$$\frac{\partial \rho_s \mathbf{U}}{\partial t} + \nabla \cdot \left(\rho_s \mathbf{U}\mathbf{U}\right) = -\nabla p + \nabla \cdot \left(\rho_s \mu_s \nabla \mathbf{U}\right) + \rho_s \mathbf{g} + \mathbf{F}_\sigma \tag{4.5}$$

Where p is the pressure in the fluid; $\mathbf{g}$ is the gravitational acceleration vector; $\mathbf{F}_\sigma$ is surface tension. $\mathbf{F}_\sigma$ is calculated as follows:

$$\mathbf{F}_\sigma = \sigma \kappa \nabla \alpha \tag{4.6}$$

where σ is the surface tension coefficient; κ is the surface curvature which is depended on the shape of deposited ink on the substrate. κ is computed from local gradients in the surface normal to the interface as follows [183]:

$$\kappa = \frac{1}{|\mathbf{n}|}\left(\left(\frac{\mathbf{n}}{|\mathbf{n}|}\cdot\nabla\right)|\mathbf{n}| - \nabla \cdot \mathbf{n}\right) \tag{4.7}$$

where $\mathbf{n} = \nabla \alpha$ is the normal vector to the ink surface. Wall adhesion between deposited ink and substrate is considered in the model based on the use of the static contact angle as:

$$\hat{\mathbf{n}} = \hat{\mathbf{n}}_w \cos\theta_c + \hat{\mathbf{t}}_w \sin\theta_c \tag{4.8}$$

where $\hat{\mathbf{n}} = \mathbf{n}/|\mathbf{n}|$ is the unit vector normal to the ink surface, $\hat{\mathbf{n}}_w$ and $\hat{\mathbf{t}}_w$ represents the unit vector normal and tangent to the substrate, respectively, θ_c is the static contact angle between the ink and substrate.

Phase fraction equation:

$$\frac{\partial \alpha}{\partial t} + \nabla \cdot \left(\alpha \mathbf{U}\right) + \nabla \cdot \left(\alpha\left(1-\alpha\right)\mathbf{U}_\mathbf{r}\right) = 0 \tag{4.9}$$

Where $\mathbf{U}_\mathbf{r}$ is velocity vector compressing two-phase free surface, which represents the velocity difference between two-phase fluids and can be calculated as follows:

$$\mathbf{U}_\mathbf{r} = \min\left(c|\mathbf{U}|, \max|\mathbf{U}|\right)\frac{\nabla \alpha}{|\nabla \alpha|} \tag{4.10}$$

Where c is controllable compression factor and it is selected as c=1 in the numerical simulation.

4.2.2 Implementation of VOF

The free and open-source CFD software OpenFOAM v1912 [184] is used to realize the numerical simulation of the DIW. In the numerical simulation, OpenFOAM v1912 is used to build geometrical model, generate meshes, determine boundary conditions and solve governing equations. Especially, the governing equations in VOF are solved based on the solver for two incompressible, isothermal immiscible fluids using VOF method with optional mesh motion and mesh topology changes including adaptive re-meshing, *interFoam*. PIMPLE algorithm, a combined algorithm of the pressure-implicit split-operator (PISO) and the semi-implicit method for pressure-linked equations (SIMPLE) algorithms, is chosen as the numerical algorithm for *interFoam* solver.

After numerical simulation in OpenFOAM v1912, ParaView, which is an open-source, multi-platform data analysis and visualization application [185], is used to build visualizations and analyze simulation data.

In this thesis, hardware condition for the numerical simulations is as follows:

Computer: Dell precision T1700; processor in computer: Intel XEON; simulation software: OpenFOAM v1912.

4.3 Numerical simulation of FEF

4.3.1 Numerical Modeling

As shown in Figure 4.2 (a), FEF is produced by extruding ink in the syringe through the nozzle into the air with the piston movement. Dimensions of the geometrical model of FEF in DIW include: the piston diameter D_p; the initial filled length of ink L_0; the nozzle inner diameter d_n; the nozzle outer diameter D_n; the nozzle length L_n; the gap between nozzle bottom and substrate h. In this modeling, h is set as 26 mm to avoid FEF touching the substrate. D_p, d_n, D_n, L_n and L_0 are set to match the actual device dimensions: 21.6 mm, 0.84 mm, 1.22mm, 18 mm, 30 mm, respectively. Figure 4.2 (b) presents the 3D model established in OpenFOAM for FEF at the initial time, where red regime represents the ink and blue regime represents the air. As shown in Figure 4.2 (c), the 3D model is simplified into a 2D axisymmetric model by capturing 1/120 of the 3D model in the circumferential direction to reduce computation cost under the axisymmetric laminar flow condition for the ink extrusion.

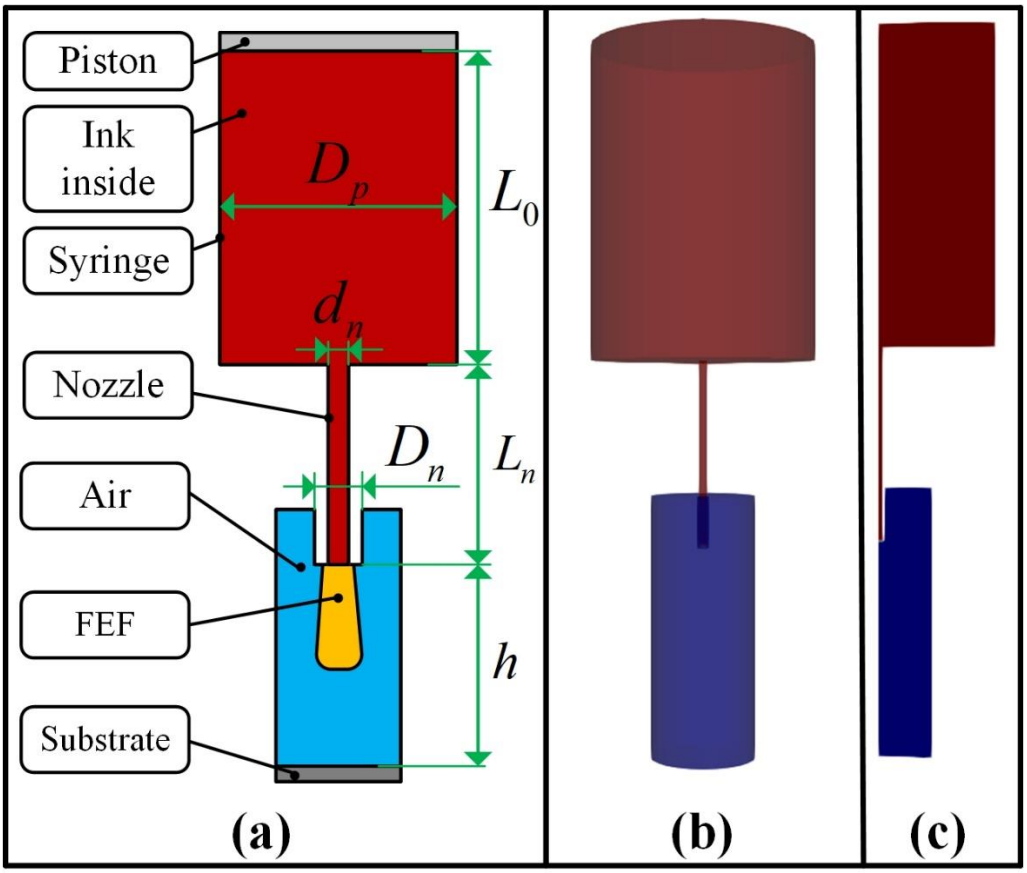

Figure 4.2 Geometrical model of FEF in numerical simulation for DIW: (a) dimensions of the geometrical model; (b) established 3D model at the initial time; (c) simplified 2D axisymmetric model at the initial time

OpenFOAM is designed as a code for 3D space and defines all meshes as 3D meshes, but wedge type meshes are used for 2D axisymmetric problems specifically [186]. Thus, wedge type meshes are used for the simplified 2D axisymmetric model as shown in Figure 4.3 (a), where lengths and widths of meshes in the same area are set nearly same and meshes in the junction of different areas are refined to improve calculation accuracy. Total number of the meshes is 18996. Boundary conditions are grouped into 5 categories and are defined as shown in Figure 4.3 (b) and Table 4.1.

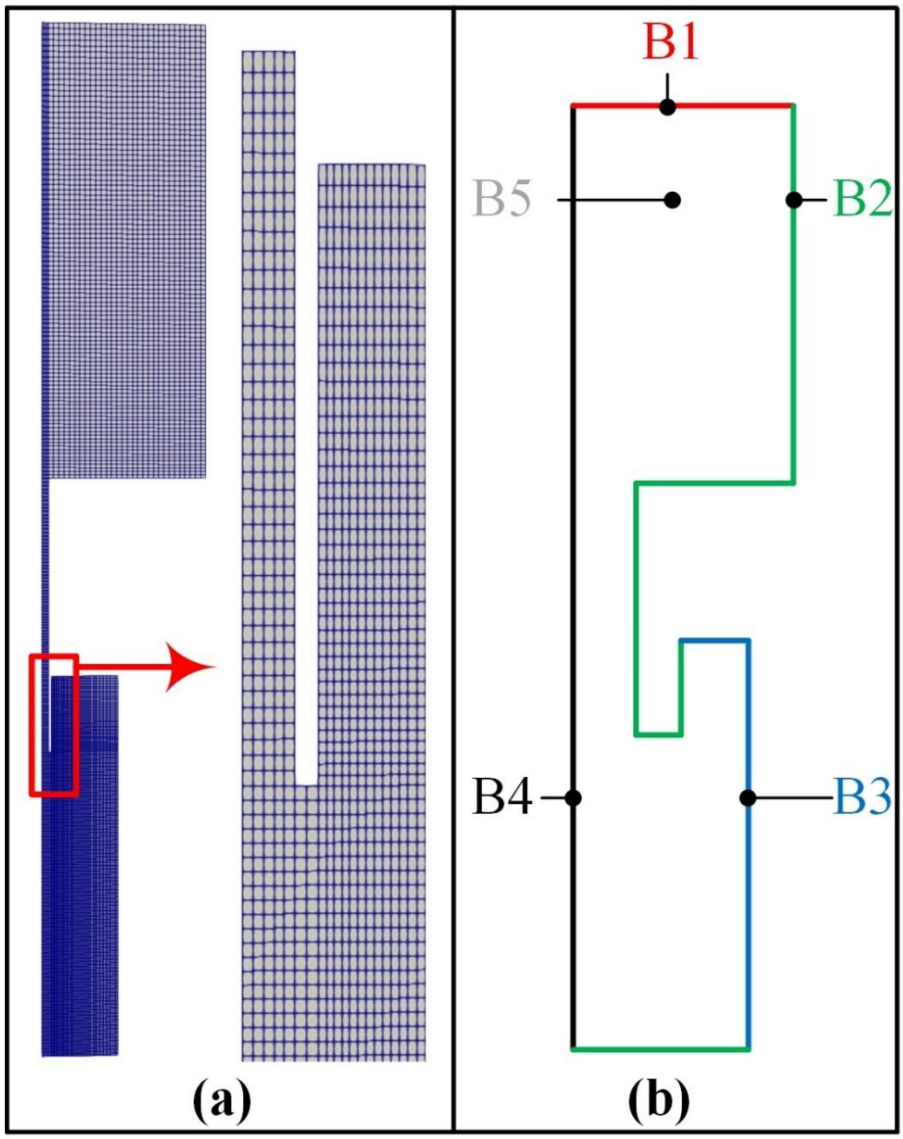

Figure 4.3 Meshes and boundary conditions for model of FEF in numerical simulation for DIW: (a) meshes; (b) boundary conditions

Table 4.1 Definition of boundary conditions for numerical model of FEF

Name	Physical meaning	Type	Setting
B1	Piston	Moving boundary	Velocity is equal to piston velocity
B2	Inner walls of syringe; walls of nozzle and substrate	No-slip boundary	No-slip
B3	Air	InletOutlet boundary	Depended on dynamic calculation
B4	Symmetrical axis	Symmetrical boundary	Empty condition
B5	Front and back side symmetrical sections	Wedge boundary	Symmetrical condition

4.3.2 Experimental verification

In order to validate the proposed numerical model of FEF, the selected ink Nivea Crème is used as ink for FEF extrusion tests in a DIW 3D printer. As shown in Figure 4.4 (a), a piston driven DIW 3D printer TM-081 (Tobeca Company, France) is used to extrude ink in the syringe into FEF in the air; and a camera (Canon LEGRIA HF R86 Noir, Canon Inc., Japan) is used to take photos of FEF. As shown in Figure 4.4 (b), the extrusion tool in the DIW 3D printer is composed of a 30mL syringe (Braun Melsungen AG, Germany) and a precision engineered fluid dispensing nozzle (Nordson EFD, USA). Dimensions of extrusion tool are: h =26 mm, D_p =21.6 mm, d_n =0.84 mm, D_n =1.22mm, L_n =18 mm, L_0 =30 mm (same as the setting in numerical simulation modelling in Section 4.3.1). The ink material properties of Nivea Crème are used the value in Table 3.1 obtained in Section 3.2.3.

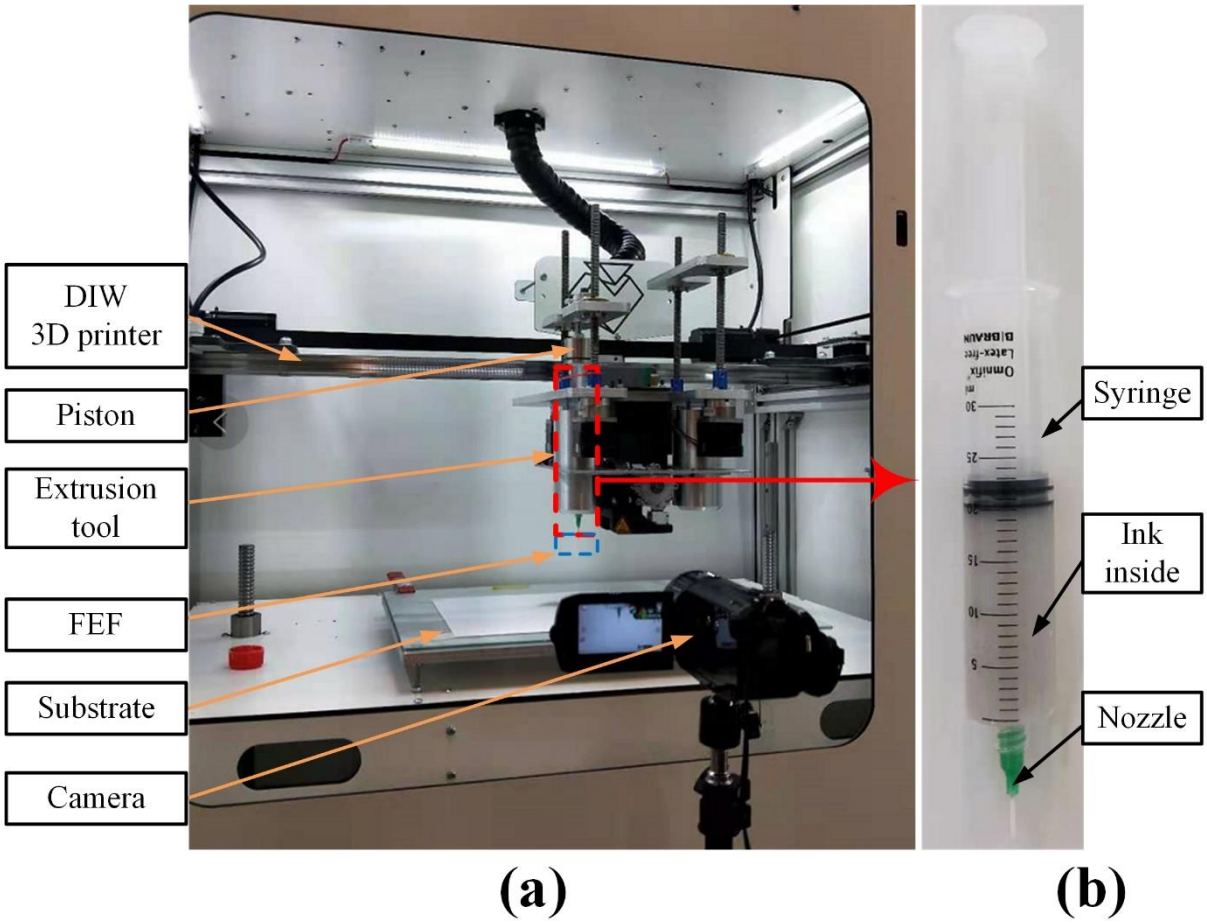

Figure 4.4 Experimental validation setup for the numerical simulation of FEF: (a) producing FEF using DIW 3D printer and observing FEF using camera; (b) extrusion tool in the DIW 3D printer

Disregarding ink compressibility, the mass conservation for the FEF producing process is expressed as:

$$v_p / v_e = \left(d_n / D_p\right)^2 \tag{4.11}$$

Where v_p is the piston velocity, v_e is average velocity of FEF.

To verify the numerical simulation of FEF considering the universality for different process parameters, 3 levels of v_p are set by setting v_e from 5 mm/s to 15 mm/s at fixed intervals of 5 mm/s, which are on the printable range. The 3 levels setting for v_p is summarized in Table 4.2. The simulation calculation time of FEF is 10 minutes.

Table 4.2 Piston velocity setting in the experimental validation for numerical simulation of FEF

Levels	v_1	v_2	v_3
v_e (mm/s)	5	10	15
v_p (10^{-3} mm/s)	7.56	15.12	22.68

Simulation and experimental results for the selected ink Nivea Crème under 3 levels of v_p are plotted in Figure 4.5. Here, all images are plotted using the same graphical scale in order to provide a direct comparison of simulation and experimental results. Modeling is verified by comparing simulation and experimental results for shape and diameter accuracy. For shape, all simulation results had continuous extruded profiles in accordance with experimental results by observing images in Figure 4.5. Diameter prediction accuracy is defined as verification indicator to verify the prediction accuracy of the model as follow:

$$E_f = \sqrt{\frac{\sum_{i=1}^{N_f} e_{fi}^2}{N_f}} \tag{4.12}$$

Where E_f is diameter prediction accuracy of numerical simulation of FEF, N_f is the number of measurement points in FEF where N_f points are evenly set on the FEF starting from the nozzle bottom, e_{fi} is the diameter difference between experimental and simulation results at i point.

In this verification, the length of FEF is 5.2 mm; the interval of measurement points is 0.5 mm and N_f is 10. Diameter prediction accuracy for the Nivea Crème are 0.02 mm, 0.08 mm and 0.04 mm for v_1, v_2 and v_3, respectively, where the maximum error is 0.08 mm and the maximum relative error is 9.52%, verified the numerical simulation model of FEF had a high diameter accuracy. Thus, the model is verified both from shape and diameter accuracy.

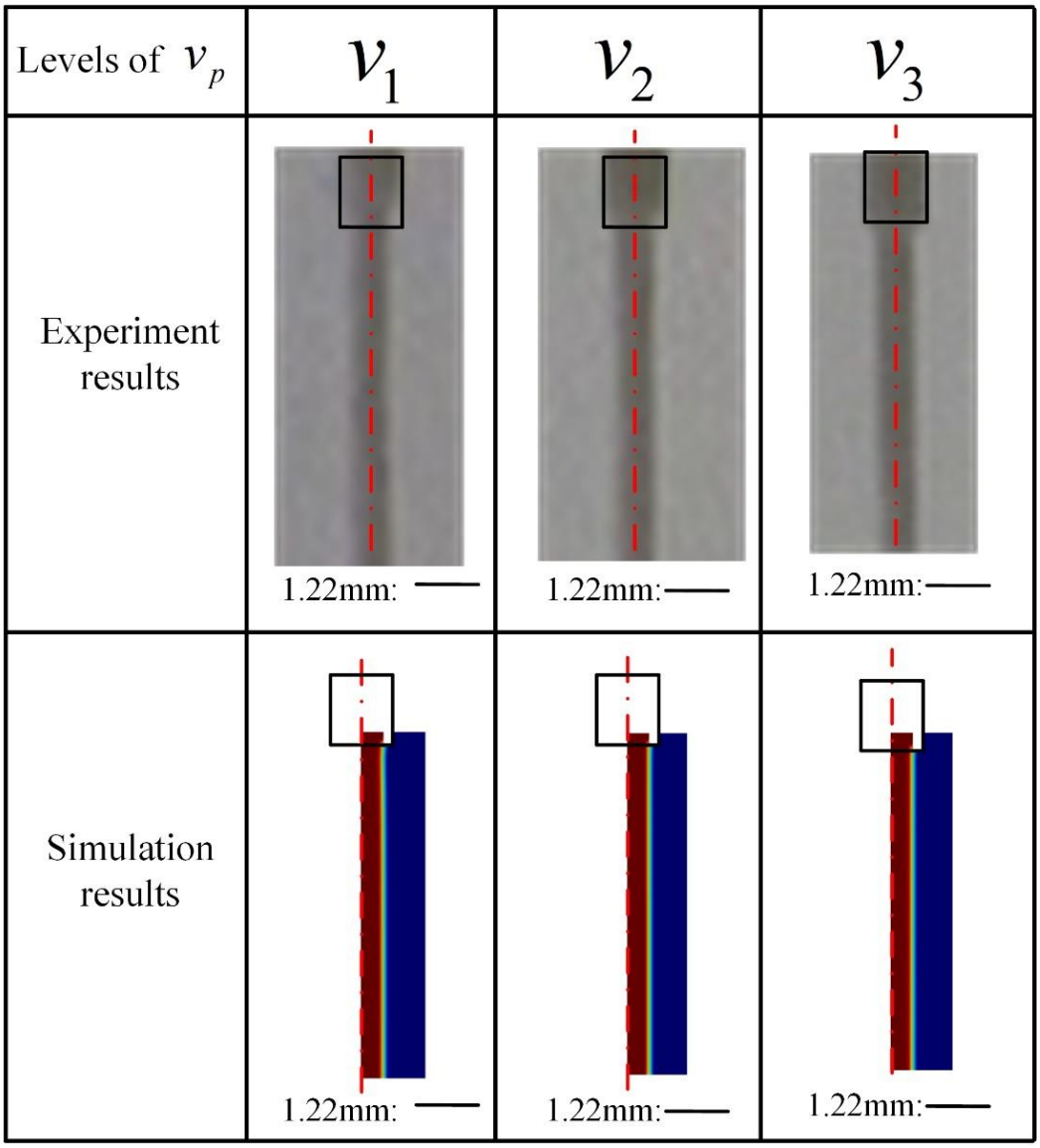

Figure 4.5 Simulation and experimental results of FEF under 3 levels of piston velocities for the selected ink Nivea Crème

4.3.3 Process analysis

After experimental verification, the simulation model of FEF is used to evaluate the effect of the piston velocity on the FEF and find suitable printable windows for process parameters by defining evaluation indicators of FEF.

(1) Evaluation indicators

Defined evaluation indicators of FEF include mean diameter and stability as continuous and tubular FEF with diameters close to the actual nozzle inner diameter is the basic requirement for a successful extrusion-based AM [187]. N_f measuring points are set along the FEF uniformly from nozzle bottom at fixed sampling intervals of 0.5 mm and diameter on each

measuring point is measured as $d_{fi}\left(i=1,2,...,N_f\right)$. Mean diameter and stability of FEF are expressed using average and standard deviation of $d_{fi}\left(i=1,2,...,N_f\right)$, respectively.

(2) Evaluation of FEF

Based on the evaluation indicators, process analysis is conducted. Firstly, v_p are set by setting v_e from 1 mm/s to 20 mm/s with Eq. (4.11) and used as input conditions in the proposed numerical model of FEF. Then, the two evaluation indicators are used to evaluate FEF under different piston velocities based on the model. As shown in Figure 4.6, there is no continuous and stable FEF when setting of v_e is lower than 2 mm/s for the Nivea Crème as piston velocity should be large enough to let FEF overcome yield stress and surface tension to produce continuous and stable filaments. The minimum setting of v_e to produce stable FEF for the ink depends on yield stress and surface tension coefficient of the ink.

When setting of v_e is higher than minimum setting of v_e to produce stable FEF, mean diameters of FEF decrease with increasing setting of v_e for the Nivea Crème. Especially, mean diameters of FEF get closer to the nozzle inner diameter as setting of v_e increases ranging from 1 mm/s to 10 mm/s and is equal to nozzle inner diameter when setting of v_e is 10 mm/s (Figure 4.6 (a)). Then, it moves further away from the nozzle inner diameter as the setting of v_e is higher than 10 mm/s. As shown in Figure 4.6 (b), stability decreases firstly and then increases as setting of v_e increases ranging from 1 mm/s to 20 mm/s for the Nivea Crème. Considering the requirement that FEF should have mean diameter close to nozzle inner diameter and good stability, printable window of setting of v_e for FEF is summarized from Figure 4.6: 5 mm/s-15 mm/s for Nivea Crème. This is consistent with the optimal v_e (5 mm/s) obtained by the experimental method in Section 3.3.

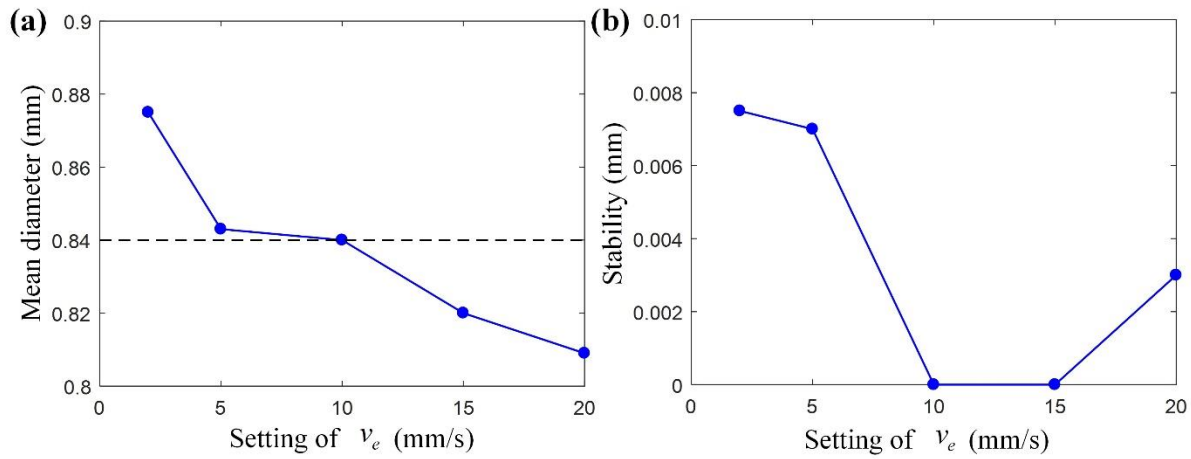

Figure 4.6 Evaluation of the FEF for the Nivea Crème using the defined two evaluation indicators as: (a) mean diameter; (b) stability

4.4 Numerical simulation of DF

4.4.1 Numerical Modeling

Numerical modeling for the 3D profile of DF is established based on the use of free and open-source CFD software OpenFOAM v1912 as shown in Figure 4.7. Because the ink extrusion and deposition process are considered as an isothermal, incompressible and laminar flow, the average velocity on each cross section in the nozzle is the same and it can be expressed as Eq. (4.11) based on conservation of mass.

According to Eq. (4.11), the flow situation in syringe has no effect on v_e. Thus, the 3D geometrical model is simplified as a combination of the nozzle, substrate and air by neglecting the syringe to improve computational efficiency as shown in Figure 4.7 (a). As presented in Figure 4.7 (b), the critical parameters in the model include the inner diameter of nozzle d_n, the outer diameter of nozzle D_n, the average velocity of ink in nozzle v_e, the nozzle length L_n, the distance between nozzle bottom and substrate h, and the nozzle velocity v_n. In the numerical simulation of DF, the values of d_n and D_n are set as 0.84 mm and 1.22 mm, which match the actual dimensions of DIW 3D printer in experimental verification, respectively. v_e is calculated using Eq. (4.11) where the value of D_p is set as 21.6 mm. As the nozzle length has no effect on v_e and the final DF, the value of L_n is set as 2.44 mm which is smaller than practice nozzle length (18 mm) to reduce computational time. To avoid the model becoming a complex dynamic-mesh model which needs a large amount of computational time, the position of nozzle is fixed while the substrate is attached with a moving velocity v_n in the boundary setting as the

movements of the nozzle and substrate are relative to each other. As shown in Figure 4.7 (c), meshes are refined in the region of DF to improve calculation efficiency and accuracy.

The initial condition of phase fraction is shown in Figure 4.7 (d) where red region represents the ink and blue region represents the air, meaning that the ink is filled in the nozzle at the initial time. Finally, the 3D profile of DF is obtained through VOF by capturing the sharp front of interface where the value of α is 0.5. And the visualization of the deposited filaments is realized using the open-source, multi-platform data analysis and visualization software, ParaView.

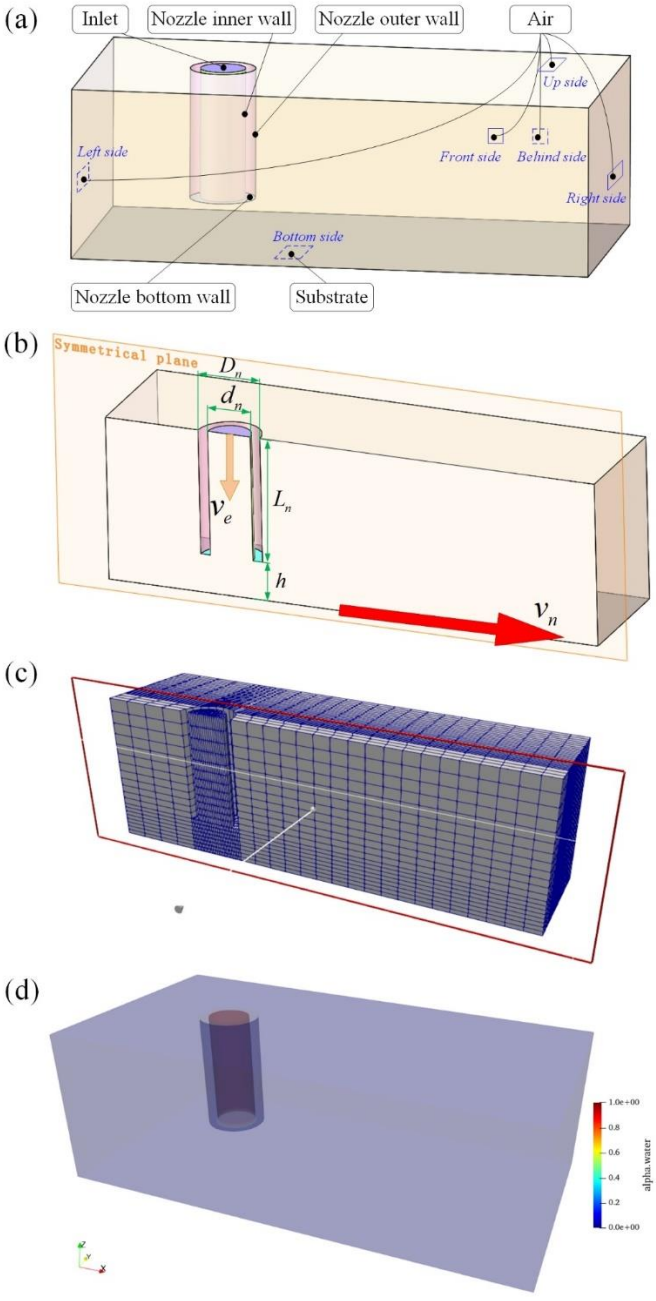

Figure 4.7 Numerical modeling of 3D profile of DF: (a) 3D geometrical model; (b) critical parameters in the model; (c) generated meshes; (d) initial condition of phase fraction

4.4.2 Experimental verification

Yuk and Zhao [188], Comminal et al. [150] and Athanasiadis et al. [125] have summarized that the deposition and the profile dimension of the DF in MEAM are significantly influenced by the dimensionless nozzle velocity $V^* = v_n / v_e$ (ratio of nozzle velocity v_n to average velocity of ink in the nozzle v_e) and the dimensionless height $H^* = h / d_n$ (ratio of distance between nozzle bottom and substrate h to inner diameter of nozzle d_n).

The deposition process and the process parameters of DIW are illustrated in Figure 4.8 (a). Ink is filled in the syringe at the initial filled length and the full nozzle first. When piston started moving at a fixed velocity v_p, ink is extruded out from nozzle. By setting the distance between nozzle bottom and substrate as h and the nozzle velocity related to substrate in the horizontal direction as v_n, the FEF is deposited on the substrate. Through observations of cross-sectional shapes under different process parameters, it is summarized that there are three deposition statuses for cross-sectional shapes of DF: over-deposition, pressed-deposition and freeform-deposition. When h is much smaller than d_n or v_n is much smaller than v_e, the DF is in over-deposition status. In over-deposition status as shown in Figure 4.8 (b), excessive ink is squeezed out beyond the outer diameter of the nozzle and width, height of DF are irregular and cannot be predicted. When h and v_n increased, the status would change to pressed-deposition as shown in Figure 4.8 (c) first and then change to freeform-deposition as shown in Figure 4.8 (d). In pressed-deposition status, the height of DF h_d is equal to h as DF is pressed by nozzle bottom and the two ends of the cross-sectional of DF are regular semicircles with a diameter of h_d. In freeform-deposition status, the filament is deposited without nozzle contact and cross-sectional shape is a part of circle dependent on the static contact angle θ_C between the ink and the substrate. The simulation calculation time of DF is 40 minutes.

To determine deposition statuses, the dimensionless nozzle velocity V^* and the dimensionless height H^* are used. Using the law of conservation of mass, the conditions of over-deposition and freeform-deposition could be expressed as Eq. (4.13) and Eq. (4.14), respectively.

$$\frac{\pi}{4} d_n^{\,2} v_e \geq h \cdot D_n \cdot v_n \tag{4.13}$$

$$\frac{\pi}{4} d_n^{\,2} v_e \leq \left(\theta_C - \frac{\sin 2\theta_C}{2} \right) \left(\frac{h}{1 - \cos \theta_C} \right)^2 v_n \tag{4.14}$$

Then, Eq. (4.13) and Eq. (4.14) are simplified as Eq. (4.15) and Eq. (4.16), respectively using V^* and H^*.

$$V^* \le \frac{\pi}{4\beta} \cdot \frac{1}{H^*} \tag{4.15}$$

where β is the ratio of D_n to d_n ($\beta = D_n / d_n$).

$$V^* \ge \frac{\pi}{4\gamma} \cdot \left(\frac{1}{H^*} \right)^2 \tag{4.16}$$

where γ represented $\left(\theta_C - \frac{\sin 2\theta_C}{2} \right) \left(\frac{1}{1 - \cos\theta_C} \right)^2$.

The dividing line 1 (solid red line) and dividing line 2 (solid blue line) described by Eq. (4.15) and Eq. (4.16) are plotted in Figure 4.8 (d) to predict deposition statuses under different V^* and H^*. Combinations of V^* and H^* are divided into three areas by dividing line 1 and dividing line 2: area below dividing line 1 represents over-deposition; area between dividing line 1 and dividing line 2 represents pressed-deposition and area above dividing line 2 represents freeform-deposition.

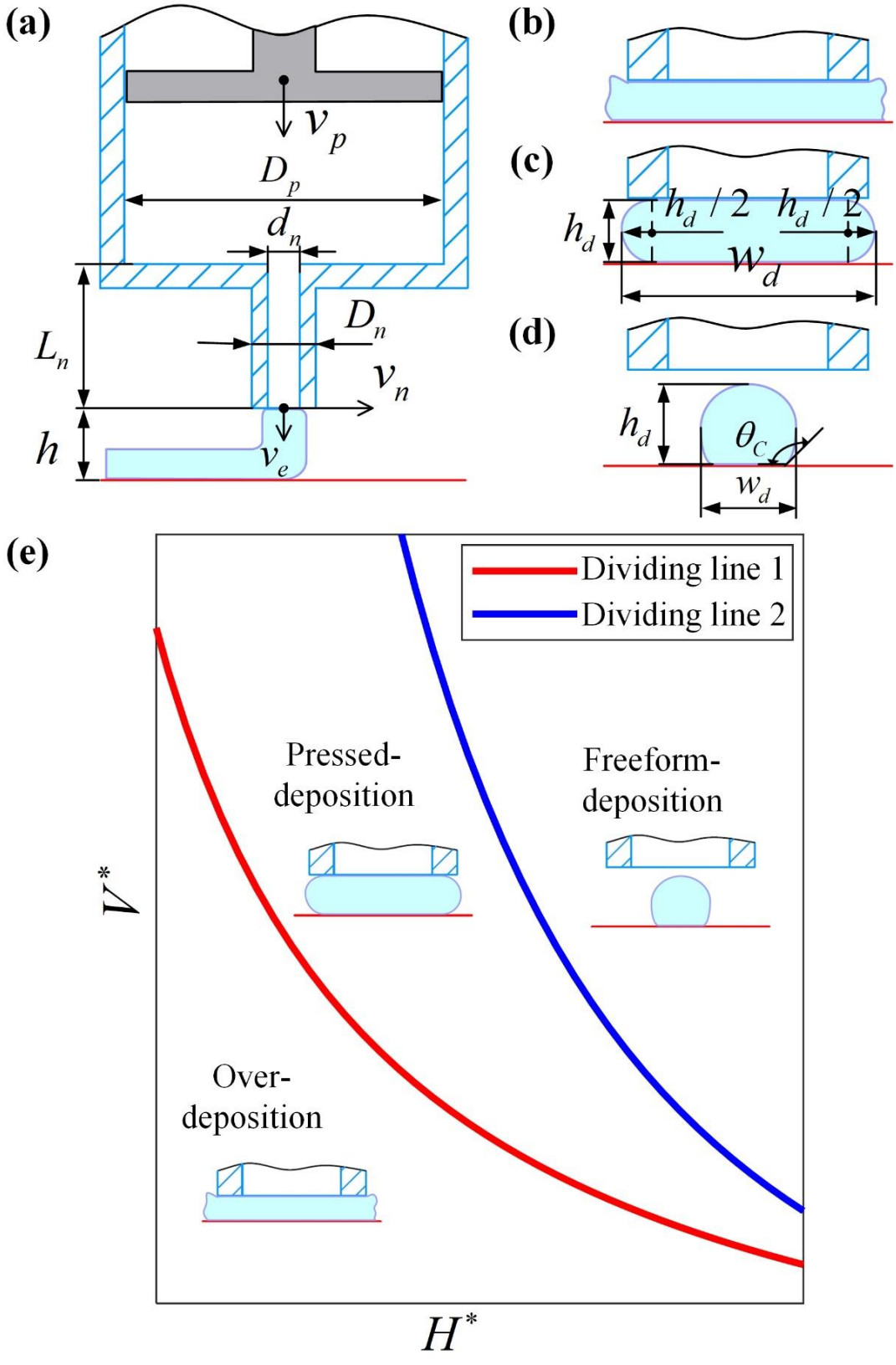

Figure 4.8 Analyses of deposition statuses and cross-sectional shapes of DF: (a) illustration of deposition process and process parameters; three deposition statuses for cross-sectional shapes of DF as (b) over-deposition, (c) pressed-deposition and (d) freeform-deposition; (e) cross-sectional shapes statuses division

Thus, to fully verify the numerical simulation of DF in deposition status, width and height. First, v_e is set as two-level process parameter which is 6 mm/s and 9 mm/s to investigate the influence of v_e on the deposition status. Then, at each level of v_e, V^* is varied from 0.4 to 1.2 at a fixed interval of 0.4 and H^* is varied from 0.3 to 1.5 at a fixed interval of 0.3 to investigate the influence of V^* and H^* on deposition status.

The quantitative comparison of the profile dimension is conducted by measuring width and height of the cross-section of the DF. A piston-driven DIW 3D printer TM-081 (Tobeca Company, France) with the selected ink is used to conduct filaments deposition experiments (Figure 4.9). In the experiments, process parameters are set first and then three 80 mm long filaments are deposited on a glass substrate and a camera (Canon LEGRIA HF R86 Noir, Canon Inc., Japan) is used to capture top and side views of deposited filaments to determine the deposition status and profile dimension of deposited filaments. The width of deposited filaments is measured at a fixed sampling interval of 5 mm for three filaments in the top view and the height is measured in the end face for three filaments in the side view. The average and standard deviation are calculated for 45 sampling points in width measurement and 3 sampling points in height measurement. Experimental width and height are expressed as the mean ± standard deviation.

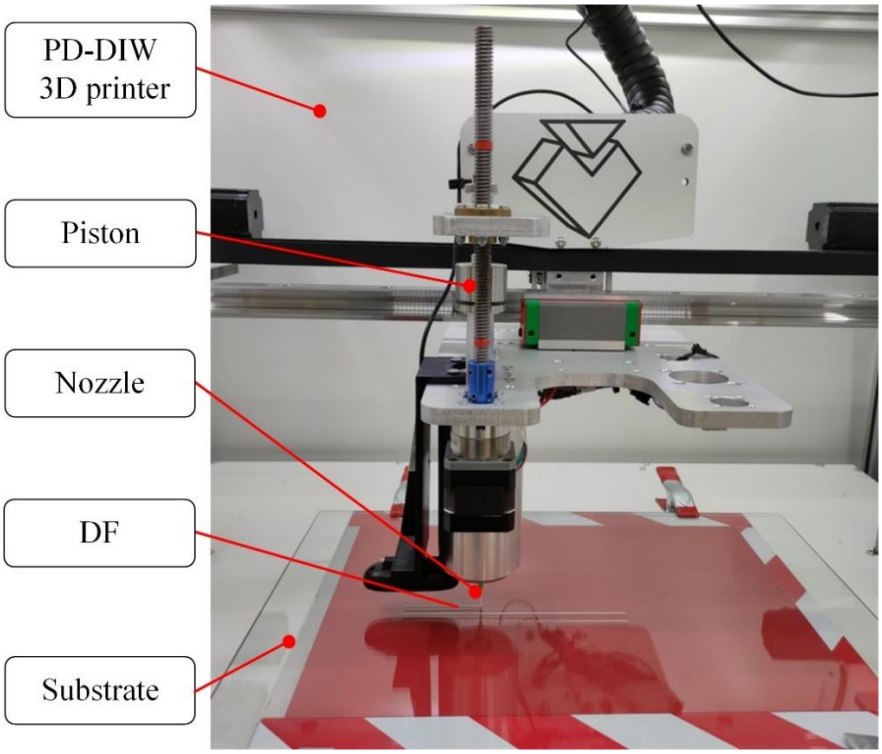

Figure 4.9 Experimental setup for filaments deposition experiments and corners deposition experiments

4.4.2.1 Experimental verification of deposition status for DF

Figure 4.10 represents the characterization of the three deposition statuses in experimental results from top view and side view and the characterization of the three deposition statuses in simulated results from 3D shape and cross-section, which show a good consistency of experimental and simulated results in the deposition status characterization. In the over-deposition status, the two ends of the cross-section are irregular shapes which are higher than h. In the pressed-deposition status, the height of cross-section is equal to h and the two ends of the as-deposited filaments possess semicircle shapes with a diameter of the same value of h. In the freeform-deposition, the cross-section nearly takes a circle shape.

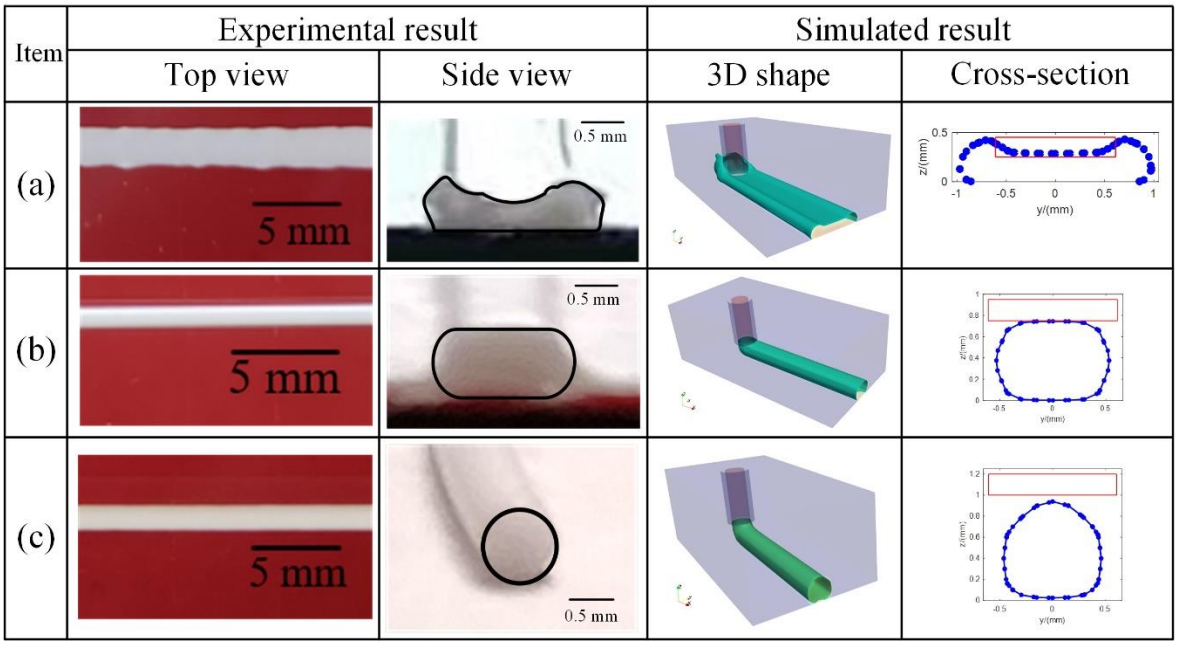

Figure 4.10 Characterization of deposition status in experimental and simulated results: (a) over-deposition; (b) pressed-deposition; (c) freeform-deposition

In order to investigate the influence of the process parameters on the deposition status, the experimental and simulated deposition status under different process parameters are compared. By using the symbols +, ■ and ● to represent over-deposition, pressed-deposition and freeform-deposition respectively, the experimental statuses of the deposited filaments under different process parameters are summarized in Figure 4.11. Correspondingly, the simulated deposited filaments under different process parameters are plotted in Figure 4.12 by using pink, green and cyan backgrounds to represent over-deposition, pressed-deposition and freeform-deposition respectively. It can be found that the effectiveness of the numerical prediction for the deposited filaments is validated as the simulated deposited statues dividing results are consistent with the experimental results and is also consistent with the idealized results.

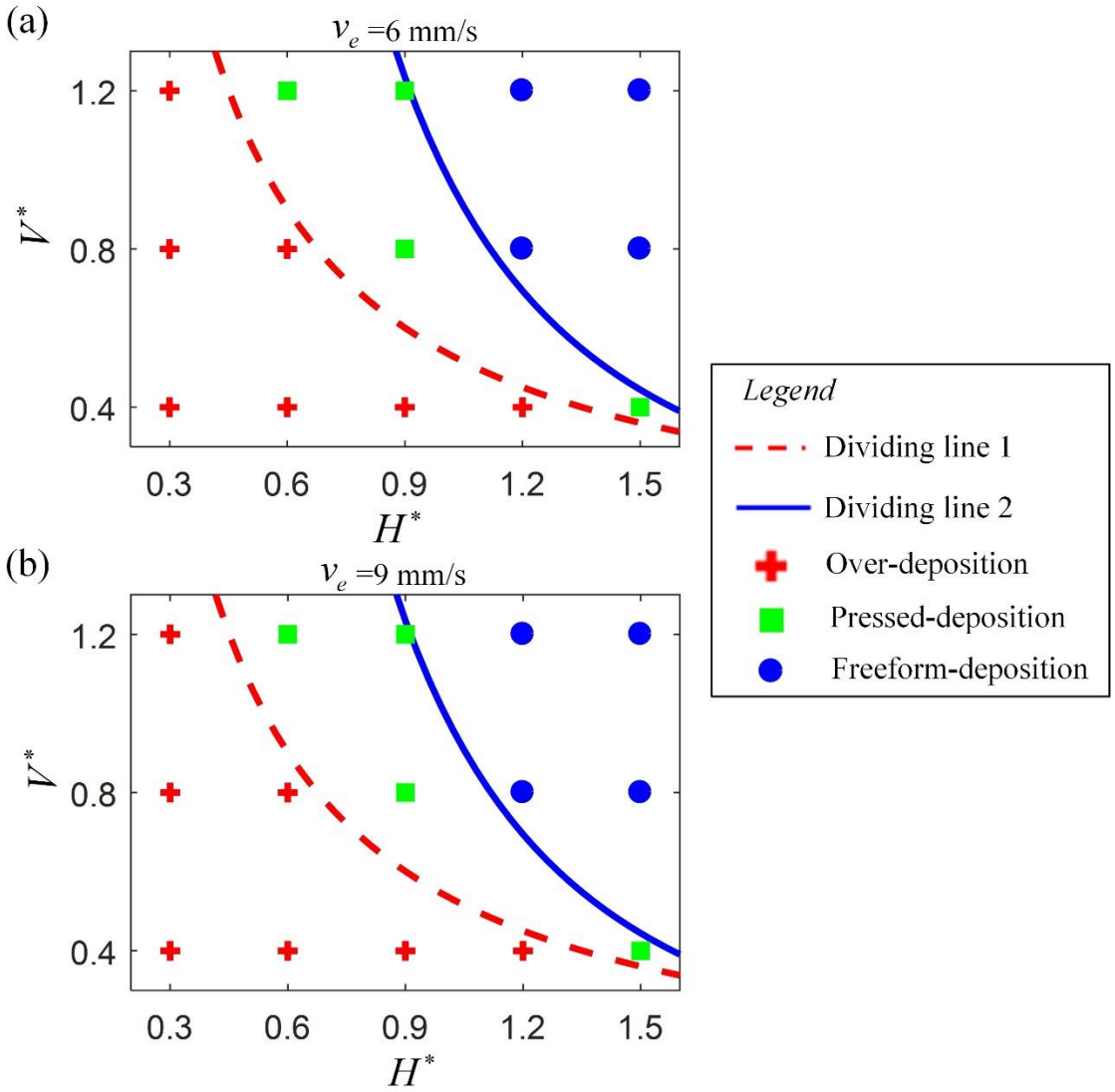

Figure 4.11 Experimental deposited status of the deposited filaments under different process parameters: (a) the value of v_e is set as 6 mm/s; (b) the value of v_e is set as 9 mm/s

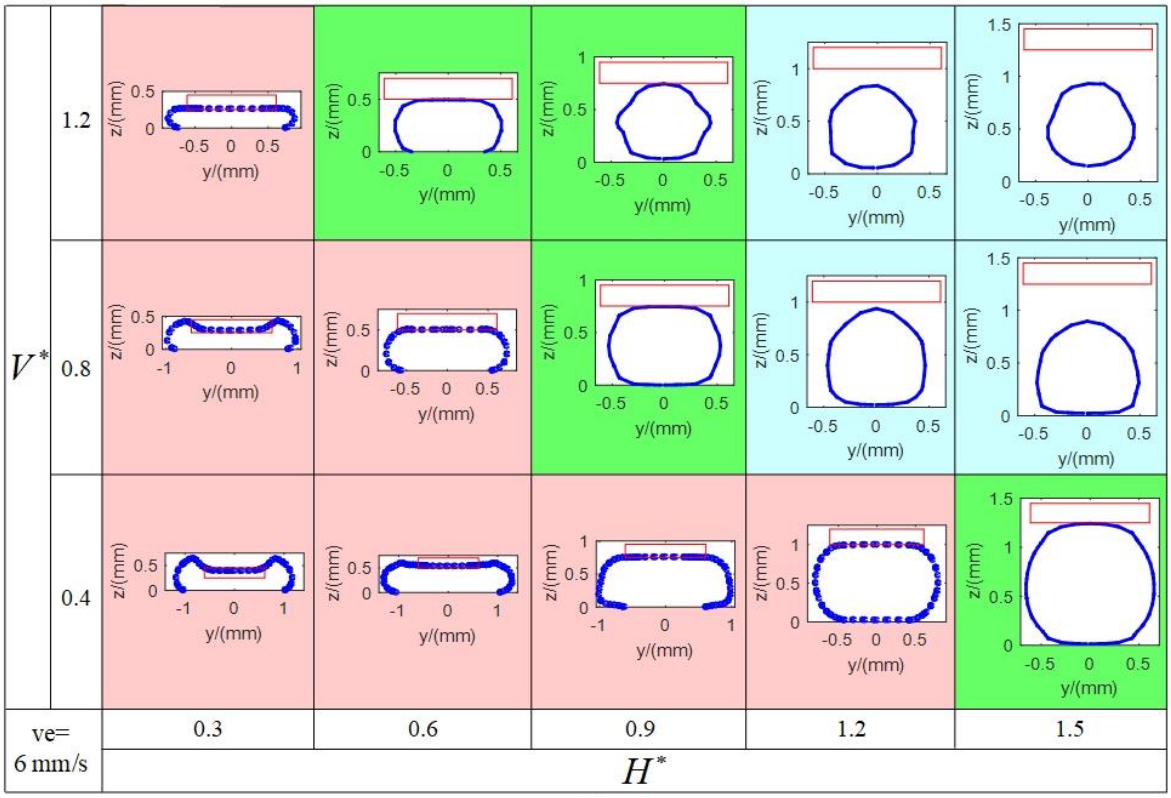

(a)

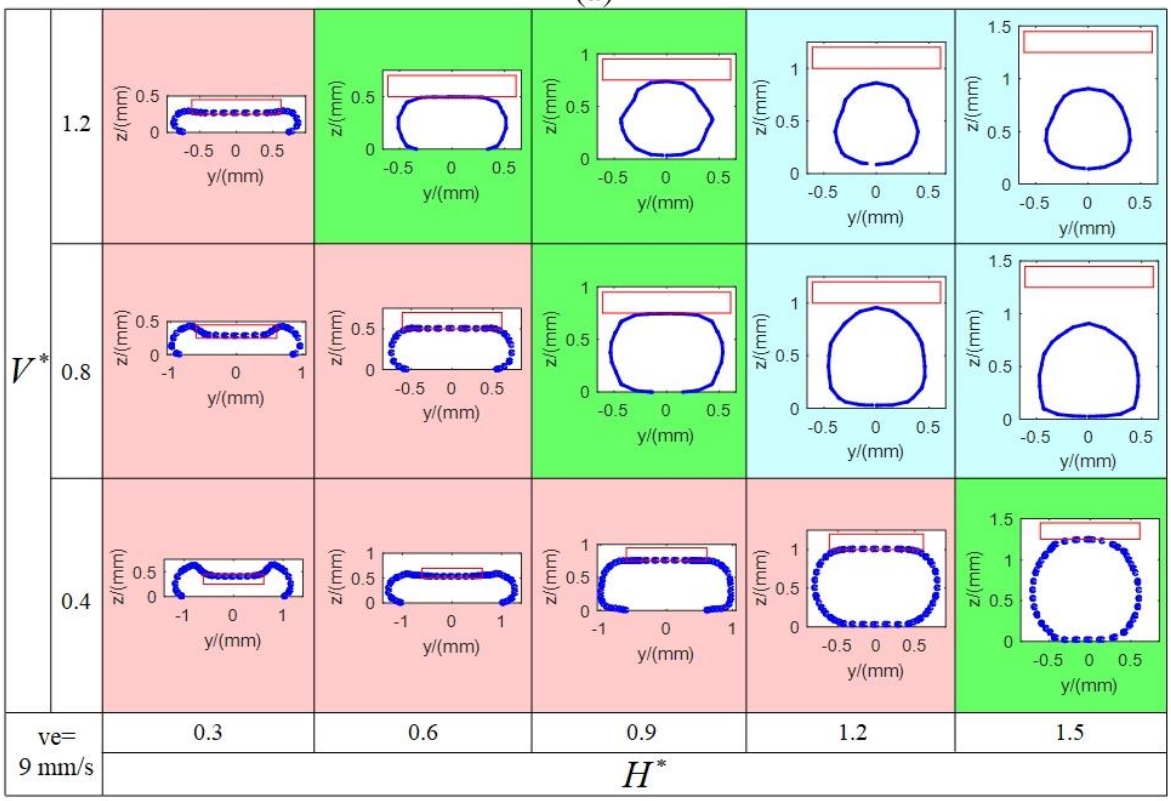

(b)

Note: means over-deposition; means pressed-deposition; means freeform-deposition.

Figure 4.12 Simulated deposition status of the DF under different process parameters: (a) the value of v_e is set as 6 mm/s; (b) the value of v_e is set as 9 mm/s

4.4.2.2 Experimental verification of profile dimension for DF

The DF in pressed-deposition and freeform-deposition have regular width and height and can finally be deposited for 3D parts with high quality but over-deposition with irregular profile leading to inferior quality should be avoided. Thus, prediction for width and height in pressed-deposition and freeform-deposition is meaningful for DIW quality evaluation and control. To verify the prediction accuracy of profile dimension for the proposed numerical model, experimental results of width and height under different process parameters setting are measured and listed in Table 4.3 and Table 4.4 where the symbol + represented over-deposition status. Correspondingly, the simulated width and height are listed in Table 4.5 and

Table 4.6. The relative errors between experimental and the simulated width and height are calculated using the data from Table 4.3 to

Table 4.6 and listed in Table 4.7 and Table 4.8.

Table 4.3 Experimental width under different process parameters (width unit: mm)

H^*	0.3		0.6		0.9		1.2		1.5	
V^*	V_e/(mm/s)		V_e/(mm/s)		V_e/(mm/s)		V_e/(mm/s)		V_e/(mm/s)	
	6	9	6	9	6	9	6	9	6	9
1.2	+	+	1.00±0.04	1.07±0.06	0.81±0.03	0.79±0.03	0.80±0.05	0.77±0.03	0.79±0.03	0.77±0.03
0.8	+	+	+	+	1.10±0.02	1.06±0.04	0.97±0.03	0.95±0.04	0.97±0.03	0.95±0.03
0.4	+	+	+	+	+	+	+	+	1.43±0.05	1.35±0.04

Table 4.4 Experimental height under different process parameters (height unit: mm)

H^*	0.3		0.6		0.9		1.2		1.5	
V^*	V_e/(mm/s)		V_e/(mm/s)		V_e/(mm/s)		V_e/(mm/s)		V_e/(mm/s)	
	6	9	6	9	6	9	6	9	6	9
1.2	+	+	0.5±0.01	0.5±0.02	0.75±0.01	0.75±0.01	0.80±0.05	0.77±0.01	0.79±0.03	0.77±0.01
0.8	+	+	+	+	0.75±0.01	0.75±0.01	0.97±0.03	0.95±0.04	0.97±0.03	0.95±0.03
0.4	+	+	+	+	+	+	+	+	1.25±0.02	1.25±0.01

Table 4.5 Simulated width under different process parameters (width unit: mm)

H^*	0.3		0.6		0.9		1.2		1.5	
V^*	V_e/(mm/s)		V_e/(mm/s)		V_e/(mm/s)		V_e/(mm/s)		V_e/(mm/s)	
	6	9	6	9	6	9	6	9	6	9
1.2	+	+	1.00	1.00	0.89	0.87	0.81	0.80	0.81	0.80
0.8	+	+	+	+	1.10	1.10	0.94	0.92	0.97	0.94

0.4	+	+	+	+	+	+	+	+	1.35	1.30

Table 4.6 Simulated height under different process parameters (height unit: mm)

H^*	0.3		0.6		0.9		1.2		1.5	
V^*	V_e/(mm/s)		V_e/(mm/s)		V_e/(mm/s)		V_e/(mm/s)		V_e/(mm/s)	
	6	9	6	9	6	9	6	9	6	9
1.2	+	+	0.50	0.50	0.73	0.71	0.78	0.78	0.78	0.76
0.8	+	+	+	+	0.74	0.74	0.93	0.93	0.90	0.88
0.4	+	+	+	+	+	+	+	+	1.25	1.23

Table 4.7 Relative error of experimental and simulated width under different process parameters

H^*	0.3		0.6		0.9		1.2		1.5	
V^*	V_e/(mm/s)		V_e/(mm/s)		V_e/(mm/s)		V_e/(mm/s)		V_e/(mm/s)	
	6	9	6	9	6	9	6	9	6	9
1.2	+	+	0	6.54%	9.88%	10.13%	1.25%	3.90%	2.53%	4.00%
0.8	+	+	+	+	0	3.77%	4.44%	3.16%	0	1.05%
0.4	+	+	+	+	+	+	+	+	5.59%	3.70%

Table 4.8 Relative error of experimental and simulated height under different process parameters

H^*	0.3		0.6		0.9		1.2		1.5	
V^*	V_e/(mm/s)		V_e/(mm/s)		V_e/(mm/s)		V_e/(mm/s)		V_e/(mm/s)	
	6	9	6	9	6	9	6	9	6	9
1.2	+	+	0	0	2.67%	5.33%	2.50%	1.30%	1.27%	1.30%
0.8	+	+	+	+	1.33%	1.33%	4.12%	2.10%	7.22%	7.37%
0.4	+	+	+	+	+	+	+	+	0	1.60%

The accuracy of the numerical prediction for profile dimension is verified as the maximum relative errors of width and height between the experimental and simulated results are 10.13% and 7.37% respectively, which are significantly improved as compared with the values of 20% and 28% reported in the literature [175]. As shown in Figure 4.13, the numerical perdition accuracy for profile dimension varies with the process parameters setting and the maximum

relative error appears at the edge of the printable window. The maximum relative error of width appears at the edge of the V^* setting (H^*=0.9, V^*=1.2) and the maximum relative error of height appears at the edge of the H^* setting (H^*=1.5, V^*=0.8). In these cases, relatively large prediction errors for the profile dimension would generate.

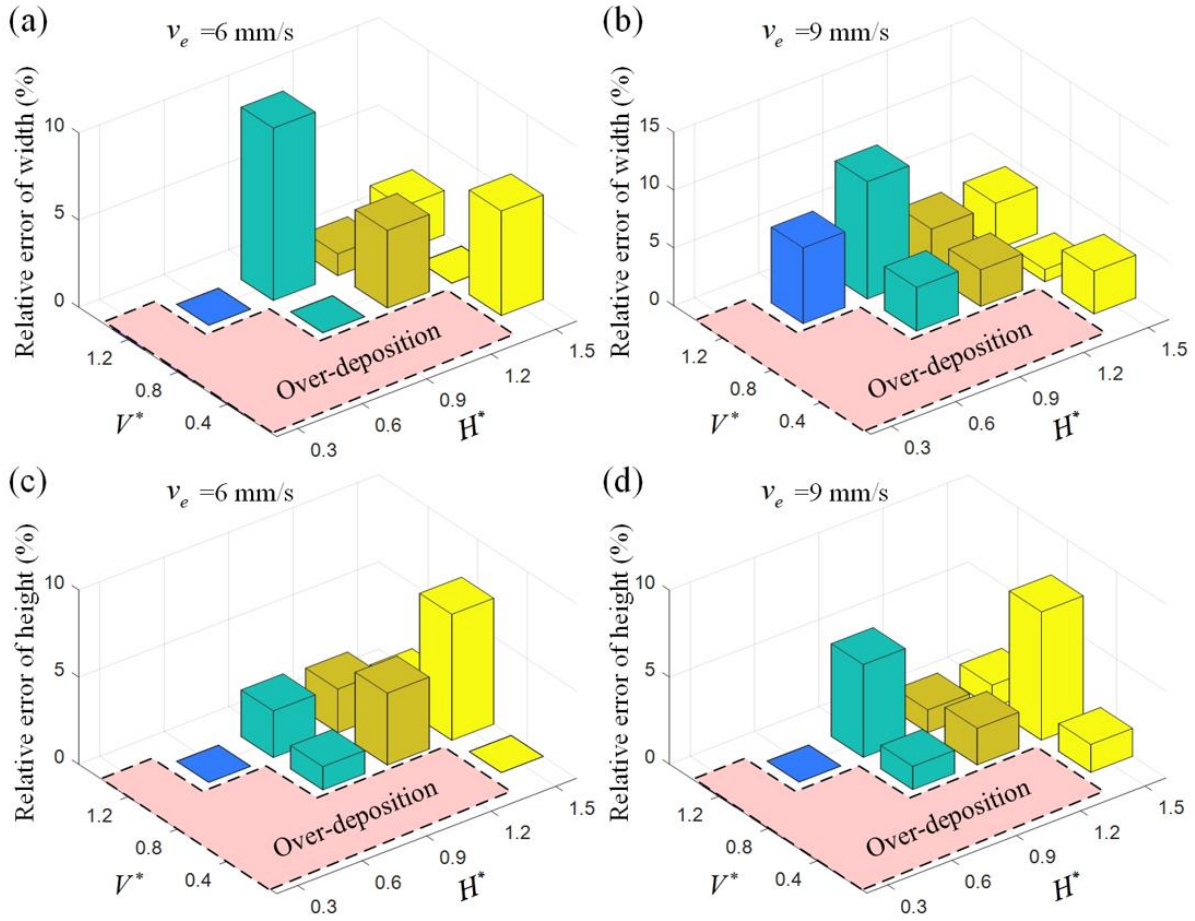

Figure 4.13 Relative error of the experimental and simulated profile dimension under different process parameters for: (a) width when v_e is set as 6 mm/s; (b) width when v_e is set as 9 mm/s; (c) height when v_e is set as 6 mm/s; (d) height when v_e is set as 9 mm/s

4.4.3 Process analysis

After the experimental validation for the numerical prediction of the deposited filaments, the effects of process parameters on deposited filaments are investigated based on the use of the numerical model. Figure 4.11, Figure 4.12, and Table 4.3 to

Table 4.6 show that the deposition statuses and profile dimension are influenced by V^* and H^* while v_e has no impact when V^* and H^* are fixed when v_e is set in printable window. The reason for this phenomenon is that v_n and v_e have the same multiple change when the

value of V^* is fixed ($V^* = v_n / v_e$) which causes the effect of changes in v_e to be offset by the synchronous changes in v_n.

The combination of V^* and H^* influence the deposition status and profile dimension. In order to investigate the effect of V^* and H^* individually, one process parameter is set as a constant value while the other changes. As shown in Figure 4.14, to investigate the effect of V^* individually, H^* is set as 1.5 while V^* changes from 0 to 1.2. As shown in Figure 4.15, to investigate the effect of H^* individually, V^* is set as 1.2 while H^* changes from 0 to 1.5. The deposition status starts from over-deposition to pressed-deposition and finally to freeform-deposition when V^* and H^* increase as shown in Figure 4.14 and Figure 4.15. The effect of V^* on width and height is influenced by its deposition status and is summarized as: width decreases with V^* in pressed-deposition and freeform-deposition; height remains the same with V^* in pressed-deposition while decreases with V^* in freeform-deposition. The effect of H^* on width and height is influenced by its deposition status and is summarized as: width decreases with H^* in pressed-deposition while remains the same with H^* in freeform-deposition; height increases with H^* in pressed-deposition while remains the same with H^* in freeform-deposition.

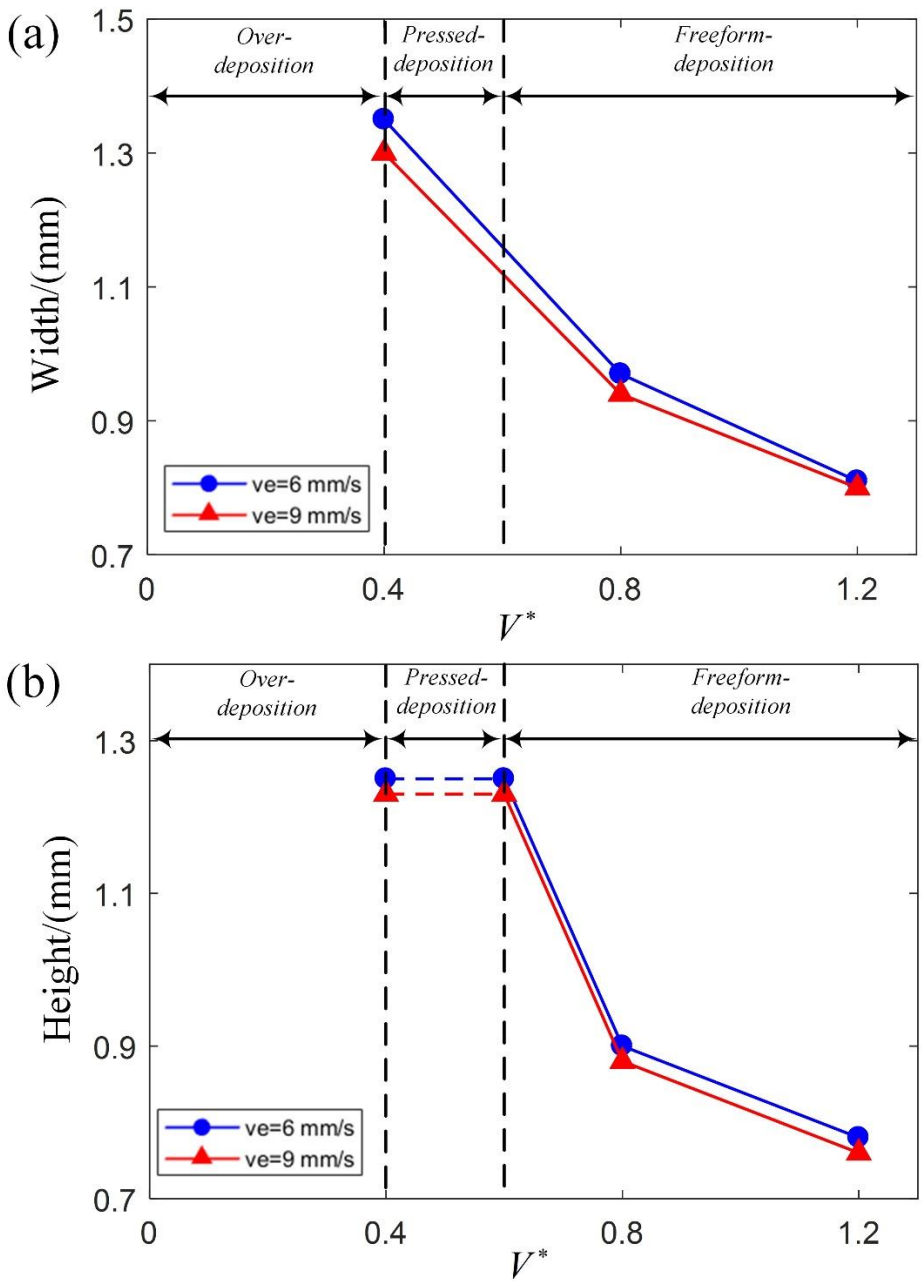

Figure 4.14 Effect of V^* on width and height when H^* is set as a constant value (H^* is set as 1.5 in the two charts): (a) width; (b) height

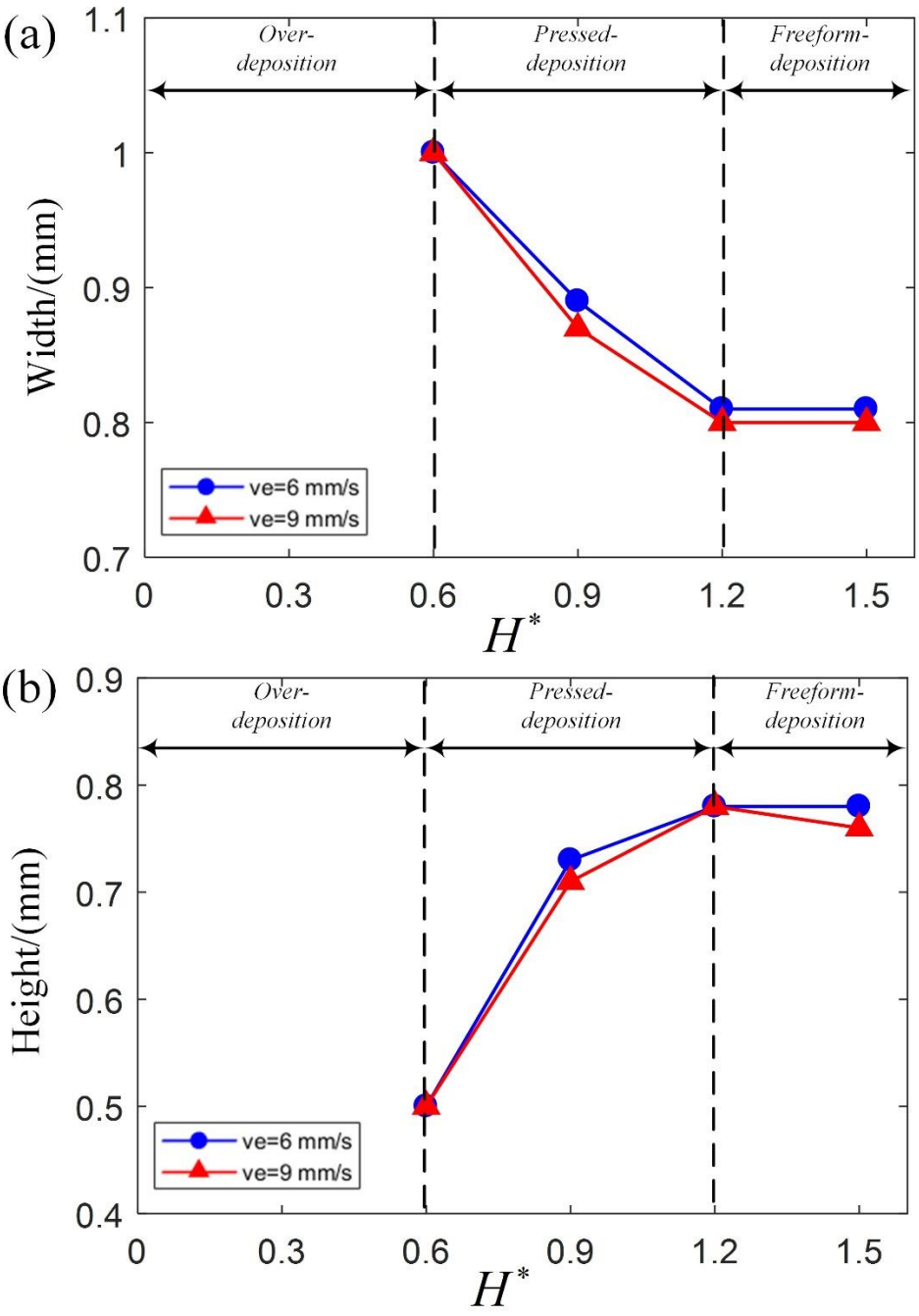

Figure 4.15 Effect of H^* on width and height when v^* is set as a constant value (v^* is set as 1.2 in the two charts): (a) width; (b) height

4.5 Numerical simulation of deposited corners

4.5.1 Numerical Modeling

The OpenFOAM v1912 is used to realize the numerical simulation of the 3D profile of deposited corners as plotted in Figure 4.16. In the numerical simulation, OpenFOAM v1912 is used to build geometrical model, generate meshes, determine boundary conditions and solve

governing equations. After numerical simulation in OpenFOAM v1912, ParaView is used to build visualizations and analyze simulation data.

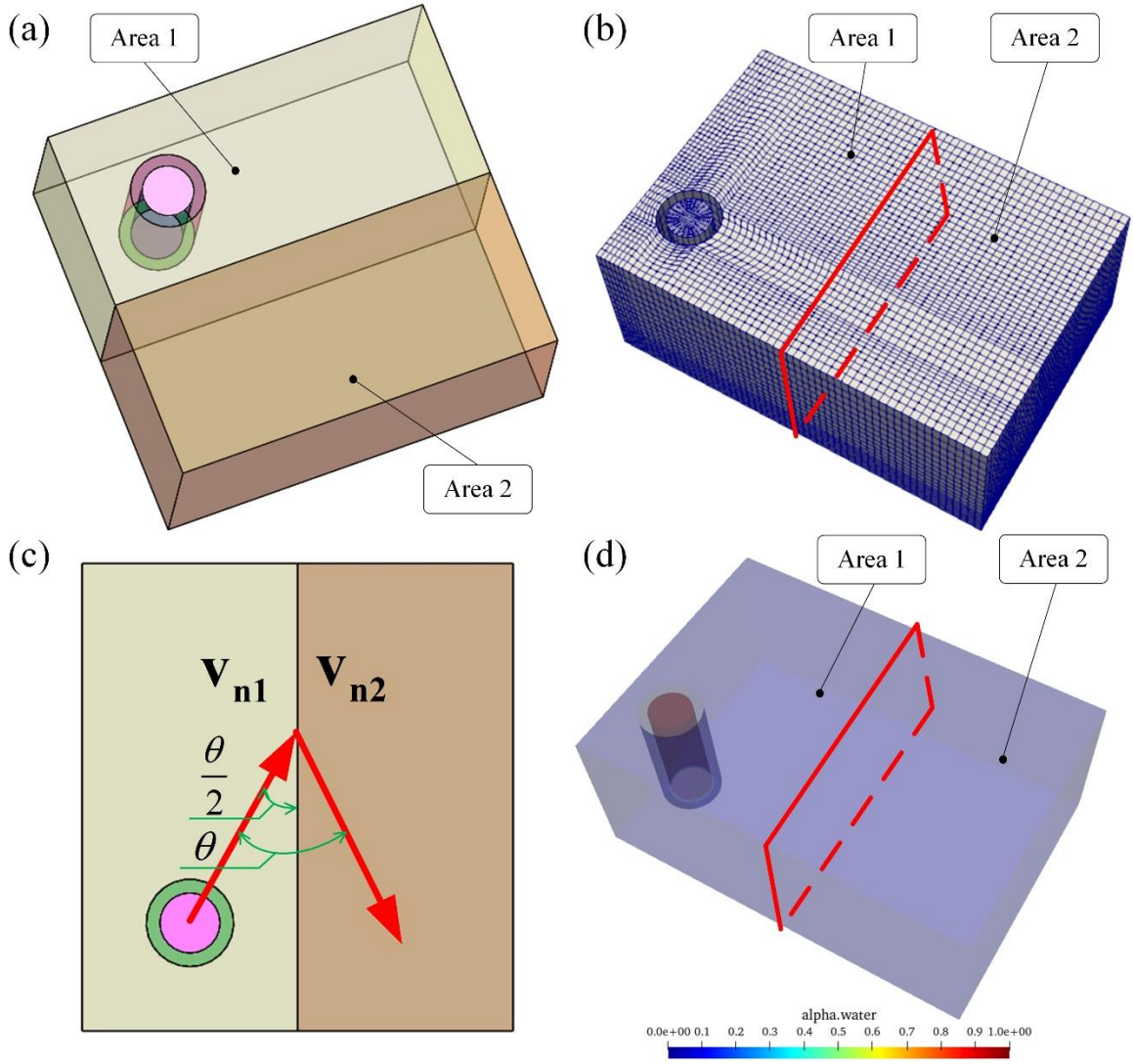

Figure 4.16 Numerical modeling of 3D profile of deposited corners: (a) 3D geometrical model; (b) generated meshes; (c) velocity condition in substrates; (d) initial condition of phase fraction

(1) Geometrical model

The route of modeling of deposited corners of any angle in the proposed numerical simulation is to construct two computing areas, and simulate the corner of any angle by applying velocities of the same magnitude and different directions with the corner angle as the velocity direction angle to the substrates of the two computing areas. As shown in Figure 4.16 (a), the geometrical model consists of two areas named as area 1 and area 2 where joint surface 1 in area 1 (Figure 4.17 (a)) and joint surface 2 in area 2 (Figure 4.18 (a)) are merged to combine area 1 and area 2 into a complete model. As shown in Figure 4.17 (a), in area 1, the boundary

surfaces include inlet, nozzle inner wall, nozzle outer wall, nozzle bottom wall, air, joint surface 1 and substrate 1. As illustrated in Figure 4.17 (b), the critical parameters of area 1 include the inner diameter of nozzle d_n, the outer diameter of nozzle D_n, the average velocity of ink in nozzle v_e, the nozzle length L_n, and the distance between nozzle bottom and substrate h. v_e is calculated using Eq. (4.11) based on the conservation of mass.

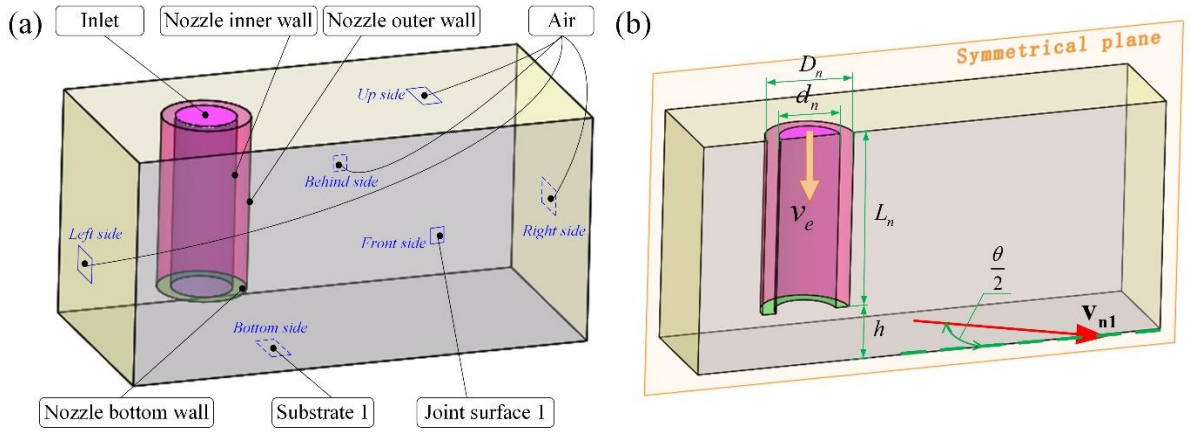

Figure 4.17 Illustration of 3D geometrical model of area 1 in model of DF: (a) boundary surfaces; (b) critical parameters

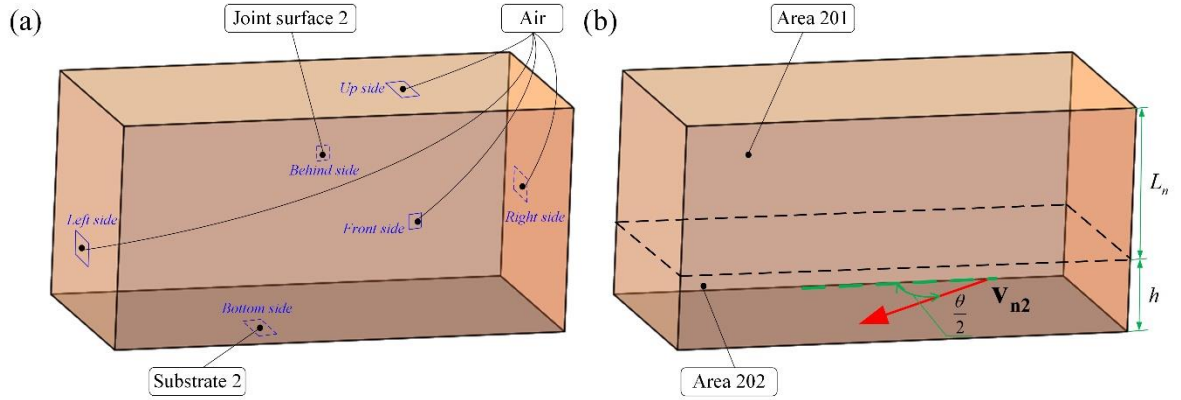

Figure 4.18 Illustration of 3D geometrical model of area 2 in model of DF: (a) boundary surfaces; (b) critical parameters

As shown in Figure 4.18 (a), in area 2, the boundary surfaces include air, joint surface 2 and substrate 2. As illustrated in Figure 4.18 (b), the critical parameters of area 2 include the h and the L_n. Area 2 is divided into area 201 and area 202 according to the values of L_n and h along the height direction as shown in Figure 4.18 (b), where the area with the height of h from substrate 2 is area 202 and the rest is area 201.

(2) Generated meshes

As shown in Figure 4.16 (b), meshes are generated as cuboid grids with arc edges in the areas related to circular nozzle and as cuboid grids with all straight edges in the areas outside

the circular nozzle to realize a smooth and precise interface simulation between ink and air. As illustrated in Figure 4.19, to improve calculation efficiency and accuracy, meshes are refined in the region of deposited filaments including inner nozzle and area between nozzle bottom and substrate in area 1 (Figure 4.19 (a)) and area 201 in area 2 (Figure 4.19 (b)).

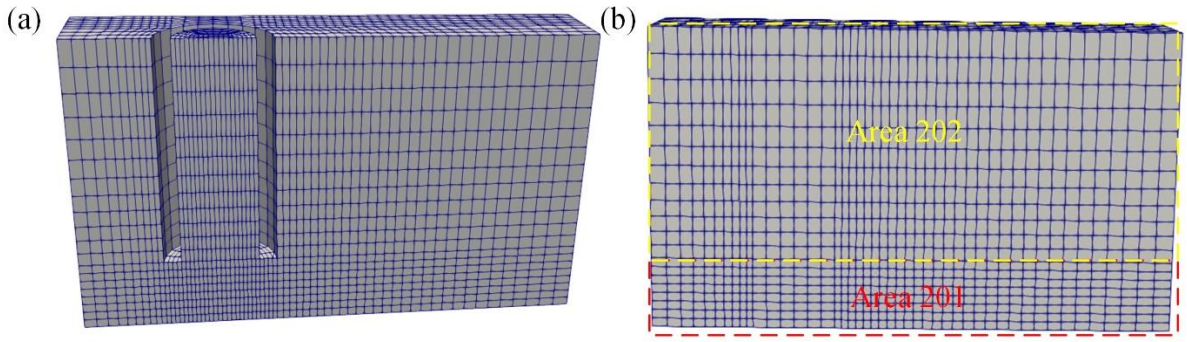

Figure 4.19 Illustration of generated meshes in: (a) area 1; (b) area 2

(3) Boundary conditions

Velocity boundary conditions include the average velocity of ink in nozzle v_e on inlet, the nozzle velocity $\mathbf{v_{n1}}$ on substrate 1 and the nozzle velocity $\mathbf{v_{n2}}$ on substrate 2. As illustrated in Figure 4.16 (c), to avoid the model becoming a complex dynamic-mesh model which needs a large amount of computational time, the position of nozzle is fixed in the model while the substrate 1 is applied with a velocity $\mathbf{v_{n1}}$ and the substrate 2 is applied with a velocity $\mathbf{v_{n2}}$ in the boundary setting respectively as the movements of the nozzle and substrates are relative to each other. The values of $\mathbf{v_{n1}}$ and $\mathbf{v_{n2}}$ are same. The angle of $\mathbf{v_{n1}}$ and $\mathbf{v_{n2}}$ models the angle of deposited corners with the value of θ. The boundary conditions for the numerical simulation is summarized as in Table 4.9.

Table 4.9 Boundary conditions for the numerical simulation of deposited corners

Name and physical meaning	Type	Setting
Inlet	Inlet	Velocity is set as v_e
Nozzle inner wall; nozzle outer wall; nozzle bottom wall	No-slip boundary	No-slip
Air	InletOutlet boundary	Depended on dynamic calculation
Substrate 1	No-slip boundary	Velocity is set as $\mathbf{v_{n1}}$
Substrate 2	No-slip boundary	Velocity is set as $\mathbf{v_{n2}}$

Figure 4.16 (d) presents the condition of phase fraction at the initial time which means the nozzle is filled with ink at the initial time, where red regime represents the ink and blue regime represents the air.

4.5.2 Experimental verification

(1) Experimental setup

In order to validate the proposed numerical simulation of deposited corners, the selected ink Nivea Crème is used in corner deposition experiments. The corner deposition experiments are setup same as Figure 4.9 using the piston driven DIW 3D printer TM-081 (Tobeca Company, France). To fully show the proposed simulation of deposited corners has the ability to simulate corners of any angle, the value of θ is set from 30 ° to 150 ° with the interval of 15 °. Before printing, the substrate is leveled using the method proposed in [189] to reduce the influence of substrate levelness on printed filaments and corners. After printing, a ruler is put aside the deposited corner, and a camera Logitech 720p (Logitech, Swiss) which is installed on the printer is used to take photos of deposited corners with the ruler. The camera is calibrated using asymmetric circular grid pattern [110] to reduce the influence of lens distortion on measurements.

The photos are processed using the software Matlab to obtain the outline of deposited corners in real dimensions. In the image processing of experimental photos, the photo is transferred to grayscale and outline of deposited corner is obtained based on the use of canny edge detection; then outline in pixel coordinate is transferred into outline in real world coordinate by comparing the dimension of a pixel and the real dimension shown in ruler. Finally, the simulated and experimental outlines in real world coordinate are compared and the maximum distance deviation between simulated and experimental outlines (MDDSEO) of deposited corners is obtained in the software Matlab. The MDDSEO is used as the quantitative indicator to analyze the effectiveness of the simulation. All corner deposition experiments are repeated three times to reduce experimental random error. The MDDSEO of each corner angle is presented as the mean ± standard deviation. Statistical analysis is performed using one-way analysis of variance (ANOVA) where statistical significance is defined as $p^* < 0.05$.

(2) Parameters setting

Parameters in numerical simulations of deposited corners include parameters of material properties, critical parameters of geometrical model and process parameters. Parameters of material properties of the selected ink are obtained experimentally in Section 3.2.3 and are

listed in Table 3.1. For critical parameters of geometrical model, the values of d_n, D_n and D_p are set as 0.84 mm, 1.22 mm, and 21.6 mm, which match the actual dimensions of the used DIW 3D printer in the experimental verification, respectively. As the nozzle length has no effect on v_e and the final deposited filaments and corners, the value of L_n is set as 2.44 mm which is smaller than practice nozzle length (18 mm) to reduce computational time.

Deposition status and the profile dimension of the deposited filaments are influenced by process parameters including v_e, h and the value of $\mathbf{v_{n1}}$ and $\mathbf{v_{n2}}$ [125, 188]. Based on the results of Section 3.3, process parameters are selected as: v_e =6 mm/s; h =0.75 mm; the value of $\mathbf{v_{n1}}$ and $\mathbf{v_{n2}}$ is 4.8 mm/s. As shown in Figure 4.20, DF under this process parameters combination has a stable and regular 3D shape and cross-sectional profile using the numerical simulation of DF proposed in Section 4.4. Finally, to model deposited corners of any angle, the value of θ is set from 30 ° to 150 ° with the interval of 15 ° in numerical simulations and experiments to validate the numerical simulation of deposited corners of any angle.

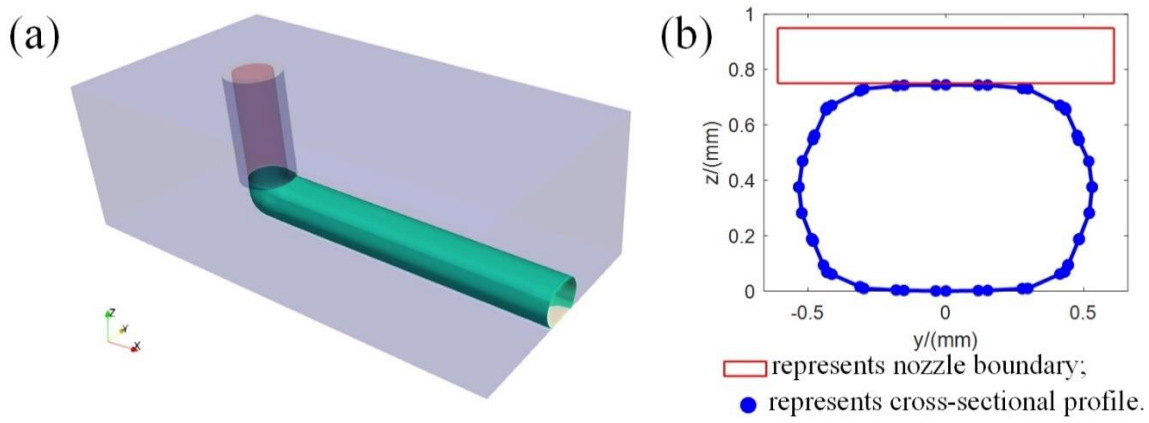

Figure 4.20 Simulated DF under the selected process parameters combination: (a) 3D profile; (b) cross-sectional profile

(3) Results

The simulation calculation times of corner when the value of θ is set from 30 ° to 150 ° are listed in .

Table 4.10 Simulation calculation time of corner under different corner angles

Corner angle	30°	60°	90°	120°	150°
Simulation time/mins	116	172	145	100	65

The 3D profile and top view of simulated deposited corners and top view of three-times experimental results for deposited corners where the value of θ is set from 30 ° to 150 ° with

the interval of 15 °are represented in Figure 4.21. Comparison of simulation and experimental results is conducted in the software Matlab using image processing and plotted in Figure 4.22. In Figure 4.22, the green area represents the simulation result of deposited filaments and corners; the grey area represents the substrate; the red, yellow and purple dashed lines represent experimental outlines of deposited corners in the first, second and third test, respectively; the blue solid line represents the MDDSEO of deposited corners.

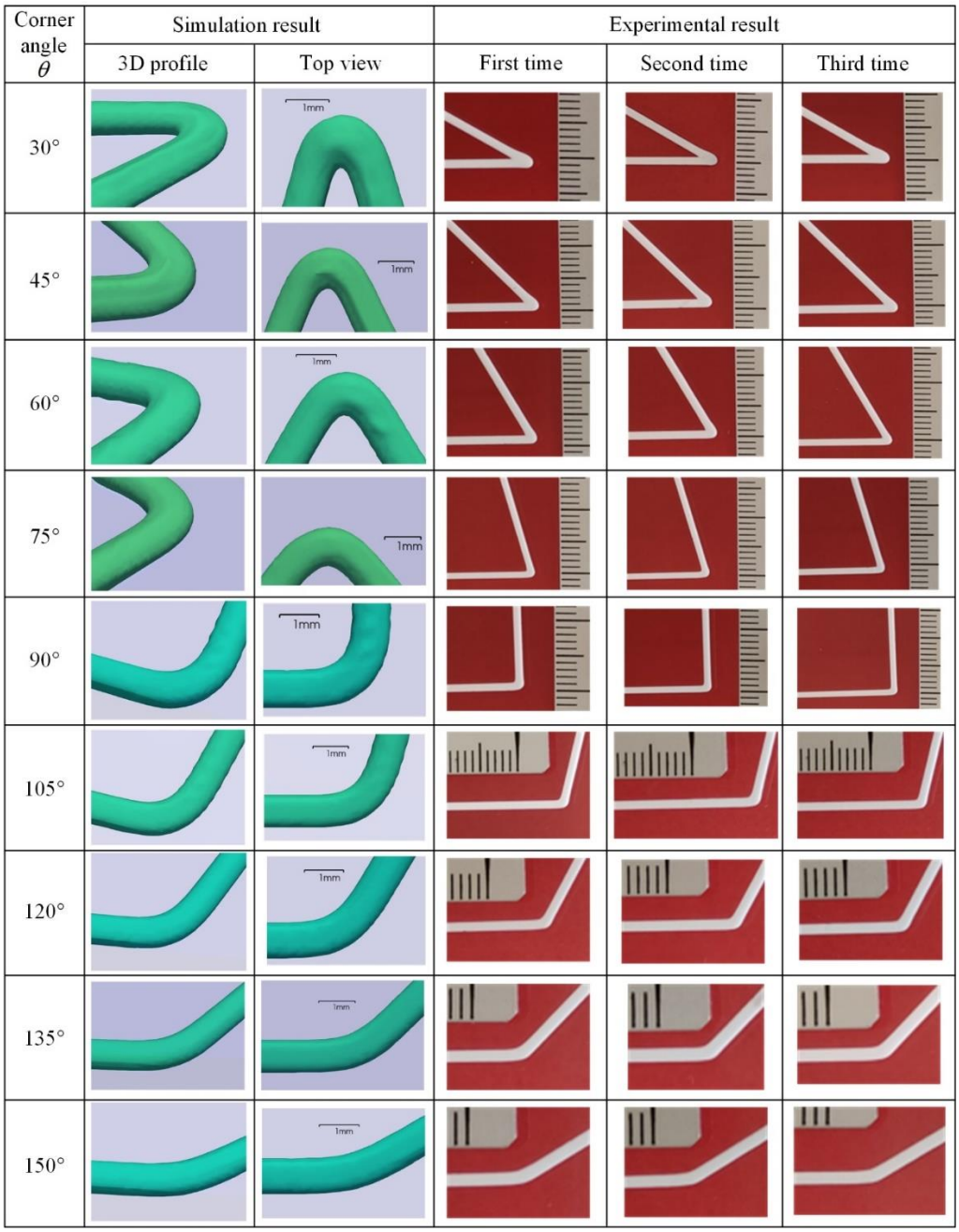

Figure 4.21 Simulation and experimental results of deposited corners where the value of corner angle is set from 30 °to 150 °with the interval of 15 °

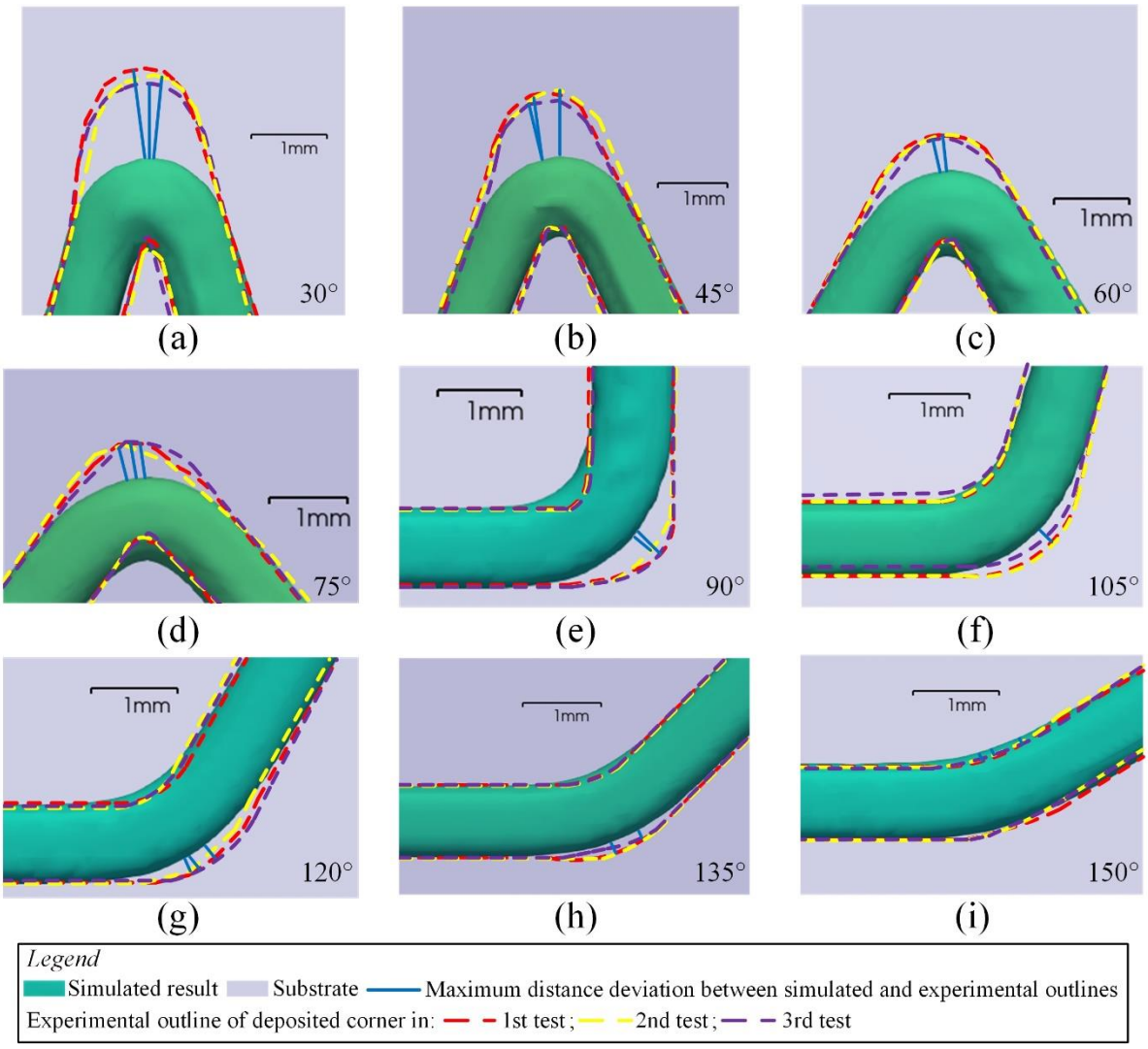

Figure 4.22 Comparison of simulation and experimental results of deposited corners when is set as: (a) 30 °; (b) 45 °; (c) 60 °; (d) 75 °; (e) 90 °; (f) 105 °; (g) 120 °; (h) 135 °; (i) 150 °

As shown in Figure 4.22, the simulation results of deposited straight filaments and the corner angles formed by two straight filaments fit experimental results well. For outlines of the deposited corners, the MDDSEO is used as indicator to illustrate the comparison between simulation and experimental results quantitatively. Based on the marked MDDSEO in Figure 4.22, MDDSEO of deposited corners under different corner angles are summarized in Table 4.11 and Figure 4.23. As shown in Table 4.11 and Figure 4.23, the maximum value and minimum value of MDDSEO is 1.06 ±0.06 mm and 0.09 ±0.01 mm when θ is set as 30 °and 150 °, respectively; and the MDDSEO decreases as θ increases. Thus, the proposed numerical simulation is validated as an effective method to model deposited corners of any angle as the simulated corner angles fit experimental angles well and the maximum value of MDDSEO is 1.06 ±0.06 mm.

Table 4.11 Maximum distance deviation between simulated and experimental outlines (MDDSEO) of deposited corners

Corner angle (°)	30	45	60	75	90	105	120	135	150
MDDSEO (mm)	1.06 ± 0.06	0.84 ± 0.04	0.45 ± 0.02	0.41 ± 0.02	0.33 ± 0.05	0.16 ± 0.01	0.14 ± 0.01	0.13 ± 0.01	0.09 ± 0.01

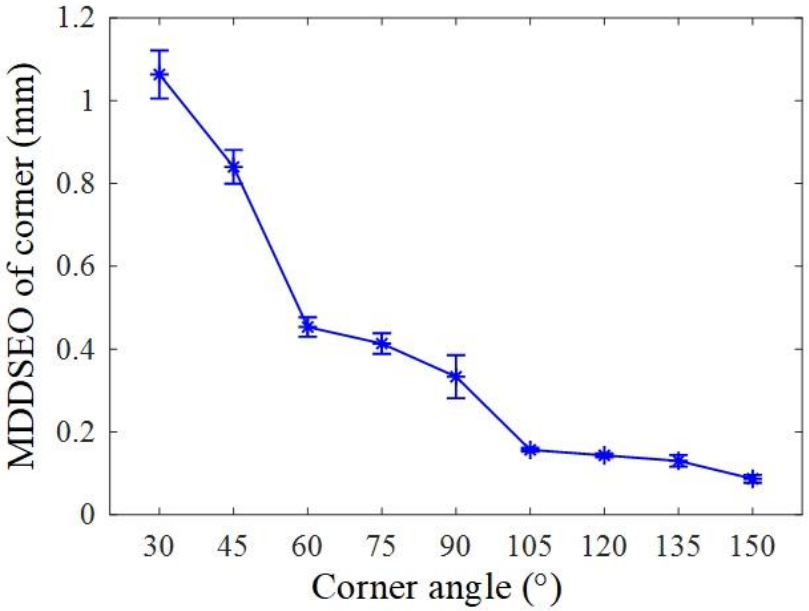

Figure 4.23 Maximum distance deviation between simulated and experimental outlines (MDDSEO) of deposited corners under different corner angles

However, the MDDSEO of corners is larger than MDDSEO of straight filaments where the maximum value of MDDSEO is 1.06 ± 0.06 mm for corners while the maximum value of MDDSEO is less than 0.20 mm for straight filaments, which means prediction accuracy of corners is inferior than that of straight filaments in the simulation. The reason for this phenomenon is due to the difference between the nozzle velocity applied on substrate in numerical simulation and real nozzle velocity in experiments only for the corner region. As shown in Figure 4.24 (a), the trajectory of nozzle velocity applied on substrate is from point A to point B and then from point B to point C. As illustrated in Figure 4.24 (b) and Figure 4.24 (c), in numerical simulation, the value of velocity on substrate along x axis is a constant v_{nx} along the trajectory, and the value of velocity on substrate along y axis can change from v_{ny} to $-v_{ny}$ at point B immediately. In practice experiments, the nozzle cannot change velocity immediately and need a uniform deceleration and uniform acceleration process to change nozzle velocity direction [190] and the acceleration depends on the firmware of the DIW 3D

printer [152]. As shown in Figure 4.25 (a), the trajectory of nozzle velocity applied on substrate is divided into 4 stages as follows where detail velocity profile along x axis and y axis is plotted in Figure 4.25 (b) and Figure 4.25 (c), respectively:

- Point A to point B_1: uniform velocity process;
- Point B_1 to point B_2: uniform deceleration process;
- Point B_2 to point B_3: uniform deceleration process;
- Point B_3 to point C: uniform velocity process.

Comparing Figure 4.24 and Figure 4.25, the difference of nozzle velocity between numerical simulation and real experiment leads to the simulation prediction error in corner regions. As shown in Figure 4.23, the MDDSEO of corners decreases as the corner angle increases which means that the effect of difference of nozzle velocity between numerical simulation and real experiment on deposited corners decreases as the corner angle increases.

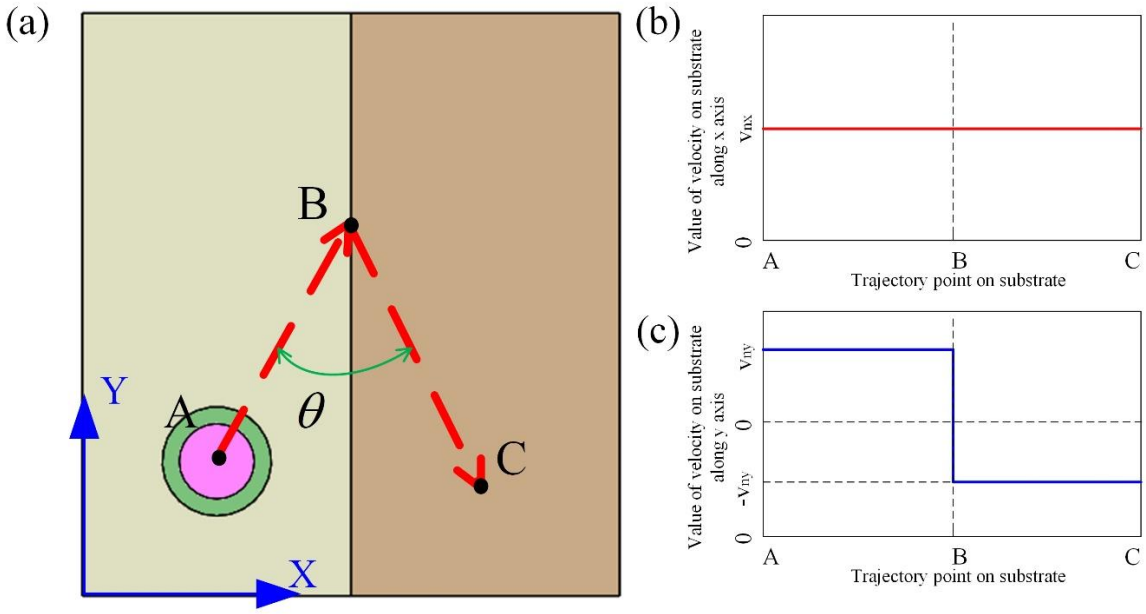

Figure 4.24 Velocity profile on substrate in numerical simulation and design of G-code: (a) trajectory; (b) value of velocity on substrate along x axis; (c) value of velocity on substrate along y axis

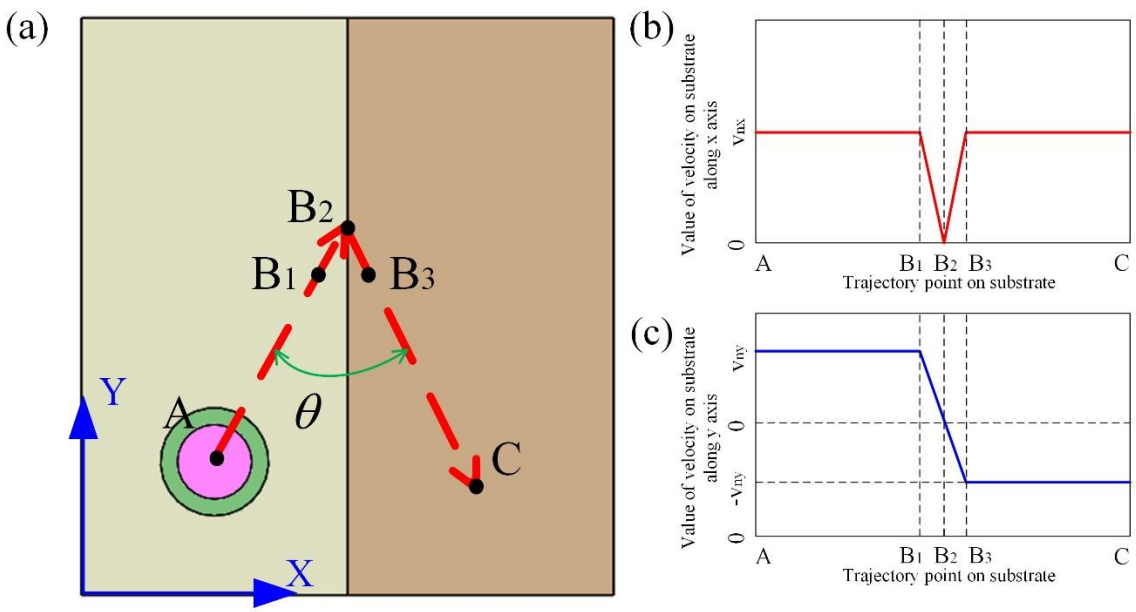

Figure 4.25 Velocity profile on substrate in actual corner deposition experiments: (a) trajectory; (b) value of velocity on substrate along x axis; (c) value of velocity on substrate along y axis

4.6 Conclusion

In this chapter, numerical simulations of the most basic elements in DIW including FEF, DF and deposited corner are proposed and experimental verifications are conducted to verify the proposed numerical simulations. Based on the proposed numerical simulations, process analyses of DIW are conducted.

For numerical simulation of FEF, a numerical model of FEF is established with numerical simulation method and then the FEF is evaluated based on this model. Two evaluation indicators, mean diameter and stability, are proposed to evaluate the FEF. The selected ink Nivea Crème is used to verify the method. The established numerical model of FEF is verified as the shape in simulation is in accordance with experimental results and the diameter prediction accuracy is better than 0.08 mm. After experimental verification, the model and evaluation indicators are used to deal with the two questions in process analysis for FEF in DIW as follows:

(1) Analyze effect of the piston velocity on FEF: there is a minimum piston velocity, 2 mm/s for Nivea Crème for setting of v_e, to produce continuous and stable FEF; mean diameters of FEF decrease with increasing piston velocity. Stability decreases firstly and then increases as piston velocity increases;

(2) Find suitable printable windows for process parameters: printable window of setting of v_e is 5 mm/s-15 mm/s for Nivea Crème.

For numerical simulation of DF, the detailed influence of process parameters on the deposition status and profile dimension has not been fully quantitatively characterized in the previous numerical prediction works for the DF of direct ink writing. In this chapter, the effect of process parameters on the deposition status and profile dimension has been quantified based on numerical prediction. An improved 3D numerical model is established by using VOF method and by considering the overall ink material properties. The improved 3D numerical model overcomes the problem of previous simplified 2D models in predicting cross-section and the shortcoming of previous 3D numerical models in ignoring important material properties such as surface tension coefficient and static contact angle which limit the prediction accuracy. Critical process parameters are identified as the dimensionless nozzle velocity and the dimensionless height.

Based on the numerical prediction, the deposition status is characterized into three types named over-deposition, pressed-deposition and freeform-deposition and the profile dimension under each deposition status is predicted. The effectiveness of the numerical prediction for the deposited filaments is validated as the simulated deposited statues dividing results are consistent with the experimental results and are also consistent with the idealized results. The prediction accuracy of the numerical prediction for the profile dimension is verified as the maximum relative errors of width and height between experimental and simulated results are 10.13% and 7.37% respectively which are significantly improved as compared with the reported values of 20% and 28% in the literature. The maximum relative error of the numerical prediction for the profile dimension appears at the edge of the printable window.

Based on the numerical prediction, the effects of the process parameters on DF are also investigated. The deposition status starts from over-deposition to pressed-deposition and finally to freeform-deposition when V^* and H^* increase while average the velocity of ink in nozzle has no significant effect on the deposition status and profile dimension. The deposition status should be taken into consideration for the effect of process parameters on the profile dimension: the width decreases with V^* in pressed-deposition and freeform-deposition; the height remains the same with V^* in pressed-deposition while decreases with V^* in freeform-deposition; the width decreases with H^* in pressed-deposition while remains the same with H^* in freeform-deposition; the height increases with H^* in pressed-deposition while remains the same with H^* in freeform-deposition.

The proposed numerical simulation and process analysis for DF characterize the deposition status and study the profile dimension in each deposition status based on the use of numerical prediction. The numerical simulation of DF suggests a material-saving and effective numerical prediction for the deposition status and profile dimension of the DF and the investigation of the effects of process parameters in DIW. It also provides a viable basis for the future work on the elaboration of numerical modeling of the overall DIW 3D printing process.

For numerical simulation of deposited corners, the previous research works for numerical simulation of deposited corners could only achieve the corner simulation under the condition of small angle and failed to realize corner simulation of any angle. In this chapter, an improved 3D numerical simulation of deposited corners is established by using VOF method and by considering the overall ink material properties. The improved 3D numerical simulation overcomes the limitation of the previous work and realizes deposited corner modeling of any angle by constructing two calculation areas where two nozzle velocities with the corner angle are applied on the substrates of two calculation areas. The effectiveness of the proposed numerical model is validated through corners deposition experiments using the selected ink in a DIW 3D printer as the simulated corner angles fit experimental angles well and the maximum value of MDDSEO is 1.06 ± 0.06 mm. It is observed that the simulation accuracy in corners is inferior than that in filaments. The reason for this phenomenon is due to the difference between the nozzle velocity applied on substrate in numerical simulation and real nozzle velocity in experiments only for the corner region as the nozzle needs a uniform deceleration and uniform acceleration process to change nozzle velocity direction in practice printing. The MDDSEO of deposited corners decreases as the corner angle increases.

The numerical simulations of FEF, DF and deposited corners provides an effective numerical simulation for the modeling outputs in DIW.It could be used in DIW process analyses work including the printability evaluation of new prepared inks, the process parameters optimization and the establishment of digital twin. They also provide a viable basis for the future work on the elaboration of numerical modeling of the overall DIW 3D printing process.

Chapter 5: Conclusion and perspectives

5.1 Conclusion

The process understanding and analysis of DIW have not been fully studied, which limits the manufacturing accuracy and application promotion of this technique. To solve this problem, it is of critical to do research on process analysis for DIW to fully understand this process and improve the usability of DIW. Numerical simulation is one of the most powerful tools in process analysis in AM. Process analysis based on numerical simulations has advantages in saving material/trial time and easily capturing critical process parameters value which are difficult obtained by experimental measurements. The research on process modeling and analysis of DIW based on numerical simulations will provide important support for the development and guidance of DIW. However, there is currently few systematic work on process modeling and analysis based on numerical simulations for DIW. To bridge this gap, this thesis proposes a process modeling and analysis for DIW based on numerical simulations.

In chapter 2, a systematic literature review of DIW is conducted firstly to summarize features, development, challenges and solutions for challenges of DIW and an insufficiently solved problem - difficulty to quickly find suitable process parameters for the prepared ink - is determined as the research question of this thesis. To solve the research question, process modeling and analysis for DIW is selected as the solution. Afterwards, a literature review of process modeling and analysis for DIW is conducted. Inputs and outputs of process modeling are summarized and numerical process modeling methods are selected as the most suitable method for process modelling and analysis of DIW. However, there is currently few systematic work on process modeling and analysis based on numerical simulations for DIW. Based on the review, the objective of this thesis is determined as: to propose a process modeling and analysis for DIW based on numerical simulations.

In chapter 3, the ink Nivea Crème and a piston-driven DIW 3D printer are chosen to verify the proposed numerical simulations. Before numerical simulation, ink material properties are characterized and optimal process parameters setting is selected to provide the basis for modeling inputs. For ink material properties characterization, density, surface tension, static

contact angle and rheology properties are obtained for the used ink. For process parameters selection, the DIW process parameters are identified through process analyses and a two-step method is proposed to optimize DIW process parameters for dimensional accuracy and analyze the significance of each process parameter. Experimental verifications verify the proposed process parameters selection method and the method robustness on other shapes; parameter adaptability in 3D parts printing from printed layers' analyses for the proposed method and parameter adaptability in constructs fabricated as 100% infill or with porosities.

In chapter 4, numerical simulations of the most basic elements in DIW including FEF, DF and deposited corner are proposed and experimental verifications are conducted to verify the proposed numerical simulations. Based on the proposed numerical simulations, process analyses of DIW are conducted.

For numerical simulation of FEF, the established numerical model of FEF is verified as the shape in simulation is in accordance with experimental results and the diameter prediction accuracy is better than 0.08 mm. Process analysis based on the numerical simulation of FEF shows that: 1) there is a minimum piston velocity, 2 mm/s for Nivea Crème for setting of v_e, to produce continuous and stable FEF; 2) mean diameters of FEF decrease with increasing piston velocity and stability decreases firstly and then increases as piston velocity increases; 3) suitable printable windows for setting of v_e is 5 mm/s-15 mm/s for Nivea Crème.

For numerical simulation of DF, the effect of process parameters on the deposition status and profile dimension has been quantified based on numerical prediction of DF. An improved 3D numerical model is established by using VOF method and by considering the overall ink material properties. The improved 3D numerical model overcomes the problem of previous simplified 2D models in predicting cross-section and the shortcoming of previous 3D numerical models in ignoring important material properties such as surface tension coefficient and static contact angle which limit the prediction accuracy. Critical process parameters are identified as the dimensionless nozzle velocity and the dimensionless height. Based on the numerical prediction, the deposition status is characterized into three types named over-deposition, pressed-deposition and freeform-deposition and the profile dimension under each deposition status is predicted. The effectiveness of the numerical prediction for the DF is validated as the simulated deposited statues dividing results are consistent with the experimental results and are also consistent with the idealized results.

The prediction accuracy of the numerical prediction for the profile dimension is verified as the maximum relative errors of width and height between experimental and simulated results

are 10.13% and 7.37% respectively which are significantly improved as compared with the reported values of 20% and 28% in the literature. The maximum relative error of the numerical prediction for the profile dimension appears at the edge of the printable window. Based on the numerical prediction, the effects of the process parameters on DF are also investigated. The deposition status starts from over-deposition to pressed-deposition and finally to freeform-deposition when V^* and H^* increase while average the velocity of ink in nozzle has no significant effect on the deposition status and profile dimension. The deposition status should be taken into consideration for the effect of process parameters on the profile dimension: the width decreases with V^* in pressed-deposition and freeform-deposition; the height remains the same with V^* in pressed-deposition while decreases with V^* in freeform-deposition; the width decreases with H^* in pressed-deposition while remains the same with H^* in freeform-deposition; the height increases with H^* in pressed-deposition while remains the same with H^* in freeform-deposition.

For numerical simulation of deposited corners, the previous research works for numerical simulation of deposited corners could only achieve the corner simulation under the condition of small angle and failed to realize corner simulation of any angle. An improved 3D numerical simulation of deposited corners is established by using VOF method and by considering the overall ink material properties. The improved 3D numerical simulation overcomes the limitation of the previous work and realizes deposited corner modeling of any angle by constructing two calculation areas where two nozzle velocities with the corner angle are applied on the substrates of two calculation areas. The effectiveness of the proposed numerical model is validated through corners deposition experiments using the selected ink in a DIW 3D printer as the simulated corner angles fit experimental angles well and the maximum value of MDDSEO is 1.06 ± 0.06 mm. It is observed that the simulation accuracy in corners is inferior than that in filaments and the MDDSEO of deposited corners decreases as the corner angle increases.

In conclusion, this thesis determines the research objective through systematic literature reviews and realize the objective by ink material property characterization, process parameters selection, numerical simulations, experimental verification and process analysis. This thesis suggests an effective numerical simulation for the modeling outputs in DIW which could be used in DIW process analyses work including the printability evaluation of new prepared inks, the process parameters optimization and the establishment of digital twin, which is helpful for the process understanding and analysis of DIW.

5.2 Perspectives

Following the works presented in Chapter 1-4, many other perspectives can be envisaged. Among those I hope to follow are:

For process parameters selection, there is a limitation in quantitative analysis of printed objects (parts) and the thesis does not obtain a quantitative relationship between input and output based on experimental method. Future work will conduct a quantitative evaluation for printed objects using computer vision method and a quantitative relationship between input and output will be proposed based on the quantitative data using response surface methodology.

For numerical simulations of DIW, the thesis does not establish numerical simulations of printed layers and 3D parts. Future work will establish numerical simulations of printed layers and 3D parts to realize modeling of all outputs for DIW including FEF, DF, deposited corners, printed layers and 3D parts.

For process analysis of DIW, the thesis does not fully analyze the process in the printability evaluation of new prepared inks, the process parameters optimization and the establishment of digital twin. Future work will conduct a complete process analyses work including the printability evaluation of new prepared inks, the process parameters optimization and the establishment of digital twin, which is helpful for the process understanding and analysis of DIW.

Non-planar substrates and the use of multi-axis robots are important direction for DIW owing to their ability to build more complex geometries. Future work will study the non-planar substrates and the use of multi-axis robots.

References

[1] W.E. Frazier, Metal Additive Manufacturing: A Review, Journal of Materials Engineering and Performance 23(6) (2014) 1917-1928.

[2] H. Bikas, P. Stavropoulos, G. Chryssolouris, Additive manufacturing methods and modelling approaches: a critical review, The International Journal of Advanced Manufacturing Technology 83(1) (2016) 389-405.

[3] X. Niu, S. Singh, A. Garg, H. Singh, B. Panda, X. Peng, Q. Zhang, Review of materials used in laser-aided additive manufacturing processes to produce metallic products, Frontiers of Mechanical Engineering 14(3) (2019) 282-298.

[4] A. Jiménez, P. Bidare, H. Hassanin, F. Tarlochan, S. Dimov, K. Essa, Powder-based laser hybrid additive manufacturing of metals: a review, The International Journal of Advanced Manufacturing Technology 114(1) (2021) 63-96.

[5] S.A. Rasaki, D. Xiong, S. Xiong, F. Su, M. Idrees, Z. Chen, Photopolymerization-based additive manufacturing of ceramics: A systematic review, Journal of Advanced Ceramics 10(3) (2021) 442-471.

[6] A. Indurkar, A. Pandit, R. Jain, P. Dandekar, Plant-based biomaterials in tissue engineering, Bioprinting 21 (2021) e00127.

[7] A. Kalkal, S. Kumar, P. Kumar, R. Pradhan, M. Willander, G. Packirisamy, S. Kumar, B.D. Malhotra, Recent advances in 3D printing technologies for wearable (bio)sensors, Additive Manufacturing 46 (2021) 102088.

[8] P. Kumar, D.K. Rajak, M. Abubakar, S.G.M. Ali, M. Hussain, 3D Printing Technology for Biomedical Practice: A Review, Journal of Materials Engineering and Performance (2021).

[9] A. Shahzad, I. Lazoglu, Direct ink writing (DIW) of structural and functional ceramics: Recent achievements and future challenges, Composites Part B: Engineering 225 (2021) 109249.

[10] C.D. Armstrong, L. Yue, Y. Deng, H.J. Qi, Enabling direct ink write edible 3D printing of food purees with cellulose nanocrystals, Journal of Food Engineering 330 (2022) 111086.

[11] Z.M. Jessop, A. Al-Sabah, N. Gao, S. Kyle, B. Thomas, N. Badiei, K. Hawkins, I.S. Whitaker, Printability of pulp derived crystal, fibril and blend nanocellulose-alginate bioinks for extrusion 3D bioprinting, Biofabrication 11(4) (2019) 045006.

[12] J.A. Lewis, Direct Ink Writing of 3D Functional Materials, Advanced Functional Materials 16(17) (2006) 2193-2204.

[13] M.A.S.R. Saadi, A. Maguire, N.T. Pottackal, M.S.H. Thakur, M.M. Ikram, A.J. Hart, P.M. Ajayan, M.M. Rahman, Direct Ink Writing: A 3D Printing Technology for Diverse Materials, Advanced Materials 34(28) (2022) 2108855.

[14] Y. Tu, A. Hassan, J.A. Arrieta-Escobar, U. Khaleeq uz Zaman, F. xue, s. Ali, G. Yang, Predictive modeling of extruded filament in the air for bioink in direct ink writing using numerical simulation, Procedia CIRP 112 (2022) 394-399.

[15] H. Ji, J. Zhao, J. Chen, S. Shimai, J. Zhang, Y. Liu, D. Liu, S. Wang, A novel experimental approach to quantitatively evaluate the printability of inks in 3D printing using two criteria, Additive Manufacturing 55 (2022) 102846.

[16] S. Lamnini, F. Baino, G. Montalbano, H. Javed, F. Smeacetto, Printability of carboxymethyl cellulose/glass-containing inks for robocasting deposition in reversible solid oxide cell applications, Materials Letters 318 (2022) 132239.

[17] V.K. Vorobiov, M.P. Sokolova, N.V. Bobrova, V.Y. Elokhovsky, M.A. Smirnov, Rheological properties and 3D-printability of cellulose nanocrystals/deep eutectic solvent electroactive ion gels, Carbohydrate Polymers 290 (2022) 119475.

[18] N. Guo, M.C. Leu, Additive manufacturing: technology, applications and research needs, Frontiers of Mechanical Engineering 8(3) (2013) 215-243.

[19] R. Leal, F.M. Barreiros, L. Alves, F. Romeiro, J.C. Vasco, M. Santos, C. Marto, Additive manufacturing tooling for the automotive industry, The International Journal of Advanced Manufacturing Technology 92(5) (2017) 1671-1676.

[20] N. Saengchairat, T. Tran, C.-K. Chua, A review: additive manufacturing for active electronic components, Virtual and Physical Prototyping 12(1) (2017) 31-46.

[21] A. Gisario, M. Kazarian, F. Martina, M. Mehrpouya, Metal additive manufacturing in the commercial aviation industry: A review, Journal of Manufacturing Systems 53 (2019) 124-149.

[22] S.A. Rasaki, C. Liu, C. Lao, H. Zhang, Z. Chen, The innovative contribution of additive manufacturing towards revolutionizing fuel cell fabrication for clean energy generation: A comprehensive review, Renewable and Sustainable Energy Reviews 148 (2021) 111369.

[23] E. Rezvani Ghomi, F. Khosravi, R.E. Neisiany, S. Singh, S. Ramakrishna, Future of additive manufacturing in healthcare, Current Opinion in Biomedical Engineering 17 (2021) 100255.

[24] R.P. Chaudhary, C. Parameswaran, M. Idrees, A.S. Rasaki, C. Liu, Z. Chen, P. Colombo, Additive manufacturing of polymer-derived ceramics: Materials, technologies, properties and potential applications, Progress in Materials Science 128 (2022) 100969.

[25] A. Mostafaei, A.M. Elliott, J.E. Barnes, F. Li, W. Tan, C.L. Cramer, P. Nandwana, M. Chmielus, Binder jet 3D printing—Process parameters, materials, properties, modeling, and challenges, Progress in Materials Science 119 (2021) 100707.

[26] B. Utela, D. Storti, R. Anderson, M. Ganter, A review of process development steps for new material systems in three dimensional printing (3DP), Journal of Manufacturing Processes 10(2) (2008) 96-104.

[27] W. Zhang, R. Melcher, N. Travitzky, R.K. Bordia, P. Greil, Three-Dimensional Printing of Complex-Shaped Alumina/Glass Composites, Advanced Engineering Materials 11(12) (2009) 1039-1043.

[28] D. Ke, S. Bose, Effects of pore distribution and chemistry on physical, mechanical, and biological properties of tricalcium phosphate scaffolds by binder-jet 3D printing, Additive Manufacturing 22 (2018) 111-117.

[29] A. Zocca, H. Elsayed, E. Bernardo, C.M. Gomes, M.A. Lopez-Heredia, C. Knabe, P. Colombo, J. Günster, 3D-printed silicate porous bioceramics using a non-sacrificial preceramic polymer binder, Biofabrication 7(2) (2015) 025008.

[30] H. Zhong, X.H. Yao, Y. Zhu, J. Zhang, D. Jiang, J.G. Chen, Z. Chen, X.J. Liu, Z. Huang, Preparation of SiC Ceramics by Laminated Object Manufacturing and Pressureless Sintering, 2015.

[31] B. Dermeik, N. Travitzky, Laminated Object Manufacturing of Ceramic-Based Materials, Advanced Engineering Materials 22(9) (2020) 2000256.

[32] S.C. Altıparmak, V.A. Yardley, Z. Shi, J. Lin, Extrusion-based additive manufacturing technologies: State of the art and future perspectives, Journal of Manufacturing Processes 83 (2022) 607-636.

[33] X. Wang, M. Jiang, Z. Zhou, J. Gou, D. Hui, 3D printing of polymer matrix composites: A review and prospective, Composites Part B: Engineering 110 (2017) 442-458.

[34] K. Sun, T.-S. Wei, B.Y. Ahn, J.Y. Seo, S.J. Dillon, J.A. Lewis, 3D Printing of Interdigitated Li-Ion Microbattery Architectures, Advanced Materials 25(33) (2013) 4539-4543.

[35] K. Zub, S. Hoeppener, U.S. Schubert, Inkjet Printing and 3D Printing Strategies for Biosensing, Analytical, and Diagnostic Applications, Advanced Materials 34(31) (2022) 2105015.

[36] Z. Chen, J. Ouyang, W. Liang, Z.-c. Yan, F. Stadler, C. Lao, Development and characterizations of novel aqueous-based LSCF suspensions for inkjet printing, Ceramics International 44(11) (2018) 13381-13388.

[37] Z. Zhu, Z. Gong, P. Qu, Z. Li, S.A. Rasaki, Z. Liu, P. Wang, C. Liu, C. Lao, Z. Chen, Additive manufacturing of thin electrolyte layers via inkjet printing of highly-stable ceramic inks, Journal of Advanced Ceramics 10(2) (2021) 279-290.

[38] A.-N. Chen, J.-M. Wu, K. Liu, J.-Y. Chen, H. Xiao, P. Chen, C.-H. Li, Y.-S. Shi, High-performance ceramic parts with complex shape prepared by selective laser sintering: a review, Advances in Applied Ceramics 117(2) (2018) 100-117.

[39] L.S. Santos, S.K. Gupta, H.A. Bruck, Simulation of buckling of internal features during selective laser sintering of metals, Additive Manufacturing 23 (2018) 235-245.

[40] M. Pelanconi, P. Colombo, A. Ortona, Additive manufacturing of silicon carbide by selective laser sintering of PA12 powders and polymer infiltration and pyrolysis, Journal of the European Ceramic Society 41(10) (2021) 5056-5065.

[41] K. Wang, R. Liu, H. Xu, High-strength and wave-transmitting Si3N4–Si2N2O-BN composites prepared using selective laser sintering, Ceramics International 48(14) (2022) 20126-20133.

[42] C.Y. Yap, C.K. Chua, Z.L. Dong, Z.H. Liu, D.Q. Zhang, L.E. Loh, S.L. Sing, Review of selective laser melting: Materials and applications, Applied Physics Reviews 2(4) (2015) 041101.

[43] F. Calignano, Design optimization of supports for overhanging structures in aluminum and titanium alloys by selective laser melting, Materials & Design 64 (2014) 203-213.

[44] L. Zhang, B. Song, J.J. Fu, S.S. Wei, L. Yang, C.Z. Yan, H. Li, L. Gao, Y.S. Shi, Topology-optimized lattice structures with simultaneously high stiffness and light weight fabricated by selective laser melting: Design, manufacturing and characterization, Journal of Manufacturing Processes 56 (2020) 1166-1177.

[45] Y. Xu, G. Huang, T. Li, Y. Tan, T. Bao, Compressive properties of Ti6Al4V Functionally Graded Lattice Structures via topology optimization design and selective laser melting fabrication, Materials Science and Engineering: A (2022) 144265.

[46] Z. Li, S. Sui, X. Ma, H. Tan, C. Zhong, G. Bi, A.T. Clare, A. Gasser, J. Chen, High deposition rate powder- and wire-based laser directed energy deposition of metallic materials: A review, International Journal of Machine Tools and Manufacture 181 (2022) 103942.

[47] M. Ansari, E. Jabari, E. Toyserkani, Opportunities and challenges in additive manufacturing of functionally graded metallic materials via powder-fed laser directed energy deposition: A review, Journal of Materials Processing Technology 294 (2021) 117117.

[48] H. Yi, Q. Wang, H. Cao, Wire-arc directed energy deposition of magnesium alloys: microstructure, properties and quality optimization strategies, Journal of Materials Research and Technology 20 (2022) 627-649.

[49] A. Pathania, S. Anand Kumar, B.K. Nagesha, S. Barad, T.N. Suresh, Reclamation of titanium alloy based aerospace parts using laser based metal deposition methodology, Materials Today: Proceedings 45 (2021) 4886-4892.

[50] J. Han, G. Zhang, X. Chen, Y. Cai, Z. Luo, X. Zhang, Y. Su, Y. Tian, High strength Ti alloy fabricated by directed energy deposition with in-situ Cu alloying, Journal of Materials Processing Technology 310 (2022) 117759.

[51] M. Chen, K. Yang, Z. Wang, S. Wang, E. Wu, Y. Lu, Z. Ni, J. Lu, G. Sun, Microstructure evolution and mechanical performance of NV E690 steel repaired by underwater laser directed energy deposition technique, Advanced Powder Materials (2022) 100095.

[52] A. Al Rashid, W. Ahmed, M.Y. Khalid, M. Koç, Vat photopolymerization of polymers and polymer composites: Processes and applications, Additive Manufacturing 47 (2021) 102279.

[53] S. Zakeri, M. Vippola, E. Levänen, A comprehensive review of the photopolymerization of ceramic resins used in stereolithography, Additive Manufacturing 35 (2020) 101177.

[54] D. Vallet, V. Pateloup, P. Michaud, T. Chartier, Development of a 3D model to predict curing dimensions and conversion rates of curable ceramic systems during stereolithography 3D printing process, Journal of the European Ceramic Society 42(13) (2022) 5851-5863.

[55] Q. Ge, B. Jian, H. Li, Shaping soft materials via digital light processing-based 3D printing: A review, Forces in Mechanics 6 (2022) 100074.

[56] Z. Wang, W. Yang, Y. Qin, W. Liang, H. Yu, L. Liu, Digital micro-mirror device -based light curing technology and its biological applications, Optics & Laser Technology 143 (2021) 107344.

[57] I.L. de Camargo, R. Erbereli, J.F.P. Lovo, R. Fortulan, C.A. Fortulan, Digital light processing additive manufacturing of in situ mullite-zirconia composites, Journal of the European Ceramic Society 42(13) (2022) 6025-6032.

[58] M. Sun, H. Cheng, P. Golvari, S.M. Kuebler, X. Yu, M. Zhang, Modeling of two-photon polymerization in the strong-pulse regime, Additive Manufacturing 60 (2022) 103241.

[59] A.K. Nguyen, R.J. Narayan, Two-photon polymerization for biological applications, Materials Today 20(6) (2017) 314-322.

[60] U. Staudinger, G. Zyla, B. Krause, A. Janke, D. Fischer, C. Esen, B. Voit, A. Ostendorf, Development of electrically conductive microstructures based on polymer/CNT nanocomposites via two-photon polymerization, Microelectronic Engineering 179 (2017) 48-55.

[61] K. Vanmol, S. Tuccio, V. Panapakkam, H. Thienpont, J. Watté, J. Van Erps, Two-photon direct laser writing of beam expansion tapers on single-mode optical fibers, Optics & Laser Technology 112 (2019) 292-298.

[62] M. Kim, J.-W. Choi, Rubber ink formulations with high solid content for direct-ink write process, Additive Manufacturing 44 (2021) 102023.

[63] D.F.D. Campos, M.A. Philip, S. Gürzing, C. Melcher, Y.Y. Lin, J. Schöneberg, A. Blaeser, B. Theek, H. Fischer, M. Betsch, Synchronized Dual Bioprinting of Bioinks and Biomaterial Inks as a Translational Strategy for Cartilage Tissue Engineering, 3D Printing and Additive Manufacturing 6(2) (2019) 63-71.

[64] C. Liu, Y. Qiu, Y. Liu, K. Xu, N. Zhao, C. Lao, J. Shen, Z. Chen, Novel 3D grid porous Li4Ti5O12 thick electrodes fabricated by 3D printing for high performance lithium-ion batteries, Journal of Advanced Ceramics 11(2) (2022) 295-307.

[65] T. Kim, C. Bao, M. Hausmann, G. Siqueira, T. Zimmermann, W.S. Kim, 3D Printed Disposable Wireless Ion Sensors with Biocompatible Cellulose Composites, Advanced Electronic Materials 5(2) (2019) 1800778.

[66] L.A. Vergara, H.A. Colorado, Additive manufacturing of Portland cement pastes with additions of kaolin, superplastificant and calcium carbonate, Construction and Building Materials 248 (2020) 118669.

[67] Z. Ye, C. Chu, D. Zhang, S. Ma, J. Guo, Y. Cheng, G. Xu, Z. Li, A. Sun, Study on 3D-Direct Ink Writing based on adding silica submicron-particles to improve the rheological properties of alumina ceramic ink, Materials Today Communications 28 (2021) 102534.

[68] M.C. Mulakkal, R.S. Trask, V.P. Ting, A.M. Seddon, Responsive cellulose-hydrogel composite ink for 4D printing, Materials & Design 160 (2018) 108-118.

[69] A. Shen, D. Caldwell, A.W.K. Ma, S. Dardona, Direct write fabrication of high-density parallel silver interconnects, Additive Manufacturing 22 (2018) 343-350.

[70] E. Guzi de Moraes, I.M. Ferreira, L.B. Teixeira, L.H. Cartapati, M.T. Souza, A.P. Novaes de Oliveira, Additive manufacturing of cellular structures from recycled soda-lime glass printing inks by robocasting, Ceramics International (2022).

[71] J. Cesarano, R. Segalman, P. Calvert, ROBOCASTING PROVIDES MOLDLESS FABRICATION FROM SLURRY DEPOSITION, Ceramic industry 148 (1998).

[72] J. Cesarano, P. Calvert, FREEFORMING OBJECTS WITH LOW BINDER SLURRY, United States, 2000.

[73] L. Sun, S.T. Parker, D. Syoji, X. Wang, J.A. Lewis, D.L. Kaplan, Direct-write assembly of 3D silk/hydroxyapatite scaffolds for bone co-cultures, Advanced healthcare materials 1(6) (2012) 729-735.

[74] J. Lessing, A.C. Glavan, S.B. Walker, C. Keplinger, J.A. Lewis, G.M. Whitesides, Inkjet Printing of Conductive Inks with High Lateral Resolution on Omniphobic “RF Paper” for Paper-Based Electronics and MEMS, Advanced Materials 26(27) (2014) 4677-4682.

[75] A. Frutiger, J.T. Muth, D.M. Vogt, Y. Mengüç, A. Campo, A.D. Valentine, C.J. Walsh, J.A. Lewis, Capacitive Soft Strain Sensors via Multicore–Shell Fiber Printing, Advanced Materials 27(15) (2015) 2440-2446.

[76] A. Sydney Gladman, E.A. Matsumoto, R.G. Nuzzo, L. Mahadevan, J.A. Lewis, Biomimetic 4D printing, Nature Materials 15(4) (2016) 413-418.

[77] M. Wehner, R.L. Truby, D.J. Fitzgerald, B. Mosadegh, G.M. Whitesides, J.A. Lewis, R.J. Wood, An integrated design and fabrication strategy for entirely soft, autonomous robots, Nature 536(7617) (2016) 451-455.

[78] N. Zhou, C. Liu, J.A. Lewis, D. Ham, Gigahertz Electromagnetic Structures via Direct Ink Writing for Radio-Frequency Oscillator and Transmitter Applications, Advanced Materials 29(15) (2017) 1605198.

[79] X.B. Chen, K. Jun, Modeling of positive-displacement fluid dispensing processes, IEEE Transactions on Electronics Packaging Manufacturing 27(3) (2004) 157-163.

[80] F. Wang, P. Mao, H. He, Dispensing of high concentration Ag nano-particles ink for ultra-low resistivity paper-based writing electronics, Scientific Reports 6(1) (2016) 21398.

[81] M. Rafiee, R.D. Farahani, D. Therriault, Multi-Material 3D and 4D Printing: A Survey, Advanced Science 7(12) (2020) 1902307.

[82] P.T. Smith, A. Basu, A. Saha, A. Nelson, Chemical modification and printability of shear-thinning hydrogel inks for direct-write 3D printing, Polymer 152 (2018) 42-50.

[83] G. Franchin, L. Wahl, P. Colombo, Direct ink writing of ceramic matrix composite structures, Journal of the American Ceramic Society 100(10) (2017) 4397-4401.

[84] C. Xu, C. An, Q. Li, S. Xu, S. Wang, H. Guo, J. Wang, Preparation and Performance of Pentaerythrite Tetranitrate-Based Composites by Direct Ink Writing, Propellants, Explosives, Pyrotechnics 43(11) (2018) 1149-1156.

[85] R. Tu, H.A. Sodano, Additive manufacturing of high-performance vinyl ester resin via direct ink writing with UV-thermal dual curing, Additive Manufacturing 46 (2021) 102180.

[86] J. Hinton Thomas, Q. Jallerat, N. Palchesko Rachelle, H. Park Joon, S. Grodzicki Martin, H.-J. Shue, H. Ramadan Mohamed, R. Hudson Andrew, W. Feinberg Adam, Three-dimensional printing of complex biological structures by freeform reversible embedding of suspended hydrogels, Science Advances 1(9) (2015) e1500758.

[87] F. Zhu, L. Cheng, J. Yin, Z.L. Wu, J. Qian, J. Fu, Q. Zheng, 3D Printing of Ultratough Polyion Complex Hydrogels, ACS Applied Materials & Interfaces 8(45) (2016) 31304-31310.

[88] L. Yang, X. Zeng, A. Ditta, B. Feng, L. Su, Y. Zhang, Preliminary 3D printing of large inclined-shaped alumina ceramic parts by direct ink writing, Journal of Advanced Ceramics 9(3) (2020) 312-319.

[89] X. Wu, T. Tu, Y. Dai, P. Tang, Y. Zhang, Z. Deng, L. Li, H.-B. Zhang, Z.-Z. Yu, Direct Ink Writing of Highly Conductive MXene Frames for Tunable Electromagnetic Interference Shielding and Electromagnetic Wave-Induced Thermochromism, Nano-Micro Letters 13(1) (2021) 148.

[90] A. Shahzad, S.A. Khan, A. Paksoy, Ö. Balcı-Çağıran, I. Lazoglu, Negative additive manufacturing of Al2O3-Al cermet material by fused deposition and Direct Ink Writing, Materials Today Communications 33 (2022) 104739.

[91] Y. Lakhdar, C. Tuck, J. Binner, A. Terry, R. Goodridge, Additive manufacturing of advanced ceramic materials, Progress in Materials Science 116 (2021) 100736.

[92] B.P. Croom, A. Abbott, J.W. Kemp, L. Rueschhoff, L. Smieska, A. Woll, S. Stoupin, H. Koerner, Mechanics of nozzle clogging during direct ink writing of fiber-reinforced composites, Additive Manufacturing 37 (2021) 101701.

[93] G. Siqueira, D. Kokkinis, R. Libanori, M.K. Hausmann, A.S. Gladman, A. Neels, P. Tingaut, T. Zimmermann, J.A. Lewis, A.R. Studart, Cellulose Nanocrystal Inks for 3D Printing of Textured Cellular Architectures, Advanced Functional Materials 27(12) (2017) 1604619.

[94] L. del-Mazo-Barbara, M.-P. Ginebra, Rheological characterisation of ceramic inks for 3D direct ink writing: a review, Journal of the European Ceramic Society (2021).

[95] B. Román-Manso, J. Muth, L.J. Gibson, W. Ruettinger, J.A. Lewis, Hierarchically Porous Ceramics via Direct Writing of Binary Colloidal Gel Foams, ACS Applied Materials & Interfaces 13(7) (2021) 8976-8984.

[96] B. Luo, H. Chen, Z. Zhu, B. Xie, C. Bian, Y. Wang, Printing single-walled carbon nanotube/Nafion composites by direct writing techniques, Materials & Design 155 (2018) 125-133.

[97] L. Ouyang, R. Yao, Y. Zhao, W. Sun, Effect of bioink properties on printability and cell viability for 3D bioplotting of embryonic stem cells, Biofabrication 8(3) (2016) 035020.

[98] N. Paxton, W. Smolan, T. Böck, F. Melchels, J. Groll, T. Jungst, Proposal to assess printability of bioinks for extrusion-based bioprinting and evaluation of rheological properties governing bioprintability, Biofabrication 9(4) (2017) 044107.

[99] J.L. Dávila, M.A. d'Ávila, Rheological evaluation of Laponite/alginate inks for 3D extrusion-based printing, The International Journal of Advanced Manufacturing Technology 101(1) (2019) 675-686.

[100] Y. He, F. Yang, H. Zhao, Q. Gao, B. Xia, J. Fu, Research on the printability of hydrogels in 3D bioprinting, Scientific Reports 6(1) (2016) 29977.

[101] S. Ma, S. Fu, S. Zhao, P. He, G. Ma, M. Wang, D. Jia, Y. Zhou, Direct ink writing of geopolymer with high spatial resolution and tunable mechanical properties, Additive Manufacturing 46 (2021) 102202.

[102] A. Kazemian, B. Khoshnevis, Real-time extrusion quality monitoring techniques for construction 3D printing, Construction and Building Materials 303 (2021) 124520.

[103] Y. Tu, A. Hassan, A. Siadat, G. Yang, Analytical modeling of deposited filaments for high viscosity material-based piston-driven direct ink writing, The International Journal of Advanced Manufacturing Technology (2022).

[104] T.J. Fleck, J.C.S. McCaw, S.F. Son, I.E. Gunduz, J.F. Rhoads, Characterizing the vibration-assisted printing of high viscosity clay material, Additive Manufacturing 47 (2021) 102256.

[105] B. Akhoundi, M. Nabipour, O. Kordi, F. Hajami, Calculating printing speed in order to correctly print PLA/continuous glass fiber composites via fused filament fabrication 3D printer, Journal of Thermoplastic Composite Materials (2021) 0892705721997534.

[106] H. Giberti, L. Sbaglia, M. Urgo, A path planning algorithm for industrial processes under velocity constraints with an application to additive manufacturing, Journal of Manufacturing Systems 43 (2017) 160-167.

[107] Y. Jin, J. Du, Z. Ma, A. Liu, Y. He, An optimization approach for path planning of high-quality and uniform additive manufacturing, The International Journal of Advanced Manufacturing Technology 92(1) (2017) 651-662.

[108] L. Li, R. McGuan, R. Isaac, P. Kavehpour, R. Candler, Improving precision of material extrusion 3D printing by in-situ monitoring & predicting 3D geometric deviation using conditional adversarial networks, Additive Manufacturing 38 (2021) 101695.

[109] Z. Jin, Z. Zhang, G.X. Gu, Autonomous in-situ correction of fused deposition modeling printers using computer vision and deep learning, Manufacturing Letters 22 (2019) 11-15.

[110] A.L. Petsiuk, J.M. Pearce, Open source computer vision-based layer-wise 3D printing analysis, Additive Manufacturing 36 (2020) 101473.

[111] H. Luan, Q. Huang, Prescriptive Modeling and Compensation of In-Plane Shape Deformation for 3-D Printed Freeform Products, IEEE Transactions on Automation Science and Engineering 14(1) (2017) 73-82.

[112] K. He, Q. Zhang, Y. Hong, Profile monitoring based quality control method for fused deposition modeling process, J. Intell. Manuf. 30(2) (2019) 947–958.

[113] M. Najjartabar Bisheh, S.I. Chang, S. Lei, A layer-by-layer quality monitoring framework for 3D printing, Computers & Industrial Engineering 157 (2021) 107314.

[114] G. Percoco, L. Arleo, G. Stano, F. Bottiglione, Analytical model to predict the extrusion force as a function of the layer height, in extrusion based 3D printing, Additive Manufacturing 38 (2021) 101791.

[115] N. Ashrafi, S. Nazarian, N.A. Meisel, J.P. Duarte, Experimental prediction of material deformation in large-scale additive manufacturing of concrete, Additive Manufacturing 37 (2021) 101656.

[116] N. Roussel, J. Spangenberg, J. Wallevik, R. Wolfs, Numerical simulations of concrete processing: From standard formative casting to additive manufacturing, Cement and Concrete Research 135 (2020) 106075.

[117] R. Attalla, C. Ling, P. Selvaganapathy, Fabrication and characterization of gels with integrated channels using 3D printing with microfluidic nozzle for tissue engineering applications, Biomedical Microdevices 18(1) (2016) 17.

[118] H. Li, S. Liu, L. Lin, Rheological study on 3D printability of alginate hydrogel and effect of graphene oxide, International Journal of Bioprinting; Vol 2, No 2 (2016)DO - 10.18063/IJB.2016.02.007 (2016).

[119] R. Suntornnond, E.Y. Tan, J. An, C.K. Chua, A Mathematical Model on the Resolution of Extrusion Bioprinting for the Development of New Bioinks, Materials 9(9) (2016).

[120] S. Kyle, Z.M. Jessop, A. Al-Sabah, I.S. Whitaker, 'Printability' of Candidate Biomaterials for Extrusion Based 3D Printing: State-of-the-Art, Advanced Healthcare Materials 6(16) (2017) 1700264.

[121] J.M. Lee, W.Y. Yeong, A preliminary model of time-pressure dispensing system for bioprinting based on printing and material parameters, Virtual and Physical Prototyping 10(1) (2015) 3-8.

[122] R. Suntornnond, E.Y.S. Tan, J. An, C.K. Chua, A Mathematical Model on the Resolution of Extrusion Bioprinting for the Development of New Bioinks, Materials (Basel) 9(9) (2016) 756.

[123] M. Vlasea, E. Toyserkani, Experimental characterization and numerical modeling of a micro-syringe deposition system for dispensing sacrificial photopolymers on particulate ceramic substrates, Journal of Materials Processing Technology 213(11) (2013) 1970-1977.

[124] N. Haghbin, D. Bone, K. Young, Controlled extrusion-based 3D printing of micro-channels with the geometric modelling of deposited roads, Journal of Manufacturing Processes 67 (2021) 406-417.

[125] M. Athanasiadis, A. Pak, D. Afanasenkau, I.R. Minev, Direct Writing of Elastic Fibers with Optical, Electrical, and Microfluidic Functionality, Advanced Materials Technologies 4(7) (2019) 1800659.

[126] G. Dong, G. Wijaya, Y. Tang, Y.F. Zhao, Optimizing process parameters of fused deposition modeling by Taguchi method for the fabrication of lattice structures, Additive Manufacturing 19 (2018) 62-72.

[127] H. Zhang, J.P. Choi, S.K. Moon, T.H. Ngo, A hybrid multi-objective optimization of aerosol jet printing process via response surface methodology, Additive Manufacturing 33 (2020) 101096.

[128] S. Yuan, J. Li, X. Yao, J. Zhu, X. Gu, T. Gao, Y. Xu, W. Zhang, Intelligent optimization system for powder bed fusion of processable thermoplastics, Additive Manufacturing 34 (2020) 101182.

[129] S. Mahmood, A.J. Qureshi, D. Talamona, Taguchi based process optimization for dimension and tolerance control for fused deposition modelling, Additive Manufacturing 21 (2018) 183-190.

[130] N.P. Kim, D. Cho, M. Zielewski, Optimization of 3D printing parameters of Screw Type Extrusion (STE) for ceramics using the Taguchi method, Ceramics International 45(2, Part A) (2019) 2351-2360.

[131] E.R. Fitzharris, I. Watt, D.W. Rosen, M.L. Shofner, Interlayer bonding improvement of material extrusion parts with polyphenylene sulfide using the Taguchi method, Additive Manufacturing 24 (2018) 287-297.

[132] A.a. Alafaghani, A. Qattawi, Investigating the effect of fused deposition modeling processing parameters using Taguchi design of experiment method, Journal of Manufacturing Processes 36 (2018) 164-174.

[133] O.A. Mohamed, S.H. Masood, J.L. Bhowmik, Process parameter optimization of viscoelastic properties of FDM manufactured parts using response surface methodology, Materials Today: Proceedings 4(8) (2017) 8250-8259.

[134] J. Seo, J.H. Kim, M. Lee, K. You, J. Moon, D.-H. Lee, U. Paik, Multi-objective optimization of tungsten CMP slurry for advanced semiconductor manufacturing using a response surface methodology, Materials & Design 117 (2017) 131-138.

[135] K.Y. Benyounis, Procedure of Conducting an Experiment Using Response Surface Methodology for Manufacturing Process Modelling and Optimization, Reference Module in Materials Science and Materials Engineering, Elsevier2019.

[136] G.D. Goh, S.L. Sing, W.Y. Yeong, A review on machine learning in 3D printing: applications, potential, and challenges, Artificial Intelligence Review 54(1) (2021) 63-94.

[137] S. Tong, D. Koller, Support vector machine active learning with applications to text classification, J. Mach. Learn. Res. 2 (2002) 45–66.

[138] C. Wang, X.P. Tan, S.B. Tor, C.S. Lim, Machine learning in additive manufacturing: State-of-the-art and perspectives, Additive Manufacturing 36 (2020) 101538.

[139] M. Weber, M. Welling, P. Perona, Unsupervised Learning of Models for Recognition, Computer Vision - ECCV 2000, Springer Berlin Heidelberg, Berlin, Heidelberg, 2000, pp. 18-32.

[140] S. Omar, M. Ngadi, H. Jebur, S. Benqdara, Machine Learning Techniques for Anomaly Detection: An Overview, International Journal of Computer Applications 79 (2013).

[141] T. Hristo, Unsupervised Learning of Social Networks from a Multiple-Source News Corpus, 2007.

[142] V. Figueiredo, F. Rodrigues, Z. Vale, J.B. Gouveia, An electric energy consumer characterization framework based on data mining techniques, IEEE Transactions on Power Systems 20(2) (2005) 596-602.

[143] F. Suarez, X. Zhou, Q.C. Pham, Can robots assemble an IKEA chair?, Science Robotics 3 (2018) eaat6385.

[144] J. Kim, J. Canny, Interpretable Learning for Self-Driving Cars by Visualizing Causal Attention, 2017.

[145] D. Silver, J. Schrittwieser, K. Simonyan, I. Antonoglou, A. Huang, A. Guez, T. Hubert, L. Baker, M. Lai, A. Bolton, Y. Chen, T. Lillicrap, F. Hui, L. Sifre, G. van den Driessche, T. Graepel, D. Hassabis, Mastering the game of Go without human knowledge, Nature 550(7676) (2017) 354-359.

[146] F. Liravi, R. Darleux, E. Toyserkani, Additive manufacturing of 3D structures with non-Newtonian highly viscous fluids: Finite element modeling and experimental validation, Additive Manufacturing 13 (2017) 113-123.

[147] J. Göhl, K. Markstedt, A. Mark, K. Håkansson, P. Gatenholm, F. Edelvik, Simulations of 3D bioprinting: predicting bioprintability of nanofibrillar inks, Biofabrication 10(3) (2018) 034105.

[148] S. Bakrani Balani, F. Chabert, V. Nassiet, A. Cantarel, Influence of printing parameters on the stability of deposited beads in fused filament fabrication of poly(lactic) acid, Additive Manufacturing 25 (2019) 112-121.

[149] Q. Liu, N. Zhang, W. Wei, X. Hu, Y. Tan, Y. Yu, Y. Deng, C. Bi, L. Zhang, H. Zhang, Assessing the dynamic extrusion-based 3D printing process for power-law fluid using numerical simulation, Journal of Food Engineering 275 (2020) 109861.

[150] R. Comminal, M.P. Serdeczny, D.B. Pedersen, J. Spangenberg, Numerical modeling of the strand deposition flow in extrusion-based additive manufacturing, Additive Manufacturing 20 (2018) 68-76.

[151] M.P. Serdeczny, R. Comminal, D.B. Pedersen, J. Spangenberg, Numerical simulations of the mesostructure formation in material extrusion additive manufacturing, Additive Manufacturing 28 (2019) 419-429.

[152] R. Comminal, M.P. Serdeczny, D.B. Pedersen, J. Spangenberg, Motion planning and numerical simulation of material deposition at corners in extrusion additive manufacturing, Additive Manufacturing 29 (2019) 100753.

[153] M.P. Serdeczny, R. Comminal, M.T. Mollah, D.B. Pedersen, J. Spangenberg, Numerical modeling of the polymer flow through the hot-end in filament-based material extrusion additive manufacturing, Additive Manufacturing 36 (2020) 101454.

[154] N. Scapin, P. Costa, L. Brandt, A volume-of-fluid method for interface-resolved simulations of phase-changing two-fluid flows, Journal of Computational Physics 407 (2020) 109251.

[155] M.R. Hashemi, P.B. Ryzhakov, R. Rossi, An enriched finite element/level-set method for simulating two-phase incompressible fluid flows with surface tension, Computer Methods in Applied Mechanics and Engineering 370 (2020) 113277.

[156] J. Yang, J. Kim, A phase-field method for two-phase fluid flow in arbitrary domains, Computers & Mathematics with Applications 79(6) (2020) 1857-1874.

[157] L. Zheng, S. Zheng, Q. Zhai, Reduction-consistent axisymmetric lattice Boltzmann equation method for N-phase fluids, Computers & Fluids 218 (2021) 104857.

[158] M. Li, I.A. Bolotnov, The evaporation and condensation model with interface tracking, International Journal of Heat and Mass Transfer 150 (2020) 119256.

[159] R. Comminal, W.R. Leal da Silva, T.J. Andersen, H. Stang, J. Spangenberg, Modelling of 3D concrete printing based on computational fluid dynamics, Cement and Concrete Research 138 (2020) 106256.

[160] Z. Liu, M. Li, Y.W.D. Tay, Y. Weng, T.N. Wong, M.J. Tan, Rotation nozzle and numerical simulation of mass distribution at corners in 3D cementitious material printing, Additive Manufacturing 34 (2020) 101190.

[161] M.H. Kim, Y.W. Lee, W.-K. Jung, J. Oh, S.Y. Nam, Enhanced rheological behaviors of alginate hydrogels with carrageenan for extrusion-based bioprinting, Journal of the Mechanical Behavior of Biomedical Materials 98 (2019) 187-194.

[162] F. Koch, K. Tröndle, G. Finkenzeller, R. Zengerle, S. Zimmermann, P. Koltay, Generic method of printing window adjustment for extrusion-based 3D-bioprinting to maintain high viability of mesenchymal stem cells in an alginate-gelatin hydrogel, Bioprinting 20 (2020) e00094.

[163] P. Meißner, H. Watschke, J. Winter, T. Vietor, Artificial Neural Networks-Based Material Parameter Identification for Numerical Simulations of Additively Manufactured Parts by Material Extrusion, Polymers 12(12) (2020).

[164] G. Papazetis, G.-C. Vosniakos, Mapping of deposition-stable and defect-free additive manufacturing via material extrusion from minimal experiments, The International Journal of Advanced Manufacturing Technology 100(9) (2019) 2207-2219.

[165] U.K.u. Zaman, E. Boesch, A. Siadat, M. Rivette, A.A. Baqai, Impact of fused deposition modeling (FDM) process parameters on strength of built parts using Taguchi's design of experiments, The International Journal of Advanced Manufacturing Technology 101(5) (2019) 1215-1226.

[166] F. Koch, K. Tröndle, G. Finkenzeller, R. Zengerle, S. Zimmermann, P. Koltay, Generic method of printing window adjustment for extrusion-based 3D-bioprinting to maintain high viability of mesenchymal stem cells in an alginate-gelatin hydrogel, Bioprinting (2020) e00094.

[167] F. Guo, X. Zhou, J. Liu, Y. Zhang, D. Li, H. Zhou, A reinforcement learning decision model for online process parameters optimization from offline data in injection molding, Applied Soft Computing 85 (2019) 105828.

[168] K. Chockalingam, N. Jawahar, K.N. Ramanathan, P.S. Banerjee, Optimization of stereolithography process parameters for part strength using design of experiments, The International Journal of Advanced Manufacturing Technology 29(1) (2006) 79-88.

[169] H.X. Li, Y. Li, B. Jiang, L. Zhang, X. Wu, J. Lin, Energy performance optimisation of building envelope retrofit through integrated orthogonal arrays with data envelopment analysis, Renewable Energy 149 (2020) 1414-1423.

[170] G. Senthilkumar, R. Ramakrishnan, A study of individual and interaction effect of process parameters on friction welded AISI 410 and AISI 430 joint, Materials Today: Proceedings (2020).

[171] N.-H. Kim, M.-H. Choi, S.-Y. Kim, E.-G. Chang, Design of experiment (DOE) method considering interaction effect of process parameters for optimization of copper chemical mechanical polishing (CMP) process, Microelectronic Engineering 83(3) (2006) 506-512.

[172] P. Sivaiah, D. Chakradhar, Modeling and optimization of sustainable manufacturing process in machining of 17-4 PH stainless steel, Measurement 134 (2019) 142-152.

[173] P. Geng, J. Zhao, Z. Gao, W. Wu, W. Ye, G. Li, H. Qu, Effects of Printing Parameters on the Mechanical Properties of High-Performance Polyphenylene Sulfide Three-Dimensional Printing, 3D Printing and Additive Manufacturing 8(1) (2020) 33-41.

[174] A. Schwab, R. Levato, M. D'Este, S. Piluso, D. Eglin, J. Malda, Printability and Shape Fidelity of Bioinks in 3D Bioprinting, Chemical Reviews 120(19) (2020) 11028-11055.

[175] M.P. Serdeczny, R. Comminal, D.B. Pedersen, J. Spangenberg, Experimental validation of a numerical model for the strand shape in material extrusion additive manufacturing, Additive Manufacturing 24 (2018) 145-153.

[176] A. Gosset, D. Barreiro-Villaverde, J.C. Becerra Permuy, M. Lema, A. Ares-Pernas, M.J. Abad López, Experimental and Numerical Investigation of the Extrusion and Deposition Process of a Poly(lactic Acid) Strand with Fused Deposition Modeling, Polymers 12(12) (2020).

[177] Y. Tu, A. Hassan, J.A. Arrieta-Escobar, U.K.u. Zaman, A. Siadat, G. Yang, Modeling and evaluation of freeform extruded filament based on numerical simulation method for direct ink writing, The International Journal of Advanced Manufacturing Technology 120(5) (2022) 3821-3829.

[178] H. Zong, Q. Cong, T. Zhang, Y. Hao, L. Xiao, G. Hao, G. Zhang, H. Guo, Y. Hu, W. Jiang, Simulation of printer nozzle for 3D printing TNT/HMX based melt-cast explosive, The International Journal of Advanced Manufacturing Technology 119(5) (2022) 3105-3117.

[179] M. Pantelidakis, K. Mykoniatis, J. Liu, G. Harris, A digital twin ecosystem for additive manufacturing using a real-time development platform, The International Journal of Advanced Manufacturing Technology 120(9) (2022) 6547-6563.

[180] F. Corradini, M. Silvestri, Design and testing of a digital twin for monitoring and quality assessment of material extrusion process, Additive Manufacturing 51 (2022) 102633.

[181] J. Lian, X. Yang, B. Ma, W. Gou, A novel method for bounding the phase fractions at both ends in Eulerian multi-fluid model, Computers & Fluids 243 (2022) 105512.

[182] M.R.P. de Sousa, H.S. Santana, O.P. Taranto, Modeling and simulation using OpenFOAM of biodiesel synthesis in structured microreactor, International Journal of Multiphase Flow 132 (2020) 103435.

[183] A. Ashish Saha, S.K. Mitra, Effect of dynamic contact angle in a volume of fluid (VOF) model for a microfluidic capillary flow, Journal of Colloid and Interface Science 339(2) (2009) 461-480.

[184] C. Busse, I. Tsivilskiy, J. Hildebrand, J.P. Bergmann, Numerical modeling of an inductively coupled plasma torch using OpenFOAM, Computers & Fluids 216 (2021) 104807.

[185] Q. Liu, J. Li, J. Liu, ParaView visualization of Abaqus output on the mechanical deformation of complex microstructures, Computers & Geosciences 99 (2017) 135-144.

[186] W. Ge, M.F. Modest, R. Marquez, Two-dimensional axisymmetric formulation of high order spherical harmonics methods for radiative heat transfer, Journal of Quantitative Spectroscopy and Radiative Transfer 156 (2015) 58-66.

[187] P. Geng, J. Zhao, W. Wu, W. Ye, Y. Wang, S. Wang, S. Zhang, Effects of extrusion speed and printing speed on the 3D printing stability of extruded PEEK filament, Journal of Manufacturing Processes 37 (2019) 266-273.

[188] H. Yuk, X. Zhao, A New 3D Printing Strategy by Harnessing Deformation, Instability, and Fracture of Viscoelastic Inks, Advanced Materials 30(6) (2018) 1704028.

[189] L. Zeng, X. Zou, 3D Printer Self-Adaptive Levelling Algorithm and Structure Design, 2019 4th International Conference on Mechanical, Control and Computer Engineering (ICMCCE), 2019, pp. 1054-10542.

[190] D.S. Ertay, A. Yuen, Y. Altintas, Synchronized material deposition rate control with path velocity on fused filament fabrication machines, Additive Manufacturing 19 (2018) 205-213.

Appendices

Appendix A Derivation for the relationship between R_w and W

As illustrated in Figure A1, the gravity of printed layer could be calculated as:

$$W = A_f \cdot \frac{Lx}{d_l} \cdot Lx \cdot Ly \cdot \rho \cdot g \tag{A. A1}$$

Where W is the weight of printed layer; A_f is the cross section area of filament on the substrate; Lx and Ly are designed dimension in x and y direction respectively; d_l is distance between lines; ρ is the material density; g is the gravity accelerate.

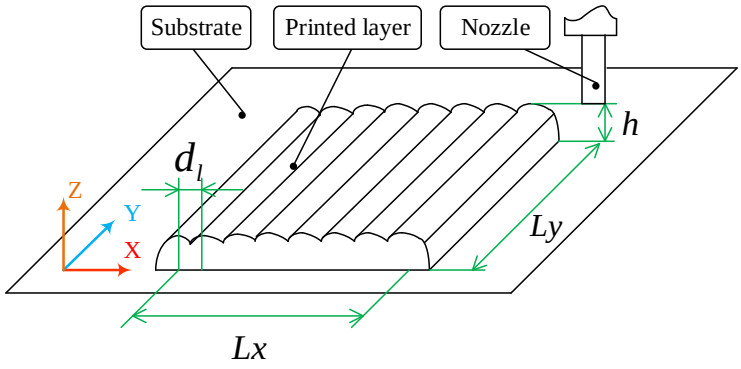

Figure A 1. Illustration of the relationship between R_w and W

Meanwhile,

$$\frac{1}{4}\pi D_p^{\ 2} \cdot v_p = A_f \cdot v_e \tag{A. A2}$$

$$v_p = \frac{1}{V^*} \cdot \frac{D_p^{\ 2}}{d_s^{\ 2}} \cdot v_n \tag{A. A3}$$

$$d_l = R_W \cdot \bar{w}_O \tag{A. A4}$$

Where all variables in Eq. (A. A2) -(A. A4) have been defined in Section 3.3.2.

Combining Eq. (A. A1) -(A. A4), the relationship between R_W and W is obtained as follows:

$$W = \frac{1}{4}\pi \frac{D_p^{\ 4}}{d_s^{\ 2}} \cdot (Lx)^2 \cdot Ly \cdot \rho \cdot g \cdot \frac{1}{\bar{w}_O \cdot R_w} \tag{A. A5}$$

Appendix B Detailed information for interaction effect tests

Two-factor interaction effects are considered. In interaction effect tests, one factor of v_n, V^* and H^* is fixed and the remaining two factor are changed to print lines. As listed in Table A 1, in interaction effect test for $v_n \times V^*$, H^* is fixed in 0.9; V^* is changed as 1, 0.8 and 0.6 for 5 mm/s and 11 mm/s of v_n. As listed in Table A 2, in interaction effect test for $v_n \times H^*$, V^* is fixed in 0.8; H^* is changed as 0.6, 0.9 and 1.2 for 5 mm/s and 11 mm/s of v_n. As listed in Table A 3, in interaction effect test for $V^* \times H^*$, v_n is fixed in 8 mm/s; H^* is changed as 0.6, 0.9 and 1.2 for 1 and 0.6 of V^*.

Table A 1 Process parameters setting of interaction effect test for $v_n \times V^*$

Experiment number	Process parameters setting		
	v_n /(mm/s)	V^*	H^*
S1-1	5	1	0.9
S1-2	5	0.8	0.9
S1-3	5	0.6	0.9
S2-1	11	1	0.9
S2-2	11	0.8	0.9
S2-3	11	0.6	0.9

Table A 2 Process parameters setting of interaction effect test for $v_n \times H^*$

Experiment number	Process parameters setting		
	v_n /(mm/s)	V^*	H^*
S3-1	5	0.8	0.6
S3-2	5	0.8	0.9
S3-3	5	0.8	1.2
S4-1	11	0.8	0.6
S4-2	11	0.8	0.9
S4-3	11	0.8	1.2

Table A 3 Process parameters setting of interaction effect test for $V^* \times H^*$

Experiment number	Process parameters setting		
	v_n /(mm/s)	V^*	H^*
S5-1	8	1	0.6
S5-2	8	1	0.9
S5-3	8	1	1.2
S6-1	8	0.6	0.6
S6-2	8	0.6	0.9
S6-3	8	0.6	1.2

Appendix C List of publications

Journal articles:

[1] **Yongqiang Tu**, Javier A. Arrieta-Escobar, Alaa Hassan, et al. Optimizing Process Parameters of Direct Ink Writing for Dimensional Accuracy of Printed Layers [J]. 3D Printing and Additive Manufacturing, 2021, published online. DOI: 10.1089/3dp.2021.0208

[2] **Yongqiang Tu**, Alaa Hassan, Javier A. Arrieta-Escobar, et al. Modeling and evaluation of freeform extruded filament based on numerical simulation method for direct ink writing [J]. The International Journal of Advanced Manufacturing Technology, 2022, 120: 3821-3829. DOI: 10.1007/s00170-022-08999-3

[3] **Yongqiang Tu**, Alaa Hassan, Ali Siadat, et al. Numerical simulation and experimental validation of deposited corners of any angle in direct ink writing [J]. The International Journal of Advanced Manufacturing Technology, 2022, 123: 559-570. DOI: 10.1007/s00170-022-10195-2

[4] **Yongqiang Tu**, Alaa Hassan, Ali Siadat, et al. Analytical modeling of deposited filaments for high viscosity material-based piston-driven direct ink writing [J]. The International Journal of Advanced Manufacturing Technology, 2022, 123: 3387-3398. DOI: 10.1007/s00170-022-10511-w

Conference articles:

[1] **Yongqiang Tu**, Javier A. Arrieta-Escobar, Alaa Hassan, et al. Predictive modeling of extruded filament in the air for bioink in direct ink writing using numerical simulation [C]. Procedia CIRP, 2022, 112(4): 394-399. DOI: 10.1016/j.procir.2022.09.026

[2] **Yongqiang Tu**, Alaa Hassan, Ali Siadat, et al. Multi-objective optimization based viscosity prediction for inks in direct ink writing numerical simulations [C]. Intelligent Networked Things, CINT 2022, Communications in Computer and Information Science, 2022, 1714: 147-157. DOI: 10.1007/978-981-19-8915-5_13

[3] **Yongqiang Tu**, Huiyun Gong, Alaa Hassan, et al. Computer vision-based evaluation of dimensional accuracy for MEAM in new product development [C]. Accepted. // The CIRP Design conference, 2023, Sydeny, NSW, Australia.

Yongqiang TU

Process modeling and analysis for direct ink writing based on numerical simulations

Résumé

L'écriture directe à l'encre (DIW) est l'une des techniques de fabrication additive (FA) les plus populaires ces dernières années. DIW appartient à la FA à extrusion de matériaux (MEAM) et elle présente des avantages exceptionnels en termes de compatibilité des matériaux et de flexibilité de l'équipement par rapport aux autres techniques FA. Cependant, la compréhension et l'analyse du processus de DIW n'ont pas été entièrement étudiées, ce qui limite la précision de fabrication et la promotion de l'application de cette technique. La simulation numérique est l'une des outils les plus puissants d'analyse de processus en FA. La recherche sur la modélisation des processus et l'analyse de DIW basée sur des simulations numériques fournira un soutien important pour le développement et l'orientation de DIW. Cependant, il existe actuellement peu de travaux systématiques sur la modélisation et l'analyse des processus basés sur des simulations numériques pour DIW. Pour combler cette lacune, l'objectif de cette thèse est de faire des recherches sur la modélisation et l'analyse des processus pour DIW basée sur des simulations numériques. Cette thèse propose des simulations numériques efficaces basées sur la méthode VOF (Volume OF Fluid) pour la modélisation des sorties dans DIW et vérifie les simulations numériques par vérification expérimentale. L'analyse des processus est effectuée sur la base des simulations numériques proposées, ce qui est utile pour la compréhension et l'analyse des processus de DIW.

Mots clés: Ecriture directe à l'encre, Simulation numérique, Analyse de processus, Volume de fluide, Extrusion de matière

Résumé en anglais

Direct ink writing (DIW) is one of the most popular additive manufacturing (AM) techniques in recent years. DIW belongs to material extrusion AM (MEAM) and it has outstanding advantages in terms of material compatibility and equipment flexibility compared with other AM techniques. However, the process understanding and analysis of DIW have not been fully studied, which limits the manufacturing accuracy and application promotion of this technique. Numerical simulation is one of the most powerful tools in process analysis in AM. The research on process modeling and analysis of DIW based on numerical simulations will provide important support for the development and guidance of DIW. However, there is currently few systematic work on process modeling and analysis based on numerical simulations for DIW. To bridge this gap, the objective of this thesis is to do research on process modeling and analysis for DIW based on numerical simulations. This thesis suggests effective numerical simulations based on Volume Of Fluid (VOF) method for the modeling outputs in DIW and verifies the numerical simulations by experimental verification. Process analysis is conducted based on the proposed numerical simulations, which is helpful for the process understanding and analysis of DIW.

Keywords: Direct ink writing, Numerical simulation, Process analysis, Volume of fluid, Material extrusion